Nature Communications

https://doi.org/10.1038/s41467-026-71524-7

Article in Press

Gmppb-mutant mice exhibit dystroglycanopathy symptoms that are rescued with GSK3β inhibition or AAV-mediated GMPPB gene replacement

Received: 4 August 2024

Accepted: 19 March 2026

Cite this article as: Fu, Z., Wang, T., Zhang, C. *et al. Gmppb*-mutant mice exhibit dystroglycanopathy symptoms that are rescued with GSK3β inhibition or AAV-mediated GMPPB gene replacement. *Nat Commun* (2026). https://doi.org/10.1038/s41467-026-71524-7

Ziwei Fu, Tongchao Wang, Chenyang Zhang, Tianyu Qi, Yanyan Chen, Ju Yang, Hua Yang, Bing Yan, Baoming Gong, Weiqiao Lu, Sushan Luo, Ying Liu, Lei Sun, Hao Jiang, Bo Chen, Zhao Zhang, Xiuping Liu & Yuxiang Wang

Gmppb-mutant Mice Exhibit Dystroglycanopathy Symptoms that are Rescued with GSK3β Inhibition or AAV-mediated GMPPB Gene Replacement

Ziwei Fu[1, #], Tongchao Wang[2, #], Chenyang Zhang[1, 3], Tianyu Qi[1], Yanyan Chen[1], Ju Yang[4], Hua Yang[1], Bing Yan[5], Baoming Gong[5], Weiqiao Lu[6], Sushan Luo[7], Ying Liu[1], Lei Sun[5, 8], Hao Jiang[6], Bo Chen[9], Zhao Zhang[3], Xiuping Liu[4, *] and Yuxiang Wang[10, *]

1. Department of Pathology, School of Basic Medical Sciences, Fudan University, Shanghai 200032, China.
2. State Food and Drug Administration Center for Drug Evaluation, Beijing 100082, China
3. MOE Key Laboratory of Metabolism and Molecular Medicine, Department of Biochemistry and Molecular Biology, School of Basic Medical Sciences, Fudan University, Shanghai, 200032, China.
4. Department of Pathology, School of Basic Medical Sciences, Shanghai Fifth People's Hospital, Fudan University, Shanghai 200240, China.
5. Institute of Developmental Biology & Molecular Medicine, Fudan University, Shanghai, 200433, China
6. Key Laboratory of Marine Drugs of Ministry of Education, Shandong Provincial Key Laboratory of Glycoscience and Glycotechnology, School of Medicine and Pharmacy, Ocean University of China, Qingdao, 266003, China
7. Huashan Rare Disease Center and Department of Neurology, Huashan Hospital, Shanghai Medical College, National Center for Neurological Disorders, Fudan University, Shanghai, 200040, China
8. State Key Laboratory of Genetic Engineering and National Center for International Research of Development and Disease, Institute of Developmental Biology and Molecular Medicine, Collaborative, Shanghai, 200433, China.
9. Keymed Biosciences (Chengdu) Limited, Chengdu 610219, China
10. Department of Pathology, School of Basic Medical Sciences, Fudan University & Shanghai Pudong Hospital, Fudan University Pudong Medical Center, Shanghai, 200032, China.

[#]: these authors contribute equally;

*: Corresponding authors, email: yuxiang_wang@fudan.edu.cn, xpliu1228@fudan.edu.cn

Abstract

Mutations in GDP-mannose pyrophosphorylase B (GMPPB) cause dystroglycanopathy, a rare neuromuscular disorder characterized by α-dystroglycan hypoglycosylation, yet the pathogenic mechanisms and therapeutic options remain poorly defined. To dissect the molecular basis of dystroglycanopathy, we generate *Gmppb* knockout and knock-in (P32L and R287Q) mice. We show that homozygous *Gmppb* knockout and P32L mutant mice (both male and female) display embryonic lethality, while heterozygous *Gmppb*-P32L (*Gmppb*$^{P32L/+}$) mice (both male and female) develop progressive muscular dystrophy accompanied by Purkinje cell loss, peripheral demyelination, and impaired nerve conduction. Integrated biochemical, transcriptomic, metabolomic and glycoproteomic analyses reveal widespread protein hypoglycosylation, metabolic dysregulation and suppressed Wnt/β-catenin signaling, resulting in defective differentiation and regeneration of muscle stem cells. Pharmacological activation of Wnt signaling with CHIR-99021 restores myogenic capacity and improves regeneration after injury. Furthermore, AAV-mediated GMPPB gene replacement reinstates α-dystroglycan glycosylation, normalizes GDP-mannose levels, and rescues motor and electrophysiological defects. Collectively, our findings establish *Gmppb*$^{P32L/+}$ mice as a faithful model of *GMPPB*-associated dystroglycanopathy and demonstrate that Wnt pathway activation and AAV-based gene therapy represent promising strategies for treating glycosylation-defective muscular dystrophies.

Key Words: GMPPB, Rare disease, Muscular dystrophy, Dystroglycanopathy, Gene Therapy, Wnt

Introduction

A group of pathological conditions in the neuromuscular system, including Fukuyama-type congenital muscular dystrophy (FCMD), muscle-eye-brain (MEB) disease, Walker–Warburg syndrome (WWS)[1,2], congenital muscular dystrophy (CMD) 1C/D, and limb-girdle muscular dystrophy (LGMD) 2I/K/M/N[3-5], collectively fall under the classification of Dystroglycanopathy (DGP) based on their uniform feature in abnormal glycosylation of α-dystroglycan (α-DG). Dystroglycan (DG) is a highly glycosylated membrane protein and a key component of the dystrophin-glycoprotein complex (DGC)[6], functioning as a cell-surface receptor for proteins in the extracellular matrix and synapses[7,8]. α-DG is anchored to the cell membrane and stabilizes the structural framework of the cell by binding to the extracellular matrix. In skeletal muscle, this binding function is vital for the protection and stabilization of the muscle fibers[8]. Moreover, the DGC also functions as a platform for signal transduction, recruiting molecules such as nNOS and modulating pathways including nitric oxide, MAPK/ERK, and PI3K/Akt to influence vascular responses, calcium homeostasis, and muscle regeneration[9].

Despite the heterogeneous genetic background of these conditions, which was historically challenging to ascertain due to limited clinically available genomic tools, clinical classification has been primarily based on symptoms, with the specific pathogenesis remaining largely elusive. To date, genomic studies have identified at least 19 genes associated with DGP[10]. The majority of these genes encode enzymes involved in either glycosylating α-DG or providing substrates for post-translational glycosylation modifications of DG[11-13]. Among these genes, *GMPPB*, coding for GDP-mannose pyrophosphorylase B, catalyzes the conversion of GTP and mannose-1-phosphate into GDP-mannose, a key mannose donor for multiple glycosylation pathways, including O-mannosylation, C-mannosylation, N-glycosylation, and glycosyl-phosphatidylinositol (GPI) anchor formation[14,15]. *GMPPB* mutations are inherited in an autosomal-recessive manner. Patients with compound mutations in *GMPPB* display a spectrum of symptoms, ranging from a mild, predominant proximal weakness primarily affecting the lower

limbs, to severe, structural brain defects, intellectual disability, epilepsy, and ocular abnormalities[16]. Creatine kinase levels are typically elevated, ranging from 2 to 50 times higher than normal[17]. Muscle biopsies frequently show myopathic changes with varying degrees of decreased α-DG glycosylation[18,19]. The severe phenotypes significantly affect physiological functions and shorten life expectancy, with many affected patients dying before reaching adulthood[12,18]. The enzymatic activity of GMPPB is negatively regulated by its allosteric feedback inhibitor GMPPA. Mutations in GMPPA result in hyperglycosylation of α-DG and a distinct neuromuscular syndrome[20,21], reflecting the vital role of GDP-mannose homeostasis in the disease context. A recent study shows that E3 ligase TRIM67-mediated GMPPB ubiquitination reduces its activity, with evidence showing that particular patient-derived mutations alter this ubiquitination [22]. Moreover, GMPPB is predicted to undergo methylation and O-GlcNacylation, though specific experimental evidence is lacking[23]. *Gmppb*-deficient cell, zebrafish and mouse models have been generated to establish its contribution to disease pathogenesis[12,24]. However, animal models that faithfully recapitulate the clinical manifestations of *GMPPB*-related DGP remain lacking.

Muscle satellite cells (MuSCs), or muscle stem cells, reside between the basal lamina and the sarcolemma of muscle fibers and are essential for postnatal muscle growth and regeneration [25,26]. Upon activation after injury, MuSCs re-enter the cell cycle and differentiate into myoblasts, which undergo reprogramming of gene expression patterns including Pax7 and Myogenin[27], thereby initiating the differentiation phase and giving rise to myocytes. Defects in MuSC differentiation and self-renewal are increasingly recognized as major contributors to muscular dystrophies[28,29], including Duchenne muscular dystrophy, where defects in polarity, asymmetric division, and myogenic programming limit regeneration[30],[31]. In contrast, the role of MuSCs in DGP remains poorly understood. Although *GMPPB* mutations are linked to hypoglycosylation of α-DG, the mechanisms by which these mutations impair muscle regeneration and contribute to disease progression are not fully defined.

In this study, to investigate molecular pathogenesis and explore therapeutic strategies for *GMPPB*-DGP, we generated genetically engineered mouse strains carrying *Gmppb* mutations and identified neuromuscular phenotypes closely resembling the features of *GMPPB*-related muscular dystrophy, thereby providing direct evidence of *GMPPB* mutations contributing to muscular dystrophy. This characterization involved assessing parameters such as motor performance, histological changes in muscle and brain tissues, serum creatine kinase levels, and the glycosylation status of α-DG. We established *Gmppb*-knockout myoblast cellsand isolated MuSCs from dystrophic mice, to investigate the impact of *Gmppb* mutations on muscle differentiation and regenerative capacity. Transcriptomic, metabolomic and glycoproteomic analyses in these models revealed that *Gmppb* P32L mutation leads to impaired protein glycosylation overall and downregulation of the Wnt signaling pathway, consequently influencing muscle differentiation and regenerative capacity. Pharmacological activation of the Wnt pathway successfully mitigated the phenotypes of *GMPPB*-DGP. Furthermore, we determined the efficacy of AAV gene replacement therapies, which have shown promise in treating diseases such as DMD[32,33]. We showed that AAV-mediated GMPPB expression in the neuromuscular system was sufficient to reverse *Gmppb* mutational phenotypes. This work offers a platform for preclinical investigations on *GMPPB*-DGP and presents promising therapeutic avenues for addressing DGP diseases.

Results

Homozygous *Gmppb* knockout and P32L mutations result in embryonic lethality not rescued by mannose supplementation

First, we integrated published clinical cases of patients with *GMPPB* mutations to catalog the types and frequencies of variants, identifying ten *GMPPB* gene point mutations as the most frequently reported (**Fig. 1a**)[11-13,16,18,34-39]. Notably, patients carrying the P32L and R287Q mutations often present with severe pathological phenotypes, marked by congenital muscular dystrophy along with developmental abnormalities in the brain[16,18,40]. Conversely, those with the D27H mutation typically manifest with milder limb-girdle muscular dystrophy (LGMD) phenotypes. Furthermore, our analysis of the protein structure[41] (**Fig. 1b**) revealed that mutations P32L, D27H, and T153I reside in the Rossman fold region, while mutations V330I, R357H, and R287Q/W are situated in the β-strand region. These regions are critical for the catalytic activity and stability of GMPPB[42]. Therefore, we generated two *Gmppb* knock-in mouse models, namely *Gmppb*^{P32L} and *Gmppb*^{R287Q} mice, as well as one *Gmppb* knockout (*Gmppb*-KO) mouse model (**Fig. 1c**). Specifically, the *Gmppb*^{P32L} and *Gmppb*^{R287Q} mice were generated using a CRISPR/Cas9-mediated homology-directed repair (HDR) approach. For the P32L allele, a single-guide RNA (sgRNA) was designed to target a sequence near nucleotide position c.95 of the *Gmppb* coding region, and a single-stranded oligodeoxynucleotide (ssODN) donor template was provided containing the desired c.95C>T substitution. Similarly, for the R287Q allele, an sgRNA was designed to target the region encompassing nucleotide c.860, and an ssODN donor harboring the c.860G>A substitution was used to introduce the arginine-to-glutamine change at residue 287. For the *Gmppb*-KO line, two sgRNAs were designed to target the intronic regions flanking exons 2 and 3 of *Gmppb*. Simultaneous Cas9-mediated double-strand breaks followed by non-homologous end joining (NHEJ) resulted in the deletion of a 303 bp fragment, leading to a frame shift and functional loss of the gene. In all cases, sgRNAs and donor templates were co-injected with Cas9 mRNA into fertilized C57BL/6J zygotes. Founder mice carrying the intended

mutations were identified by Sanger sequencing of PCR-amplified genomic DNA surrounding the target sites **(Supplementary Fig. 1a, b and c**). Correctly targeted founders were backcrossed to C57BL/6J mice three times to eliminate potential off-target effects and establish stable lines.

The litter size and genotype data indicated that homozygous *Gmppb*$^{R287Q/R287Q}$ mice are viable (**Supplementary Fig. 1a and 2a**), whereas no homozygous *Gmppb*$^{-/-}$ or *Gmppb*$^{P32L/P32L}$ mice are present (**Supplementary Fig. 1b, c and 2d, e)**, suggesting that they may have experienced embryonic lethality. Next, we examined mouse embryos obtained from crossbreeding heterozygous *Gmppb*$^{+/-}$ and *Gmppb*$^{P32L/+}$ mice. The data indicate a significant reduction in embryo counts by E14.5 and evident embryo resorption were observed (**Fig. 1d, 1f**), in contrast to the normal appearance of developing embryos in the *Gmppb*$^{+/+}$ x *Gmppb*$^{+/-}$ **(Supplementary Fig. 1d)** and *Gmppb*$^{+/+}$ x *Gmppb*$^{+/+}$ **(Supplementary Fig. 1e)** crossings. While the development of heterozygous *Gmppb*$^{+/-}$ and *Gmppb*$^{P32L/+}$ was relatively comparable to their respective wild-type littermates at E10.5 and E12.5, with mild to moderate level of edema and local hemorrhage present in a portion of embryos at E12.5 **(Fig. 1e and g)**, both homozygous *Gmppb*$^{-/-}$ and *Gmppb*$^{P32L/P32L}$ embryos exhibited remarkable developmental failure, structural abnormalities and fusion with the maternal tissues **(Fig. 1e and g)**. These results suggest that the homozygous embryos failed to develop before E10.5. Evidently, allele ablation, P32L, and R287Q mutations resulted in varying degrees of functional impairment, with R287Q phenotypes being relatively mild. To determine whether the absence of homozygous offspring resulted from preimplantation defects, we performed genotyping on isolated blastocysts. Consistent with the previous *Gmppb* knockout model[43], homozygous *Gmppb*$^{-/-}$ blastocysts were readily detected (**Supplementary Fig. 2b)**, indicating that complete loss of *Gmppb* permits early embryonic development up to the blastocyst stage. In contrast, *Gmppb*$^{P32L/P32L}$ blastocysts were not observed (**Supplementary Fig. 2c)**, suggesting that embryos carrying the P32L substitution fail to reach or maintain this stage. These findings indicate that while *Gmppb* loss-of-function allows limited pre-implantation development, the P32L mutation causes an earlier or more severe defect. Future studies involving

blastocyst transfer or implantation assays will be valuable to determine whether the P32L embryos can form morphologically normal blastocysts but fail during implantation, or whether defects of the heterozygous carriers contribute to developmental arrest occurs prior to this stage.

Previous studies in Pmm2 mutant mice have shown that mannose supplementation can potentially overcome abnormal glycosylation and embryonic lethality[44,45]. To determine whether mannose supplementation can correct the lethality in *Gmppb* $^{-/-}$ and *Gmppb*$^{P32L/P32L}$ embryos, heterozygous females were provided with drinking water containing 9 mg/mL mannose starting 1 week before mating and throughout mating and gestation[45] to ensure stable embryonic exposure to mannose. The results showed that in *Gmppb*$^{+/-}$ or *Gmppb*$^{P32L/+}$ models, continuous mannose supplementation failed to rescue embryonic lethality (**Supplementary Fig. 2d and e**).

Gmppb-P32L mutation leads to haploinsufficiency of the wild type alleles, resulting in progressive muscular dystrophic phenotypes

That *Gmppb*$^{+/-}$ and *Gmppb*$^{P32L/+}$ models exhibited a more severe phenotype compared to human patients prompted us to investigate the effect of gene dosages in these mouse models. First, to examine histological alterations, we performed Hematoxylin and Eosin (HE) staining on tissues obtained at 32 weeks including the tibialis anterior muscle (TA), gastrocnemius muscle (GA), quadriceps muscle (Qu), heart, diaphragm, and brain tissue. Tissues of *Gmppb*$^{+/-}$ and *Gmppb*$^{R287Q/R287Q}$ mice did not present obvious pathological changes (**Supplementary Fig. 3a**). However, in *Gmppb*$^{P32L/+}$ mice, centrally nucleated muscle fibers were evident in the TA, GA and Qu muscles, indicating ongoing muscle tissue damage (**Supplementary Fig. 3a**). We did not observe significant morphological changes in non-striated muscle tissues such as the heart or diaphragm in these models (**Supplementary Fig. 3a**).

The GA muscles of 32-week *Gmppb*$^{P32L/+}$ mice exhibited reduced GDP-mannose content

assessed by liquid chromatography-mass spectrometry (LC-MS) (**Fig. 2a**), reduced muscle fiber size, as well as an increased level of centrally nucleated myofibers (**Fig. 2b-d**). Furthermore, the proportion of centrally nucleated myofibers increased as *Gmppb*$^{P32L/+}$ mice aged (**Fig. 2e**), indicating a progressive deterioration of this pathological condition. Electron microscopy revealed that 32-week-old *Gmppb*$^{P32L/+}$ mice showed disordered myofilament and dissolving of focal myofilament, which was absent in wild-type muscles (**Supplementary Fig. 3b**). Additionally, myoplasmic necrosis spanning multiple muscle fibers was present in the muscles of 48-week-old *Gmppb*$^{P32L/+}$ mice (**Supplementary Fig. 3c**). Accumulation of scattered autophagic vacuoles containing cytoplasmic debris and electron-dense material was prevalent, and a significant portion of mitochondria appeared distorted in the muscle of *Gmppb*$^{P32L/+}$ mice (**Fig. 2f**). Homeostasis of autophagic activities is critical for muscle development and regeneration, and its dysregulation has been associated with pathological conditions such as myopathies[46,47]. It is important to further investigate whether/how the observed increase in autophagic vacuoles contributes to muscular defects in *Gmppb*$^{P32L/+}$ mice.

Severely affected *GMPPB*-DGP patients routinely display neurological abnormalities[17,48]. In addition, GMPPA deficient mice display a progressive loss of Purkinje cells[20]. We performed a series of analyses to determine whether *Gmppb*$^{P32L/+}$ mice develop additional phenotypes affecting the central and peripheral nerve systems. Glycosylation of α-DG in the whole brain lysate is markedly reduced in the *Gmppb*$^{P32L/+}$ groups, as assessed by Western blots (**Supplementary Fig. 4a**). *Gmppb*$^{P32L/+}$ mice showed no notable differences in structural organization of the brain, with no aberrant neuronal migration in the cerebral cortex and hippocampal region observed (**Supplementary Fig. 4b**). Immunofluorescent staining with NeuN revealed well-organized hippocampal formation, including clearly defined pyramidal and granule cell layers (**Supplementary Fig. 4c**). However, *Gmppb*$^{P32L/+}$ mice showed significantly impairment in spatial learning and memory as assessed by Morris water maze tests (**Supplementary Fig. 4d**). However, though consistent with defective muscle functions,

Gmppb$^{P32L/+}$ mice showed significantly reduced average swimming speed, which confounded the interpretation (**Supplementary Fig. 4d**). Additional motor-independent behavioral assays, such as novel object recognition or fear conditioning, will be important to further confirm the impairment in recognition. Calbindin immunofluorescent staining of the cerebellum indicated a reduced population of Purkinje cells specifically found in 12 month *Gmppb*$^{P32L/+}$ mice (**Fig. 3a**). Together with findings in *Gmppa* mutants[20], this likely reflecting the particular vulnerability of Purkinje cells to disturbances in GDP-mannose homeostasis due to their high metabolic and glycosylation demands. Furthermore, the sciatic nerves of *Gmppb*$^{P32L/+}$ mice displayed marked demyelination, as shown by H&E staining (**Fig. 3b**) and electron microscopy (**Fig. 3c**, red arrows), with spatially disoriented Schwann cells broadly evident (**Fig. 3d**, yellow arrows). In the spinal cord nerves, however, H&E staining and electron microscopy showed no significant changes in neuronal population, myelination or organization (**Supplementary Fig. 4e-g**). Because proper myelination of axons is critical for rapid conduction of electrical impulses, we next assessed the nerve conductance velocity (NCV) and compound muscle action potential (CMAP) with electromyography. The results indicated a significant reduction in conduction velocity and CMAP amplitude in *Gmppb*$^{P32L/+}$ sciatic nerves (**Fig. 3e and f**), indicating impaired transmission. These data show that although gross brain structure appears preserved, Gmppb$^{P32L/+}$ mice develop progressive cerebellar Purkinje cell loss, cognition defect, peripheral nerve demyelination, and impaired nerve conduction, indicating that GMPPB deficiency affects both central and peripheral nervous system integrity.

To evaluate muscle functions and motor activities, we performed rotarod and grip tests on 16-week-old *Gmppb*$^{+/-}$, *Gmppb*$^{P32L/+}$ *Gmppb*$^{R287Q/R287Q}$ and wild-type mice. The average time spent on rotarod significantly decreased in *Gmppb*$^{+/-}$ and *Gmppb*$^{P32L/+}$ mice (**Supplementary Fig. 5a**), while the average grip strength significantly decreased only in *Gmppb*$^{P32L/+}$ mice (**Supplementary Fig. 5b)**. The muscle weakening appeared to be progressive, shown by comparative studies of rotarod and grip test with 16- and 48-week-old mice (**Fig. 3g and h)**.

However, the results of these analyses are dependent on multifactorial determinations, such as muscle mass/body weight ratio, neural conductance. The lean/body weight ratio assessed by EchoMRI displayed significant reduction in *Gmppb*$^{P32L/+}$ mice (**Supplementary Fig. 5c and d**), consistent with the myopathic phenotype. This, together with the impaired nerve conductance and motor coordination (loss of Purkinje cells) we reported above (**Fig. 3a**), necessitating a specific muscle function test in this context. Thus, we performed *in vivo* muscle contraction test on the GA muscle. In this artificially stimulated muscle contraction test, we found that *Gmppb*$^{P32L/+}$ muscle generated a significantly reduced maximal tetanic force compared to WT (**Fig. 3i**). These data demonstrate that *Gmppb*$^{P32L/+}$ mice present a complex phenotype involving both neuropathic and myopathic components.

Patients with *GMPPB*-dystroglycanopathy generally display elevated levels of serum creatine kinase (CK)[11,40]. Similarly, serum CK levels in 30-week-old *Gmppb*$^{P32L/+}$ mice were significantly increased, while those of *Gmppb*$^{+/-}$ and *Gmppb*$^{R287Q/R287Q}$ mice were comparable to those ofwild-type mice (**Fig. 3j**). In contrast, at 16-week serum CK levels did not differ significantly among WT, *Gmppb*$^{P32L/+}$, *Gmppb*$^{+/-}$ and *Gmppb*$^{R287Q/R287Q}$ (**Supplementary Fig. 5a**). Collectively, our results suggest that *Gmppb*$^{P32L/+}$ mice developed progressive defects in muscle development, leading to impaired muscle functions that deteriorate over time.

Gmppb$^{P32L/+}$ and *Gmppb*$^{+/-}$ mice showed a reduced level of α-DG glycosylation

To evaluate the impact of specific mutations on protein abundance, we assessed GMPPB protein levels by immunofluorescence and found no significant differences among the genotypes (**Supplementary Fig. 6a**). Previous research has established a strong correlation between decreased levels of α-dystroglycan (α-DG) glycosylation and dystroglycanopathies, particularly evident in patients with *GMPPB* mutations[12,13,16]. Therefore, we analyzed the level of α-DG glycosylation in our mouse models. First, protein lysates extracted from skeletal muscle lysates and enriched by wheat germ agglutinin (WGA) agarose were assessed for the levels of α-DG

glycosylation using antibodies specifically targeting α-DG glycosylation epitopes VIA4-1 and IIH6C4[49,50] (**Fig. 4a**). The results indicated a significant reduction in α-DG glycosylation in muscles from *Gmppb*$^{P32L/+}$ mice. However, *Gmppb*$^{+/-}$ and *Gmppb*$^{R287Q/R287Q}$ mice exhibited reduced glycosylation levels specifically for VIA4-1(**Fig. 4b and c**). The disparity between VIA4-1 and IIH6C4 may be attributed to their distinct epitope specificities, warranting further investigation. Nevertheless, there were no notable changes in the level of β-DG, nor any observed mobility shifts, as reported in some *GMPPB* patients[35], across all groups (**Fig. 4a and d**). Western blot analyses with two independent total α-DG antibodies showed reduced signal of the mature α-DG banding pattern, consistent with hypoglycosylation (**Fig. 4e and Supplementary Fig. 6b)**. To determine the protein stability, inhibition of protein turnover with cycloheximide (CHX) in *in vitro* cultured muscle slices resulted in varying α-DG degradation rate, with *Gmppb*$^{+/-}$ and *Gmppb*$^{P32L/+}$ muscles showing reduced protein stability compared to WT and *Gmppb*$^{R287Q/R287Q}$ samples (**Supplementary Fig. 6c and d**). In addition, combination treatment of the proteasomal inhibitor MG-132 and CHX indicated that in *Gmppb*$^{P32L/+}$ muscles, degradation pathway is shifted towards the autophagy- or lysosome-dependent routes compared to the relatively preserved α-DG protein in *Gmppb*$^{+/-}$ muscles (**Supplementary Fig. 6c and d**). Additionally, immunofluorescent labeling with IIH6C4 (**Fig. 4f**) and the core α-DG (**Supplementary Fig. 6e**) in cross sections of muscle specimen confirmed the reduced level of α-DG glycosylation and α-DG membrane abundance specifically in *Gmppb*$^{P32L/+}$ muscles. These results suggest the potentially dominant negative role of P32L mutation in the pathogenesis of *GMPPB*-dystroglycanopathy.

The physiological roles of Dystroglycan in maintaining structural stability of muscle relies on their ability to bind to extracellular ligands such as laminin[51]. To investigate whether reduced levels of α-DG glycosylation impact its binding capacity with extracellular ligands, we performed solid-phase laminin-binding assay (**Fig. 4g**) and laminin overlay assay (**Fig. 4h**) using WGA-enriched glycoproteins extracted from the muscles. The overall ligand-binding capacity of native (non-denatured) α-DG was markedly diminished in *Gmppb*$^{P32L/+}$ mice (**Fig. 4g, h**).

Immunofluorescent staining for laminin indicated the membrane binding activity of laminin was significantly reduced in *Gmppb*$^{P32L/+}$ muscles (**Fig. 4i**). Thus, the defective glycosylation of α-DG in *Gmppb*$^{P32L/+}$ mice significantly disrupts the interactions between α-DG and extracellular matrix ligands, such as laminin, in the muscles of these mice.

GMPPB Knockout causes aberrant muscle differentiation

Having established that *GMPPB* P32L mutations lead to impaired α-DG glycosylation resulting in long-term muscle damage resembling muscular dystrophic phenotypes in *GMPPB* patients, we further investigated the molecular consequences on *GMPPB* loss-of-function with C2C12 myoblast cells. First, we generated *GMPPB* knockout C2C12 myoblast cells with CRISPR-Cas9 and confirmed the successful knockout with Western blots and RT-qPCR (**Fig. 5a**). The viability of *GMPPB*-KO cells did not change, and the proliferation activity in *GMPPB*-KO cells were similar to WT C2C12 cells (**Fig. 5b**). We assessed the GDP-mannose abundance using LC-MS showing a significant reduction of GDP-mannose levels in *Gmppb*-KO cells (**Fig. 5c, Supplementary Fig. 7a**). Primary myoblasts can be induced by 2% horse serum to differentiate into multinucleated myotubes and undergo shifts in expression patterns of muscle-specific regulators such as Myogenin and MyHC, a process that is critical in muscle development and regeneration[52,53]. FACS analyses with Annexin V/PI staining showed increased rate of apoptosis in *Gmppb*-KO C2C12 cells during the time course of differentiation (**Fig. 5d**). Additionally, when subjected to differentiation for 7 days with horse serum, immunofluorescent labeling of MyHC indicated abnormal myotube morphology, reduced myotube diameter, and a lower myotube fusion index in *Gmppb*-KO C2C12 cells (**Fig. 5e, f, g**). Together, these data suggest that *GMPPB* loss-of-function disrupts the muscle differentiation and formation of myotubes.

Myogenic regulatory factors (MRFs), such as MyoD, Myf5, Pax7 and Myogenin (MyoG), play vital roles in regulating muscle differentiation, as their temporal expression patterns drive

myogenesis[54]. We next analyzed the level of MRFs in *Gmppb*-KO and wild-type cells during proliferation and differentiation. In the proliferative phase, the expression levels of Pax7 and MyoD were reduced (**Fig. 5h, i, l, m**), whereas the level of Myf5 is increased (**Fig. 5j, n)** in *Gmppb*-KO cells relative to their wild-type counterparts. Meanwhile, consistent with previous studies[55,56], the expression levels of Pax7 and MyoD gradually decrease over time during the differentiation phase in wild-type C2C12 cells (**Fig. 5h, i, l, m**). However, in *Gmppb*-KO cells, this decline of Pax7 and MyoD is absent. Instead, their expression persistently remains at low levels (**Fig. 5 h, i, l, m**). Conversely, during differentiation, the expression of Myogenin gradually increases in *Gmppb*-KO cells but remains significantly lower than in wild-type cells (**Fig. 5k, o)**, whereas Myf5 expression remains elevated compared to wild-type cells (**Fig. 5j, n**). To control for potential effects introduced during KO generation, we assessed Myf5 and Myogenin expression in *Gmppb*-KO cells re-expressing GMPPB (*Gmppb*-KO-CDS; **Supplementary Fig. 7e**); these cells showed expression patterns similar to wild-type C2C12 cells (**Supplementary Fig. 7b, c and d**), indicating that the shift observed in *Gmppb*-KO cells was not due to the knockout procedure itself. Taken together, these findings suggest that *GMPPB* deficiency disrupts the normal temporal pattern of myogenic regulatory factor expression in C2C12 cells during proliferation and differentiation, which may underlie the impaired muscle regeneration and myopathy observed when GMPPB activity is reduced by mutations.

To elucidate the effects of allelic mutations of *GMPPB*, we re-expressed recombinant GMPPB with point mutations (P32L, T153I, R185C, R287Q and V330I) into *Gmppb*-KO C2C12 cells. Western blots with flag antibody confirmed the expression of mutant GMPPB proteins in these stable cell lines (**Supplementary Fig. 7e**). To determine whether *GMPPB* mutations impact the catalytic activity, we determined the GDP-mannose concentrations using LC-MS (**Supplementary Fig. 7f**). We found that both *GMPPB*-P32L and *GMPPB*-R287Q cells displayed a significant reduction in the GDP-mannose content compared to the wild-type cells, indicating again that P32L and R287Q mutations are hypomorphic/amorphic. Notably, the GDP-mannose content in *GMPPB*-P32L cells was approximately 20% of that in wild-type cells

(**Supplementary Fig. 7f**). Moreover, we also determined the subcellular localization of these GMPPB variants with immunofluorescent staining (**Supplementary Fig. 7g**). In wild-type cells, GMPPB displayed a diffuse cytoplasmic localization surrounding the nuclei **(Supplementary Fig. 7g**), consistent with its known role as a cytosolic enzyme involved in GDP-mannose biosynthesis. The P32L and R287Q mutations caused protein aggregation in the cytoplasm. The T153I mutation caused GMPPB to aggregate near membrane protrusions into the cytoplasm. Conversely, the R185C and V330I mutations have no significant changes compared with wild-type GMPPB (**Supplementary Fig. 7g**). Together, these data indicated that *GMPPB* is essential for muscle differentiation and proper subcellular localization.

Gmppb Knockout and *Gmppb*$^{P32L/+}$ lead to widespread disruption of protein glycosylation and impairment of the physiological process related to muscle functions

The varying impact of different mutations on the catalytic activity of *GMPPB* may offer an explanation for the wide spectrum of disease phenotypes observed in patients. However, examination of clinical features of patients with different mutations suggests that phenotypes of compound *GMPPB* mutations may involve a more complicated mechanism that potentially involves compensatory effect[12,18]. Indeed, that *GMPPB*-KO cells are viable, exhibiting no obvious defects in proliferative activity (**Fig. 5b**) further stresses the existence of possible compensation. GDP-mannose is a critical precursor in protein and lipid glycosylation not limited to α-DG[57], emphasizing that deficiency in *GMPPB* may result in global change of the proteome and metabolome, with numerous components involved in gene transcription which promotes the exertion of compensatory mechanisms.

To characterize the mechanisms of *GMPPB*-KO myoblasts on muscle development, we performed RNA sequencing (RNA-seq) analysis on *Gmppb*-KO and wild-type C2C12 cells, and subsequently investigated differentially expressed genes (DEGs) using gene ontology (GO)

enrichment analysis. 1177 differentially expressed genes (DEGs, (490 up/687 down, KO vs. WT)) were identified with the threshold set at p.adjust < 0.05 and |log2FC| > 1 (**Supplementary Fig. 7h and i**). We validated the DEGs expression with RT-qPCR (**Supplementary Fig. 7j and k**). The results revealed a significant enrichment of genes associated with muscle organ development, striated muscle cell differentiation, muscle contraction, and receptor regulator activity (**Fig. 6a**). Similarly, GO analysis of RNA sequencing data from muscle tissue of WT, *Gmppb*$^{+/-}$, *Gmppb*$^{P32L/+}$ and *Gmppb*$^{R287Q/R287Q}$ mice further confirmed the enrichment of pathways related to muscle development specifically in *Gmppb*$^{P32L/+}$ mice. These pathways included response to extracellular stimulus, skeletal muscle organ development, skeletal muscle tissue development, and skeletal muscle cell differentiation (**Fig. 6b**). These pathway alterations again emphasize an association between the *GMPPB* mutation and global transcriptomic changes that result in abnormalities in muscle development, consistent with our observations of muscular dystrophy phenotypes in *Gmppb*$^{P32L/+}$ mice. Furthermore, we observed substantial changes in the abundance of various cytosolic metabolites through LC-MS-based untargeted metabolomics analysis with gastrocnemius muscle of *Gmppb*$^{P32L/+}$ mice **(Supplementary Fig. 8a)**. Pathway enrichment analyses indicated significant alteration in the glycerophospholipid pathway (**Supplementary Fig. 8b**), which plays a vital role in the development of muscular and cellular membrane components[58]. Overall, these results suggest that *GMPPB* loss-of-function (in both *GMPPB*-KO C2C12 cells and *Gmppb*$^{P32L/+}$ mouse model) disrupts the metabolism and transcriptional activities globally. Although our transcriptomic data in mice suggest altered immune pathways, the *Gmppb*-mutant animals did not display obvious immune deficiencies or increased infection under routine conditions. A dedicated immunological evaluation will be required to determine whether these transcriptomic changes translate into functional immune alterations.

To test whether *GMPPB* knockout results in changes in protein glycosylation overall, we detected the glycosylation level of total protein extracted from *GMPPB*-KO cells, using concanavalin A (ConA) that attaches to the mannose and glucose groups on glycosylated

proteins[59], as well as aleuria aurantia lectin (AAL) that recognizes fucose residues in elongated sugar chains[60] (**Supplementary Fig. 9a, b, c**). The results showed a significant reduction in both ConA and AAL signals upon *GMPPB* knockout (**Supplementary Fig. 9d**), suggesting that *GMPPB* loss-of-function disrupted glycosylation of proteins not limited to α-DG. Gene set enrichment analyses (GSEA) of RNAseq data showed that *GMPPB* knockout significantly altered mannose-type O-glycan biosynthesis, with the pathway influencing N-glycan biosynthesis relatively untouched (**Fig. 6c**). These results suggest a potential upregulation of O-mannose biosynthesis in response to *GMPPB* deficiency, although further experimental characterization is required to confirm this compensation mechanism.

Furthermore, GSEA analyses revealed a significant downregulation of pathways associated with the neuromuscular junction (NMJ) in *Gmppb*-KO cells, including neuroactive ligand receptor interaction, acetylcholine-gated channel complex, and postsynaptic neurotransmitter receptor activity **(Fig. 6d).** Quantitative reverse transcription PCR also indicated that the expression of multiple key genes participating in the NMJ signaling transduction, including musk, ryr1 and AchR subunits (chrnd and chrna1) was significantly inhibited in *Gmppb*-KO cells **(Supplementary Fig. 9e)**. Meanwhile, it has been established that regulation of postsynaptic calcium release at the neuromuscular junction is critical for NMJ transmission and generation of contractile force[61]. Also, transcriptomic profiles suggested functional impairments in calcium signaling pathway in *Gmppb*-KO cells **(Fig. 6a)**. Therefore, to determine the consequence of *GMPPB* knockout specifically on muscular calcium signaling, we assessed intracellular Ca^{2+} level with fluorescent Fluo-4 Ca^{2+} indicator. Notably, stimulation with 1 mM ATP resulted in a hyperactive surge in cytosolic calcium influx in *Gmppb*-KO cells **(Supplementary Fig. 9f)**, suggesting dysregulated calcium release from intracellular stores via ectopic activation of a P2Y-evoked and G-protein-mediated signaling pathway. The hyperactive response observed in *Gmppb*-KO cells may indicate an increased susceptibility of dystrophic cells to such stimulation, as has been observed in the *mdx* mouse model of Duchenne muscular dystrophy (DMD), leading to sarcolemma damage[62,63]. These findings highlight the potential disruption of Ca^{2+} homeostasis

following the loss of *GMPPB*, where hyperactive calcium flow disrupted Ca^{2+} dynamics in skeletal myogenesis, hindering muscle development. Taken together, the deficiency of *GMPPB* may lead to deficient protein glycosylation not limited to dystroglycan and disruption of the NMJ signaling pathway, both critical for maintaining normal muscle functions. The dysregulated Ca^{2+} handling observed in our cell and mouse models suggests that NMJ function may also be affected. Detailed NMJ analyses are planned for follow-up collaborations aimed at linking our biochemical findings to synaptic structure.

To further characterize the electron microscopic findings where scattered autophagic vacuoles were identified in *Gmppb*$^{P32L/+}$ muscles (**Fig. 2f** and **Supplementary Fig. 3b and c**), we performed gene set enrichment analysis using transcriptomic data from *Gmppb*$^{P32L/+}$ mutant muscles. This analysis (**Fig. 6e**) revealed significant enrichment of the "unfolded protein response" pathway and a trend toward enrichment of the "reactive oxygen species pathway" ($p = 0.0634$), suggesting activation of proteostatic and oxidative stress programs. Consistent with these findings, Western blot analyses showed a marked increase in the LC3-II/I ratio and accumulation of p62 (**Fig. 6f**) in *Gmppb*$^{P32L/+}$ muscles, whereas these changes were not observed in *Gmppb*$^{+/-}$ or *Gmppb*$^{R287Q/R287Q}$ models. These results indicate that the P32L mutation leads to autophagic flux impairment and mitochondrial stress, revealing a mutation-specific disruption of cellular homeostasis that may contribute to the distinct pathological severity associated with this variant. In addition, to further examine the mitochondrial defects suggested by our ultrastructural analyses (**Fig. 2f**), we performed MitoTracker immunofluorescence staining in C2C12 cells (**Fig. 6g**). In wild-type and *Gmppb*-KO-R287Q cells, mitochondria displayed an interconnected network typical of healthy mitochondrial dynamics. In contrast, *Gmppb*-KO cells exhibited a punctate, fragmented mitochondrial pattern, characterized by discrete dot-like fluorescent signals and loss of the reticular organization, whereas P32L expression (*Gmppb*-KO-P32L) failed to rescue this mitochondria defect (**Fig. 6g**). This altered distribution suggests increased mitochondrial fragmentation and impaired fusion–fission balance. Together, these data indicate that *GMPPB* deficiency, particularly the P32L mutation, induces mitochondrial stress and

structural disorganization, contributing to impaired cellular homeostasis in affected muscle fibers.

Glycoproteomic Analyses indicates widespread protein hypoglycosylation

RNAseq results suggested dysregulation of pathways related to protein glycosylation (**Fig. 6c**). To directly assess this at the protein level, we performed glycoproteomic analysis in which total protein from gastrocnemius muscles of *Gmppb*$^{P32L/+}$ and WT mice was enriched with ConA that specifically immunoprecipitated glycoproteins and their interaction partners, and subjected to LC-MS based identification and quantification. A greater number of peptides were identified in the *Gmppb*$^{P32L/+}$ samples, shown by identified scatter plot **(Fig. 6h**), consistent with Coomassie blue staining of pre- and post-ConA-enriched samples (**Supplementary Fig. 10a**). In total, 692 peptides were identified in WT only, compared to 85 peptides in P32L only (**Supplementary Fig. 10b**). Among the 1288 peptides identified in both groups, 275 showed significantly decreased abundance (FC>1.5; p>0.05), compared to 148 peptides showing increased abundance in *Gmppb*$^{P32L/+}$ muscle (**Supplementary Fig. 10c**). Pathway analyses of differentially expressed peptides indicated positive correlation in pathway related to glycan degradation, and negative correlation in glycosaminoglycan biosynthesis, cytokine-cytokine receptor interaction and the Notch signaling pathway (**Supplementary Fig. 10d**). Together, these data demonstrate that the P32L mutation induces widespread protein hypoglycosylation.

***Gmppb*$^{P32L/+}$mice exhibited reduced capacity for skeletal muscle differentiation and regeneration.**

Next, to determine whether muscle differentiation is also impaired in *Gmppb* mouse models, we isolated GA muscles from *Gmppb*$^{P32L/+}$ mice and wild-type mice, prepared single-cell suspensions, and isolated muscle satellite cells with flow cytometry using surface-specific markers CD31, CD45, Sca1, and VCAM1 **(Fig. 7a)**. The proportion of CD45^{-}CD31^{-}Sca1^{-} VCAM1^{+} MuSCs from *Gmppb*$^{P32L/+}$ muscles showed no significant difference from that of WT muscles (**Supplementary Fig. 11a and b**). However, under differentiation condition they displayed a significant decrease in the capacity to fuse into myotubes **(Fig. 7b)**, with the fusion

index reduced by approximately 30% compared to WT **(Fig. 7d).** Furthermore, the expression of MyoG during differentiation in *Gmppb*$^{P32L/+}$ satellite cells was significantly reduced compared to wild-type satellite cells **(Fig. 7c, e)**. Immunoblotting analyses revealed that, on the first day of differentiation, the expression levels of MyHC and MyoG were comparably low and showed no significant difference between *Gmppb*$^{P32L/+}$ and wild-type satellite cells (**Fig. 7f**). However, by the fifth day of differentiation, induction of MyHC and MyoG expression in *Gmppb*$^{P32L/+}$ satellite cells is significantly dampened compared to that of WT MuSCs (**Fig. 7g, h**).

Upon muscle damage, satellite cells undergo a process of activation, initiated by progressive differentiation to produce muscle cells that fuse into multinucleated myotubes and/or integrate with damaged muscle fibers, facilitating rapid regeneration of mature muscle tissue[64,65]. Since *Gmppb*$^{P32L/+}$ muscle satellite cells exhibit defects in differentiation, next, we further determined whether such defects lead to impairment in muscle regeneration. The cardiotoxin (CTX)-induced muscle injury model has been widely used to investigate capability in skeletal muscle regeneration for its transient and replicable characteristics[66]. We administered CTX to the tibialis anterior (TA) muscles of *Gmppb*$^{P32L/+}$ mice and conducted histological determination at 3, 5 and 14 day post CTX-induced muscle damage (**Fig. 8a**). At 3 days post-injury, wild type TA muscles exhibited a notable presence of newly formed muscle fibers, marked by increased level of centralized nuclei and increased proportion of muscle cells with 2 or more nuclei, as well as increased average cross-sectional area (CSA) of muscle fibers, while *Gmppb*$^{P32L/+}$ mice displayed a limited number of regenerating muscle fibers (**Fig. 8b**). By day 5 post-injury, control mice demonstrated abundant multinucleated myofibers, whereas *Gmppb*$^{P32L/+}$ mice predominantly showed mononucleated fibers, with myofibers being smaller in their CSA (**Fig. 8b**). By day 14 post-injury, control mice presented tightly packed, well-structured muscle fibers, whereas *Gmppb*$^{P32L/+}$ mice displayed regenerating muscle fibers of varying sizes (**Fig. 8b**). Moreover, by five days post-injury, *Gmppb*$^{P32L/+}$ mice exhibited a marked reduction in the proportion of myofibers containing two or more central nuclei (**Fig. 8b, c**). Similarly, the average CSA of

muscle fibers in *Gmppb*$^{P32L/+}$ mice decreased by approximately 40% compared to control mice (**Fig. 8b, d**). Very few of the *Gmppb*$^{P32L/+}$ muscle fibers exceeding 2000 μm^2 in CSA (**Fig. 8e**). The serum CK level in WT mice following CTX treatment spiked at day 3, gradually declined and normalized at day 14 (**Fig. 8f**), while the CK level in *Gmppb*$^{P32L/+}$ mice displayed similar pattern for day 3 and 5, yet failed to normalize (compared to day 0 in *Gmppb*$^{P32L/+}$ mice) at day 14, indicating incomplete regeneration **(Fig. 8f)**. Meanwhile, immunofluorescent labeling of embryonic MyHC showed that immediately following CTX treatment, eMyHC was robustly induced at day 3 and 5 in WT mice (**Fig. 8g, Supplementary Fig. 11c**), and declined to the baseline at day 14 (**Supplementary Fig. 11c**), indicating successful tissue repair despite centralized nuclei still evident in some muscle fibers (**Fig. 8b**). However, eMyHC expression was at a consistently low level at day 3, 5 and 14 in *Gmppb*$^{P32L/+}$ mice, indicating delayed and inefficient myofiber regeneration, consistent with incomplete tissue repair observed in HE staining (**Fig. 8g, Supplementary Fig. 11c**). These findings indicate a crucial role for *Gmppb* in adult skeletal muscle regeneration and suggest that *Gmppb* P32L mutation disrupts skeletal muscle regeneration.

Pharmacological activation of Wnt signaling rescued impairment of myogenesis

The process of myoblasts fusion into myotubes represents a critical step in embryonic and adult skeletal myogenesis necessitating precise temporal and spatial regulation by multiple signaling pathways[67]. To explore the molecular mechanisms underlying *GMPPB's* involvement in muscle development, we analyzed RNA-seq data from *Gmppb*-KO and wild-type C2C12 cells. KEGG enrichment analyses revealed the downregulation of nineteen signaling pathways, in which the Wnt signaling pathway is closely related to myoblast differentiation **(Supplementary Fig. 11f)**. Wnt family proteins are involved in a variety of embryonic and adult processes including proliferation, differentiation and cell fate determination[68]. Specific glycosylation patterns can dictate the spatial and temporal activation of Wnt signaling during myogenesis, whereas aberrant expression of Wnt proteins or their receptors has been associated with muscle-

related disorders and impaired regeneration processes[69,70]. The genes associated with the canonical Wnt pathway exhibited significant downregulation in *Gmppb*-KO cells, accompanied by substantial downregulation of genes linked to muscle development (**Fig. 9a**), consistent with the disruption of expression pattern during induced differentiation (Pax7 and MyoD, **Fig. 5h and i**). Validation through quantitative real-time PCR further confirmed the downregulation of Wnt signaling pathway genes and myogenic genes **(Fig. 9c)**. Furthermore, KEGG enrichment of lectin-enriched proteomic data also support alteration in the Wnt signaling pathway (**Fig. 9b**).

The activation of Wnt signaling cascade involves the engagement of Wnt ligands with their receptor complexes that leads to receptor activation and subsequent inhibition of β-catenin phosphorylation and degradation, thereby inducing translocation of β-catenin into the nucleus where it promotes the transcription of effector genes[68]. In C2C12 cells, we assessed the abundance of nuclear activated β-catenin during the proliferation and differentiation phase. The data indicated a significant decrease in the level of active β-catenin in the nuclear fractions of *Gmppb*-KO C2C12 cells during differentiation, suggesting attenuated Wnt signaling (**Fig. 9d**). Previous studies have demonstrated that reduced nuclear abundance of β-catenin results in reduced differentiation efficiency of muscle progenitor cells (MPCs), while its constitutive presence in the nucleus induces premature differentiation of MPCs, leading to a strong induction of Myogenin expression in primary myoblasts[71]. Multiple studies have also suggested that β-catenin directly interacts with the myogenic factor MyoD during muscle development, thus facilitating subsequent muscle differentiation processes[72,73]. Thus, the impaired Wnt signaling cascade in *Gmppb*-KO cells may underlie defects in muscle differentiation and regeneration.

To test the hypothesis, we administered CHIR-99021, a GSK3β inhibitor that stabilizes β-catenin and thereby activating the Wnt pathway independently of Wnt ligand-receptor interactions, during the differentiation in C2C12 myoblasts, as well as in FACS-isolated muscle satellite cells. The results showed that compared to DMSO-treated cells, CHIR-99021

significantly enhanced myotube formation and fusion indices in Gmppb-KO C2C12 cells (**Fig. 9e**) and *Gmppb*$^{P32L/+}$satellite cells (**Fig. 9f**). Furthermore, treating the mice post CTX-induced muscle injuries with CHIR-99021 led to significant increases in the cross-sectional area of regenerating muscle fibers in *Gmppb*$^{P32L/+}$ mice (**Fig. 9g**). 48-week-old *Gmppb*$^{P32L/+}$ mice treated with CHIR-99021 for 7 consecutive days successfully restored motor ability assessed by rotarod and grip tests (**Supplementary Fig. 11d and e**). Although pharmacological activation of Wnt signaling with CHIR promotes differentiation even in WT cells, the pronounced rescue in *Gmppb*-KO cells indicates that reduced β-catenin activity is a major downstream consequence of *GMPPB* loss. Thus, while the primary defect in *GMPPB* deficiency lies in protein hypoglycosylation, secondary attenuation of Wnt/β-catenin signaling likely contributes to the impaired regenerative response. Enhancing this pathway may therefore represent a rational strategy to ameliorate myogenic defects associated with disrupted glycosylation.

AAV-GMPPB treatment ameliorated the myopathy phenotype of *Gmppb* mutant mice

Most muscular dystrophies are monogenic diseases, and gene therapy mediated by adeno-associated virus (AAV) to replace defective genes holds promise as a potentially curative treatment, as a single injection may achieve therapeutic effects[74]. Early studies have shown that AAV-mediated overexpression of LARGE improved the hypoglycosylation of α-dystroglycan (α-DG) and pathological status of muscles in LARGE^{myd} muscular dystrophy mice. Additionally, LARGE overexpression was able to compensate for the α-DG glycosylation defects caused by mutations in FKTN and POMGnT1[75,76]. Preclinical data suggests that intravascular AAV micro-dystrophin delivery can significantly ameliorate muscle pathology, enhance muscle force, and attenuate dystrophic cardiomyopathy in DMD animal models[33], as well as improving disease symptoms in DMD patients[77]. Therefore, we investigated whether AAV-mediated expression of GMPPB ameliorates the muscular phenotypes in *Gmppb*$^{P32L/+}$ mice. In our studies, GMPPB expression was achieved using the serotype Myo2A adeno-associated virus (Myo2A-AAV),

which has exhibited favorable muscle transduction efficiency compared to the serotype AAV9[78]. Based on the phenotypic characterization of *Gmppb*$^{P32L/+}$ mice in our prior findings where we observed a delayed onset of disease in these mice, we administered systemic delivery of the Myo2A-*Gmppb* virus via tail vein injection into 12-week-old *Gmppb*$^{P32L/+}$ mice to assess the efficacy of AAV therapy **(Supplementary Fig. 12a)**.

After 3 months of AAV injection, Western blots with the GA muscle samples indicated durable GMPPB expression (**Supplementary Fig. 12b**). In these AAV treated *Gmppb*$^{P32L/+}$ muscle samples, a notable reduction in centrally nucleated muscle fibers was evident, with subsequent restoration of muscle morphology (**Fig. 10a, c**). Moreover, IIH6C4-positive α-DG was restored, indicating that AAV therapy elevated the α-DG glycosylation levels of *Gmppb*$^{P32L/+}$ mice muscles (**Fig. 10a, b**). Meanwhile, Western blots showed increased level of IIH6C4 and VIA4-1 in the AAV-treated *Gmppb*$^{P32L/+}$ mice, suggesting that GMPPB overexpression rescues the α-DG glycosylation (**Fig. 10d**). Measurement with LC-MS showed restored GDP-mannose level in *Gmppb*$^{P32L/+}$-AAV muscles (**Supplementary Fig. 12c**), while Western blots indicated restored β-catenin nuclear abundance in *Gmppb*$^{P32L/+}$-CHIR and *Gmppb*$^{P32L/+}$-AAV groups (**Fig. 10e**). Next, we examined the improvement of motor function in mice post-AAV therapy using rotarod test and grip test. Following gene transfer, *Gmppb*$^{P32L/+}$ mice in the AAV treatment group had significantly increased time spent on the rotarod, to a level comparable to those of wild-type mice (**Fig. 10g**). The grip strength of the AAV-treated *Gmppb*$^{P32L/+}$ mice exhibited a significant improvement, suggesting the restoration of muscle physiological function (**Fig. 10h**). Additionally, the serum CK levels in these mice decreased to levels comparable to those seen in wild-type mice (**Fig. 10i**). Meanwhile, we induced muscle injuries with CTX 4 months post AAV administration, to determine the regenerative capacity of muscles. Five days after CTX injection, *Gmppb*$^{P32L/+}$ mice treated with AAV showed a significant increase in the cross-sectional areas of regenerating muscle fibers compared to untreated *Gmppb*$^{P32L/+}$ mice, with no statistically significant difference observed relative to wild-type mice **(Supplementary Fig. 12d)**. The

number of eMyHC+ muscle fibers, demonstrated by eMyHC immunofluorescent labeling, increased by approximately 50% in *Gmppb*$^{P32L/+}$ mice (**Fig. 10j and k**). As shown above, we observed reduced nerve conductance in *Gmppb*$^{P32L/+}$ mice compared to wild-type controls (**Fig. 3e and f**). To evaluate the functional impact of therapeutic interventions, we next measured NCV following AAV-GMPPB or CHIR treatment. AAV-GMPPB–treated *Gmppb*$^{P32L/+}$ mice showed a marked improvement in both conduction velocity and CMAP amplitude, reaching levels comparable to wild-type animals. In contrast, CHIR-treated *Gmppb*$^{P32L/+}$ mice exhibited only marginal changes, with NCV and CMAP remaining significantly lower than that of wild-type or AAV-treated groups (**Fig. 3e and f**). These results indicate that direct restoration of GMPPB expression effectively rescues nerve transmission defects, whereas pharmacological modulation by CHIR provides limited benefit at the functional level. This discrepancy likely reflects the difference in therapeutic mechanisms: AAV delivery reinstates GMPPB expression and thereby corrects the underlying glycosylation defect, whereas CHIR acts indirectly through GSK3 inhibition and may only modulate downstream signaling or metabolic compensation. Because proper glycosylation of α-dystroglycan and other neuronal glycoproteins is essential for efficient neuromuscular transmission, direct restoration of *GMPPB* function appears necessary for functional rescue of nerve conduction.

In conclusion, AAV-mediated GMPPB overexpression significantly enhances the muscle regeneration capacity and nerve conductance of Gmppb$^{P32L+/-}$ mice. These results underscore the effectiveness of AAV-GMPPB gene therapy in alleviating the disease phenotype in *Gmppb*$^{P32L/+}$ mice.

Collectively, our data reveal that *GMPPB* deficiency leads to widespread hypoglycosylation, impaired Wnt/β-catenin signaling, and defective differentiation and regeneration of skeletal muscle stem cells. The P32L mutation results in more pronounced phenotypes than simple haploinsufficiency, manifesting as progressive muscular dystrophy accompanied by neurological involvement, including Purkinje cell loss and peripheral demyelination. These cellular and tissue

defects converge on disrupted glycosylation-dependent signaling and proteostasis stress. Accordingly pharmacological activation of Wnt signaling partially rescued the myogenic defects, while AAV-mediated *Gmppb* expression effectively restored α-dystroglycan glycosylation, improved neuromuscular performance, and normalized muscle regeneration. Together, these findings establish *Gmppb*$^{P32L/+}$ mice as a faithful model of *GMPPB*-associated dystroglycanopathy and provide proof-of-principle that both pathway modulation and gene replacement represent viable therapeutic strategies.

Discussion

Recent studies have established the essential role of *GMPPB* in development of animal models[12,24,40], yetmutational phenotypes have not been systematically characterized in the vertebrates. Here, we generated and analyzed three *Gmppb* mutant mouse models to understand the pathogenesis and establish therapeutic strategies for *GMPPB*-associated dystroglycanopathy. Our data showed that *Gmppb*$^{P32L/+}$ mice exhibit more severe neuromuscular dysfunctions compared to *Gmppb*$^{+/-}$ and *Gmppb*$^{R287Q/R287Q}$ mice. This disparity in phenotypes may be linked to the compensatory role of wild-type allele in *Gmppb*$^{+/-}$ mice, or the retention of enzyme activity in *Gmppb*$^{R287Q/R287Q}$ mice, whereas the potential dominant negative role of *GMPPB*-P32L mutation remains to be further elucidated with detailed biochemical approaches. Although our study focused on the P32L variant, which accounts for roughly 8% of reported *GMPPB* mutations, we recognize that individual *GMPPB* variants may have distinct biochemical and clinical consequences depending on their location within the protein and impact on post-translational regulation such as ubiquitination, stability, or enzymatic activity. Nevertheless, the core mechanisms revealed in our model (GDP-mannose deficiency, widespread hypoglycosylation and impaired Wnt/β-catenin signaling with consequent satellite cell dysfunction) are likely to contribute to disease progression in multiple *GMPPB* mutations. Thus, while the *Gmppb*$^{P32L/+}$ mouse provides a mutation-specific model, it also represents a broadly relevant preclinical platform for dissecting pathogenic pathways and evaluating potential therapeutic strategies for

GMPPB-associated dystroglycanopathy.

Our findings on the lack of efficacy of mannose supplementation in *GMPPB*-mutant mice highlight a critical principle in the dietary management of congenital disorders of glycosylation (CDG): therapeutic outcomes are highly dependent on the specific metabolic block. This pathophysiological context explains the stark contrast between the success of monosaccharide supplementation in certain CDGs, such as glucose for PGM1-CDG where it effectively bypasses an upstream metabolic defect[79] and mannose for PMM2-CDG[45], and its limited or absent benefit in others as we show here for *GMPPB*-related disorder. Previous speculation of the possible therapeutic effects of dietary mannose supplementation in this specific context has been invalidated by our failure to overcome embryonic lethality in our mouse models, despite studies showing that supplementation of GDP-mannose effectively rescued the phenotypes in *gmppb*-null zebrafish model[40], and that mannose deprivation successfully rescued *Gmppa*-null phenotypes in mice[20]. GMPPA loss-of-function leads to increased GMPPB activity and an excess of GDP-mannose, which can result in hyperglycosylation[20,21]. In that context, dietary mannose depletion can reduce the substrate pool and partially normalize GDP-mannose levels. In contrast, *GMPPB* mutations directly reduce GDP-mannose production. In our P32L model, the GDP-mannose pool is already decreased, so additional mannose supplementation does not restore the pathway because the rate-limiting step is the impaired GMPPB enzyme, not substrate availability. This mechanistic difference likely explains why mannose depletion in *Gmppa*-deficient mice was effective whereas mannose supplementation in our *Gmppb* model did not yield benefit. Yet, it was not tested whether supplementation of GDP-mannose has therapeutic potential due to concerns about stability, membrane permeability, and cost in animal models. Also, we did not examine postnatal mannose supplementation in *Gmppb*$^{P32L/+}$ mice in this study, future experiments will be needed to determine whether early or sustained mannose supplementation can modify disease progression in these models. Meanwhile, some of the *GMPPB* mutations found in patients are speculated to disrupt its binding with GMPPA, whereas other mutations

affect catalytic activities of GMPPB[36,80]. *GMPPB* and *GMPPA* mutated patients share common symptoms such as delayed developmental milestones, intellectual disability, and gait abnormalities[21,81], although their putative roles are opposite with GMPPB being the catalytic subunit and GMPPA being its inhibitory binding partner[42]. This indicates that well-balanced physiological GDP-mannose level is important for the cell to process glycosylation. Therapeutic approaches should address homeostasis of mannose processing rather than simply increasing the level of GDP-mannose.

To date, *GMPPB*-related dystroglycanopathy has been considered a recessive disorder. Our study provides a detailed analysis of the *Gmppb*$^{P32L/+}$ mouse model, revealing significant phenotypic consequences not previously identified in human heterozygous carriers. Interestingly, gene dosage or mutational effects of *GMPPB* have been associated with various systemic conditions, including autoimmune disorders, depression, and chronic musculoskeletal pain[82-84]. Although species-specific differences may contribute to variability in phenotypic expression, the *Gmppb*$^{P32L/+}$ mouse nevertheless offers a valuable experimental platform for dissecting disease mechanisms and testing therapeutic approaches. Historically, attention had not been focused on these heterozygous patients, potentially due to the subclinical nature of their manifestations. Our findings suggest that P32L mutations, previously considered to have a milder effect, can indeed lead to more pronounced symptoms and contribute to the understanding of how these mutations affect muscle regeneration. Further studies involving a more detailed characterization of the P32L mutation are expected to reveal additional insights into its role and the overall disease mechanism.

Across dystroglycanopathy models, the severity of muscle pathology does not always scale linearly with the apparent reduction of functional α-dystroglycan glycosylation as assessed by commonly used biochemical readouts. Differences in developmental timing, tissue context, genetic background, and compensatory remodeling can modulate how a given glycosylation defect translates into overt dystrophy. For example, several recessive DGpathy models such as the *Large*^{myd} mouse[85] and early myogenic lineage *Fukutin* conditional knockout mice develop

robust dystrophic changes[86], whereas other genetic models including *POMGnT1*-null mice[87] and *Fukutin* transposon knock-in mice[88] have been reported to exhibit minimal overt dystrophic pathology despite pronounced biochemical defects in α-DG glycosylation. Collectively, these observations suggest that additional molecular and/or cellular abnormalities beyond α-DG hypoglycosylation can modulate disease severity and contribute to dystrophic outcomes. This broader framework supports the view that *GMPPB*-associated disease mechanisms may extend beyond impaired α-dystroglycan ligand binding. Consistent with this, our multi-omic and functional analyses point to reduced sugar-nucleotide availability and widespread hypoglycosylation of cellular proteins, together with cellular stress signatures, which likely cooperate to impair myogenesis and regeneration in *Gmppb*$^{P32L/+}$ muscle.

Our studies established a primary association between *GMPPB* loss and impairment in the differentiation and regeneration of muscle stem cells. We observed that the deletion of the *Gmppb* gene affected the expression of myogenic regulatory factors, leading to a decrease in myotube diameter and a reduction in myotube fusion index in C2C12 myoblasts. Additionally, satellite cells derived from *Gmppb*$^{P32L/+}$ mice also showed decreased expression of Myogenin and exhibit defects in myotube formation. In response to muscle damage, satellite cells play a crucial role in reconstituting fiber integrity and function. By using a CTX-induced muscle injury model, our data further revealed impaired regeneration capability in *Gmppb*$^{P32L+/-}$ mice, as evidenced by a reduction in the cross-sectional area of regenerating muscle fibers and a decrease in the number of eMyHC+ muscle fibers. Previous studies have indicated that similar phenotype exists in other mouse models of muscular dystrophy as well. For instance, *Myf5-fukutin*-cKO mice display reduced differentiation and regeneration capacity in muscle stem cells[89]. Likewise, mice lacking dystroglycan (MORE-DG)[90] and mdx mice[91] at approximately 1 year of age exhibit impaired muscle regeneration capability. In the muscle fibers, active dystroglycan expression is vital for efficient regeneration of skeletal muscles[90]. These experimental observations collectively suggest that defects in MuSC differentiation and regeneration are critical in mediating the pathogenesis and progression of *GMPPB*-associated dystroglycanopathy.

Our transcriptomic, proteomic, and functional data collectively suggest that the P32L mutation leads to widespread hypoglycosylation of cellular proteins. Hypoglycosylation can disrupt the folding, stability, and trafficking of glycoproteins, causing ER retention and activation of the unfolded protein response (UPR). Chronic ER stress in turn promotes autophagy as a compensatory mechanism to clear misfolded proteins and damaged organelles[92]. Consistent with this model, *Gmppb*$^{P32L/+}$ muscles displayed enrichment of UPR, accumulation of p62, elevated LC3-II, and mitochondrial fragmentation. In parallel, we observed reduced nuclear β-catenin in *Gmppb*$^{P32L/+}$ cells, implicating impaired Wnt/β-catenin signaling. Notably, Wnt and autophagy pathways are known to reciprocally regulate each other, with canonical Wnt activation suppresses autophagy, whereas autophagy can modulate Wnt signaling by degrading pathway mediators[93], suggesting that the combined Wnt attenuation and autophagic activation we observe may represent a mutually reinforcing loop. Given that Wnt signaling regulates satellite cell self-renewal and differentiation, its attenuation together with autophagy/mitochondrial defects may synergistically impair muscle regeneration. These findings highlight a potential feed-forward mechanism wherein global hypoglycosylation dampens Wnt/β-catenin signaling and activates autophagy, which together contribute to the neuromuscular pathology of *GMPPB*-associated dystroglycanopathy. Interestingly, in the flatfishes (such as *Trinectes maculatus*), highly frequent genetic changes in the dystrophin–glycoprotein complex during evolution are speculated to facilitate the asymmetric body plan. These genetic changes are coupled with alterations in the Wnt signaling pathway[94]. In line with this evolutionary association, our findings suggest a previously unrecognized connection between GMPPB function and Wnt signaling. As GMPPB supplies GDP-mannose for multiple glycosylation pathways, its deficiency is expected to broadly impair protein glycosylation, potentially influencing the folding, trafficking, and surface expression of Wnt ligands, receptors, and co-receptors that depend on proper glycan modification for stability and signaling competence. Consistent with this notion, RNA-seq analysis of *GMPPB*-KO cells revealed marked alterations in the expression of Wnt pathway genes, while

lectin-enriched glycoproteomics combined with GSEA identified a shift toward increased "glycan degradation" and reduced "glycosaminoglycan biosynthesis," "cytokine-cytokine receptor interaction," and "Notch signaling." Together, these results indicate that *GMPPB* deficiency perturbs glycosylation networks critical for maintaining Wnt pathway integrity, leading to secondary transcriptional and signaling changes. Although our current data establish a clear association rather than a direct mechanistic link, they raise the possibility that disrupted glycosylation of specific Wnt components or regulators contributes to the altered signaling landscape. Further studies dissecting which glycoproteins mediate this connection will be essential to define how metabolic defects in GDP-mannose synthesis translate into pathway-specific signaling dysfunction.

Currently, there are no effective therapeutic options for dystroglycanopathies, which are primarily managed with supportive glucocorticoid therapy[38,95]. Over the past decade, adeno-associated viral (AAV) gene therapy has made significant progress in treating Duchenne muscular dystrophy, ameliorating symptoms and offering a promising direction for muscular dystrophy gene therapy[33,77,96]. Studies have shown that in *Myf5-Fukutin*-cKO mice with abnormal muscle regeneration, AAV vectors enabled selective expression of the *Fukutin* gene in muscle fibers, leading to significant improvement in muscular dystrophy symptoms[89]. Similarly, this gene therapy approach has shown effectiveness in mice with FKRP mutations and Large^{myd} mice[76,97,98]. Tokuoka et al. also demonstrated the rescue of muscle pathology in an ISPD-deficient mouse model through AAV-mediated ISPD gene therapy[99]. Previous study confirmed that MyoAAV transduction is more efficient in muscle compared with AAV9[78,100]. In this study, Myo2A-AAV-Gmppb was administered intravenously to 12-week-old *Gmppb*$^{P32L/+}$ mice. Three months post-injection, we observed improvements in muscle pathology and restoration of α-DG glycosylation levels in *Gmppb*$^{P32L/+}$ mice. Following AAV treatment, the motor function, muscle strength, and creatine kinase levels in *Gmppb*$^{P32L/+}$ mice were comparable to those of wild-type mice. Additionally, four months after AAV administration, the muscle regeneration capacity of

Gmppb$^{P32L/+}$ mice was significantly enhanced. Thus, our findings confirm the effectiveness of AAV therapy for *GMPPB* mutant muscular dystrophy. However, although the safety profile has been primarily established in previous studies[78], the side effects of delivering *Gmppb* in this specific context are yet to be characterized. *In utero* gene replacement holds promise as an approach for addressing genetic defects that lead to embryonic lethality[101]. However, this strategy currently encounters substantial technical and ethical challenges, particularly in cases of lethality during early pregnancy[102]. Methodological advancements are essential to assess the efficacy of rescuing lethality induced by *GMPPB* mutations using this approach.

Despite the well-established role of *GMPPB* in the glycosylation pathway and the consequent hypoglycosylation of α-DG, the precise molecular mechanism linking this enzymatic defect to muscle fiber degeneration remains unresolved. Our data suggest that *GMPPB* deficiency provokes broader cellular stress beyond impaired α-DG–mediated adhesion, as evidenced by the accumulation of autophagic vacuoles, exaggerated Ca^{2+} release, and disrupted mitochondrial morphology. These findings raise the possibility that defective glycosylation of additional client proteins, particularly those involved in ER homeostasis or Ca^{2+} handling, may drive a cascade of ER stress, mitochondrial dysfunction, and impaired autophagic flux that secondarily destabilizes the sarcolemma. Alternatively, α-DG hypoglycosylation itself could initiate mechanical or signaling stress leading to these downstream perturbations. Discriminating between these "adhesion-first" and "proteostasis-first" models represents a central unresolved question in the molecular pathology of *GMPPB*-related dystroglycanopathy. Future work defining the spectrum of mis-glycosylated substrates (with PNGase F/Endo H) and establishing the temporal order of these cellular events will be essential to identify the primary driver of disease and therapeutic strategies capable of restoring both glycoprotein integrity and cellular homeostasis.

In summary, our findings establish a coherent model linking defective GDP-mannose metabolism to multisystem pathology through the combined effects of disrupted glycosylation, impaired signal transduction, and cellular stress. *GMPPB* deficiency compromises glycosylation

of α-DG and other critical substrates, destabilizing the sarcolemma–ECM interface and perturbing receptor pathways such as Wnt that depend on precise glycan modification. The resulting imbalance between proteostasis, mitochondrial integrity, and myogenic signaling creates a feed-forward cascade leading to progressive muscle and neuronal degeneration. Importantly, the phenotypic rescue achieved by pharmacological Wnt activation and AAV-mediated GMPPB restoration demonstrates that both pathway modulation and gene replacement can effectively re-establish homeostasis in affected tissues. These results not only clarify the molecular basis of *GMPPB*-associated dystroglycanopathy but also outline a general therapeutic paradigm for metabolic glycosylation disorders in which targeted correction of signaling and enzymatic defects act synergistically to restore tissue integrity.

Methods

Ethical statement

All animal experiments were carried out in accordance with ethical regulations regarding animal research and were approved by the Experimental Animal Ethics Committee of the School of Basic Medicine of FudanUniversity under license number IACUC20211018-001.

Generation and genotyping of *Gmppb* mutant mice. The *Gmppb* knock-out (*Gmppb*-KO) and knock-in mice (*Gmppb*^{P32L} and *Gmppb*^{R287Q} mice) were generated by the CRISPR-cas9 system, in collaboration with the National Resource Center for Mutant Mice, Nanjing University. *Gmppb* knock-out mice were generated in C57/BL6 mice and deleted 303 bp genomic sequence. The *Gmppb*^{P32L} and *Gmppb*^{R287Q} mutations were introduced into the mouse *gmppb* orthologue to generate *Gmppb*^{P32L} mice and *Gmppb*^{R287Q} mice using the CRISPR system and donor template in C57/BL6 mice. The following genotyping primers were designed for testing *Gmppb*-KO mice: P1: 5'-AACATCTGCAGACGCCAT-TGA-3'; P2: 5'-AGGGTGGGAATGTCAGAGGA-3'; P3: 5'-GGGAGGGTATGGGACACACGG-3'; P4：5'-AGGGACCTAAAGAAAG-AAAGGGCTAAGT-3', *Gmppb* knock-out mice genotyping can be tested by analyzing PCR products. The PCR results from the *Gmppb*^{P32L} and *Gmppb*^{R287Q} mice should be sequenced using the primers listed below: P32L-F: 5'-GGGCGTTGAAATCTAATTGG-3'；P32L-R: 5'-CATGTAGCTCACTGCCAGGATCA-3'; R287Q-F: 5'-TGCCTCTTCCTACAATCGCTGA-3'; R287Q-R: 5'-CTATGACATCTTCACCCAGCACTG-3'. Mice embryos from intercrosses of heterozygotes were also genotyped using the above primer. For embryo genotyping, pregnant females were euthanized at the indicated gestational stage, and embryos were dissected from the uterus under a stereomicroscope. Extraembryonic membranes (yolk sac and placenta) were carefully removed to avoid maternal tissue contamination. Embryos were briefly rinsed in sterile phosphate-buffered saline (PBS) and placed in fresh tubes for DNA extraction. Genomic DNA was isolated from embryonic tissue (head or trunk) using standard lysis buffer and proteinase K digestion, followed by PCR-based genotyping using allele-specific primers. All procedures

followed established protocols for embryo handling and genotyping[103]. In the case of partially resorbed embryos, only clearly identifiable embryonic tissue was dissected free from maternal decidual tissue under a stereomicroscope. Samples were extensively rinsed in fresh PBS prior to DNA extraction. Resorption sites without discernible embryonic structures were not used for genotyping to avoid maternal contamination.

Sex was not considered in the study design as no previous report indicated obvious association of sex and *GMPPB* phenotypes. Therefore, the analyses did not involve sex-specific considerations.

Cell lines and *Gmppb* mutant C2C12 cells. C2C12 cell lines were purchased from the American Type Culture Collection (ATCC). Cell lines were authenticated by short tandem repeat analyses, and routinely monitored for mycoplasma contamination every month. To knock out *Gmppb* in C2C12 cells, we transfected C2C12 cells with CRISPR plasmids PX458-GFP and PX459-puromycine with two sgRNA. Two pairs of sgRNAs were designed to target exons 1 and 5 of *Gmppb* gene: exon 1 (F: 5'-CACCGAGCACTCCGAAGCCATTGG-3'; R: 5'-AAACCCAA-TGGCTTCGGAGTGCTC-3'); exon5 (F: 5'- CACCGAGAGCCTTCCAAGTATG-GTG-3'; R: 5'- AAACCACCATACTTGGAAGGCTCTC-3'). We tested transfection efficiency through PX458 plasmids with GFP. At 48 h after transfection, the cells were diluted and cultured with puromycine (4 μg/ml) for a two-day resistance screening. The clones were then diluted to a 96-well plate to expand the culture. Finally, expanded monoclonal cells were confirmed by PCR sequencing. The efficacy of guide RNA was determined by western blotting. In addition, we constructed *GMPPB* mutant plasmids in *Gmppb*-KO cells. To acquire the *Gmppb* open reading frame, we amplified *Gmppb* CDS (coding DNA sequence) using C2C12 cDNA as a template and cloned *Gmppb* CDS into pCDH-3xflag-GFP-puro (Addgene, #167463). Then, the allelic mutations c.95C>T, c.485C>T, c.553C>T, c.860G>A and c.988G>A were introduced into the wild-type plasmid using the NEBuilder HiFi DNA assembly master mix (New England Biolabs, MA, cat. # E2621S). All plasmids were verified by Sanger sequencing, and overexpressed GMPPB mutant proteins were also verified by Western blots.

Western blot analysis. For total protein extraction, C2C12 and satellite cells were lysed in RIPA buffer (Beyotime Biotechnology) and then centrifuged at 12000 rpm for 15 minutes at 4 ℃. The supernatant was collected in a new tube. Skeletal muscle tissue protein extraction using Minute™ Total Protein Extraction Kit (Invent Biotechnologies). Nuclear protein extraction using Nuclear and Cytoplasmic Protein Extraction Kit (KeyGEN BioTECH). For glycoprotein extraction. 100mg skeletal muscles were added to 1ml cold Tris-buffered saline [TBS,50 mM Tris-Hcl(PH 7.4),100 mM NaCl] plus 1% Triton-X100 and protease inhibitors, and then homogenized for 1 hour. Glycoproteins were captured with 200ul wheat-germ agglutinin (WGA) agarose (Vector Laboratories) beads overnight. The next day, the homogenate was washed three times with TBS buffer containing 0.1 % 1% Triton-X100 and protease inhibitors and then eluted with SDS-loading buffer. Next, 30μg of the total protein was separated by SDS-PAGE and electrotransferred onto a polyvinylidene fluoride (PVDF) (Millipore) membrane. Membranes were blocked in 5% skim milk powder for 1 hour at room temperature, then incubated with primary antibodies at 4 ℃ overnight. The next day, The PVDF membrane was washed with TBST three times for 5 minutes and stained with the HRP-conjugated secondary antibodies for 1 hour at room temperature. Membranes were washed with TBST three times for 5 minutes and imaged using the Tanon 5200 Series Chemiluminescence Image Analysis System. Band intensities were analyzed with ImageJ software. The primary antibodies used were as follows: mouse anti-GMPPB (Proteintech, 15094-1-AP) 1:500, mouse anti-α-DG IIH6C4 (MilliporeSigma, 05-593) 1:250, mouse anti-α-DG VIA4 (MilliporeSigma, 05-298) 1:250, mouse anti-RL2 antibody (Abcam, ab2739), sheep anti-core DG (R&D Systems, cat# HAF016) 1:1,000, mouse anti-MyHC (DSHB, MF20) 1:500, mouse anti-β-DG (DSHB, 7D11) 1:500, mouse anti-PAX7 (DSHB, 1-9) 1:500, mouse anti-MyoG antibody (DSHB, F5D) 1:500, mouse anti-vinculin (MilliporeSigma, V4505) 1:5000, mouse anti-MyoD1(Dako, M3512) 1:500, mouse anti-myogenin (Santa Cruz,sc-12732) 1:500, mouse anti-GAPDH(Santa Cruz, sc32233)1:1000, rabbit anti-Myf5 (Abcam, ab125301) 1:500, rabbit anti-Histone H3 (Abcam, ab1791) 1:1000,

rabbit anti-β-tubulin (Abcam, ab6046) 1:500, rabbit Non-phospho (Active) β-catenin (Abclonal, A22180) 1:2000, rabbit Lamin B1 antibody (Abclonal, A11495) 1:1000. All images of uncropped blots are available in the Supplementary Information file.

Laminin overlay assay. Laminin overlay assay was performed as previously reported[104]. Briefly, protein bands were transferred onto the PVDF membrane. The PVDF membranes were blocked in laminin binding buffer (LBB: 10 mM triethanolamine, 140 mM NaCl, 1 mM MgCl2, 1 mM CaCl2, pH 7.6) containing 5% nonfat dry milk, further incubated 10nM mouse EHS laminin (L2020, Sigma) overnight at 4℃ in LBB. Membranes were washed and incubated with anti-laminin (ab11575; Abcam) followed by anti-rabbit IgG-HRP. Blots were exposed by chemiluminescence.

Solid-phase laminin binding assay. Solid-phase assay was also performed as previously reported[104]. Wheat germ agglutinin (WGA)-purified skeletal muscle samples were diluted 1:100 in TBS buffer and coated onto 96-well polystyrene ELISA microplates (Costar) overnight at 4℃. After washing in LBB four times the next day, plates were coated with 3%BSA in LBB for 2 hours. Wells were rinsed with 3%BSA in LBB and added with dilutions of 2 nM-30 nM mouse EHS laminin (L2020, Sigma) for 2 hours at room temperature. After washing four times with 3%BSA in LBB, Wells were incubated for 1 hour with anti-laminin (1:5000; ab11575; Abcam) followed by anti-rabbit HRP. Plates were developed with o-phenylenediamine dihydrochloride and H_2O_2, reactions were stopped with 2M H_2SO_4, and values were obtained on a microplate reader at 495nm.

Isolation and culture of muscle satellite cells. Muscle satellite cells (MuSCs) isolation was performed as previously described[105]. Briefly, hind-limb skeletal muscles were dissected, digested by collagenase type II, and dissociated using a gentleMACS Dissociator (Miltenyi Biotec). Digested muscle suspensions were subsequently filtered through a 70-μm cell strainer and 40-μm cell strainer and then washed to yield a mononuclear cell suspension. The cells were

stained with CD45-BV650(1:75; Clone I3/2.3; BD Bioscience); CD31-BV650 (1:75; clone 390(RUO); BD Biosciences); Sca-1-FITC (1:75; 553335; BD Biosciences; VCAM1-biotin (1:75; 553331; BD Biosciences) and Streptavidin-APC (1:300; 405207; BioLegend). Streptavidin-APC (1:300; 405207; BioLegend) was used to amplify the VCAM1 signal. Cells were sorted using a FACSAria II cell sorter (BD Biosciences) equipped with 488-nm, 633-nm, and 405-nm lasers. Isolated MuSC were either directly used for protein extraction or cultured for proliferation and differentiation assays. MuSC were cultured in 6 cm plates with growth medium (30% fetal bovine serum (FBS), 1% chick embryo extract,10 ng/ml basic fibroblast growth factor (bFGF), and 1% PS in DMEM). To induce MuSC differentiation, cells were incubated with DMEM supplemented with 2% horse serum.

Histology and Immunofluorescence. Mouse skeletal muscles were collected and embedded in OCT embedding matrix and frozen in liquid N_2-cooled isopentane. 6 μm thick cryosections were then prepared at -80 ℃ to maintain muscle morphology. To visualize muscle morphology, Hematoxylin and eosin(H&E) staining was performed in muscle sections. For muscle fiber diameter quantification, the borders of fibers were manually outlined in given Area of Interest (AOI) and fibers cut at the edges were excluded. The Hue, Saturation, Intensity (HSI) was adjusted to effectively separate the stained muscle fibers from the interstitial space. The total cross-section AOI was calculated and average fiber radius generated by $r = \sqrt{[Area/\pi}$. All images used for quantification for the gastrocnemius were taken from the mid-belly region at a comparable anatomical level in each animal, and the same selection criteria and magnification were applied across genotypes. The analyses were double blinded to minimize bias. For the Immunofluorescence assay, sections were fixed with 4%PFA for 15 minutes at RT and subsequently permeabilized using 0.5% Triton X-100 in PBS. The sections were blocked for 1 hour at RT in PBS containing 3%BSA. After blocking, sections were stained overnight at 4℃ with primary antibodies. Subsequently, the samples were washed with PBS and stained with the **appropriate** secondary antibodies (Alexa Fluor 647, Alexa Fluor 488) for 1h at RT with

avoiding the light. After washing with PBS, 1 μg/ml DAPI was used to stain nuclei for 5 min. The primary antibodies used were as follows: anti-GMPPB (Proteintech, 15094-1-AP) 1:200, mouse anti-MyHC (DSHB, MF20)1:300, mouse anti-eMyHC (DSHB, F1.652) 1:50, mouse anti-MyoG antibody (DSHB, F5D) 1:200, rabbit anti-Laminin (Abcam, ab11575)1:500. Analysis of myotube diameter and fusion index was performed on images after MyHC immunofluorescence staining. At least 10 non-overlapping high-power fields were randomly selected for analysis. The measurement of myotube diameter was defined as follows: for each selected myotube, the width at the narrowest point was measured perpendicular to its long axis, and each myotube was measured three times to take the average value. Only muscle-like structures containing 3 or more nuclei were identified as myotubes. The calculation formula for the fusion index is: Fusion Index = (Total number of nuclei fused into myotubes / Total number of nuclei in the field of view) × 100%.

Transmission Electron Microscopy. We examined the ultrastructural alterations in the gastrocnemius muscles of both 32-week-old and 48-week-old *Gmppb*$^{P32L/+}$ mice and WT mice. The muscle tissues were sliced into 1mm × 1mm × 3mm sections with a sharp blade and subsequently immersed in 2.5% glutaraldehyde fixative solution, where they were fixed at 4°C for 24 hours. Then, the samples were dehydrated in a series of ethanol and embedded in resin. The ultra-thin sections were stained with uranyl acetate and lead citrate. The sections were imaged using a PHILIPS transmission electron microscope (PHILIPS, CM120, Netherlands). The sciatic and spinal cord nerves were isolated from 32-week mice and underwent similar processing for EM determination of the cross sections.

Quantitative PCR with reverse transcription. Total RNA was isolated by trizol-chloroform extraction. 3μg of RNA was reverse-transcribed using the SuperScript III Transcriptase kit (Invitrogen, #18080093), and qPCR was performed using Taq Pro Universal SYBR qPCR

Master Mix (Vazyme, #Q712). The primers used were as follows: Gapdh (5′-GTCAAGGCCGAGAATGGGAA-3′, and 5′-CTCGTGGTTCAC ACCCATCA-3′), Wnt7b (5′- CAATGGTGGTCTGGTACCCAA-3′, and 5′-AGTCT-CATGGTCCCTTTGTGGTT-3′), Wnt6 (5′-CTTGGTCATGGATCCTACCAGCAT-CT-3′, and 5′- TCGTTGTTGTGCAGTTGCACCAATGC-3′), Lef1 (5′-ACAGCGA-CCCGTACATGTCAAA-3′), FZD4 (5′-GACAACTTTCACGCCGCTCATC-3′, and 5′-CAGGCAAACCCAAATTCTCTCAG-3′), MyoD1 (5′-AGCACTACAGTGGCG-ACTCA-3′, and 5′-GGCCGCTGTAATCCATCA-3′), Pax7 (5′-GGCACAGAGGAC-CAAGCTC-3′, and 5′-GCACGCCGGTTACTGAAC-3′), Musk (5′-AGCCGATGTG-TCTGCTCTTT-3′, and 5′-ACAGGACAGTGGTGGAGGAC-3′), Chrnd (5′-CTAAG-TCTCACCCTCTCCAACCTCATCTC-3′, and 5′-GCACATTGCAGGCATAAGAA-ATCTGGAAC-3′), Ryr1 (5′-TTTCCTGGACCGAGTGTATGGC-3′, and 5′-CAGAC-AGAGGTAGCGGTTCAGT-3′), Chrna1 (5′- TCATCATTCCCTGCCTGCTCTTCT-3′, and 5′-TCTCTGCAATGTACTTCACGCCCT-3′). Experiments were performed in biological replicates as indicated in figure legends. Gapdh RNA was used to normalize data from RT-qPCR mouse samples.

Muscle injury. Muscle regeneration was induced by the injection of cardiotoxin (CTX) into TA muscle. Briefly, a total of 100 μl of 20 μM CTX was injected into TA muscle with three injections. The 28-gauge needles were inserted parallel to the muscle fiber and injected into each end of the TA muscle and the middle of the TA muscle separately. CTX-injured muscles were dissected on 3 days, 5 days, and 14 days following injury. Every experiment included at least three animals to assess muscle regeneration and repair.

GDP-mannose measurement. GDP-mannose measurement was performed as previously reported[42]. C2C12 cells (1×10^7) with different *GMPPB* mutations were collected and washed three times with PBS. After that, cells were put into a 15-ml tube and chilled with liquid nitrogen

for 20 seconds. The cell mixture was given a pre-chill of -80 °C and methanol (2 ml, 80% (vol/vol)). The tube was then kept at 80 °C overnight for incubation. The supernatant was collected after centrifugation at 12,000g for 20 minutes at 4°C. A speed vacuum dried the samples at RT for two hours. GDP-mannose was analyzed using a TSQ Quantiva mass spectrometer (Thermo Fisher) coupled with reverse-phase chromatography48. Mobile phases A and B contained water with 10mM tributylamine and 15mM acetate and 100% methanol, respectively. GDP-mannose (purity ≥99.9%) were used as standard samples. Ion transitions of 604/362nm and 588/442nm were used for GDP-mannose. The resolution for Q1 and Q3 was set at 0.7 full-width at half-maximum (FWHM). The source parameters were as follows: spray voltage, 2,500V; ion transfer tube temperature, 320°C; vaporizer temperature, 300°C; sheath gas flow rate, 30 (arbitrary units); auxiliary gas flow rate, 10 (arbitrary units).

***Ex Vivo* muscle culture and CHX/MG-132 treatment.** GA muscles were rapidly dissected into ice-cold DMEM, fascia and tendinous ends were trimmed to improve reagent penetration and mounted in a chilled slicing chamber and cut into 200–300 μm transverse slices. Only slices with uniform thickness and intact architecture were used. Slices were equilibrated for 15 min at 37 °C in DMEM supplemented with 10% FBS and 1% penicillin/streptomycin, with gentle orbital agitation (50–70 rpm). CHX (50 μg/mL) or MG132 (10 μM) was added to block biosynthesis or prevent proteasomal turnover. Medium was refreshed every 60–90 min to maintain oxygenation and remove debris. Slices were harvested at 6 h and protein lysates were isolated by grinding with liquid nitrogen. Protein lysates were subjected to Western blots using α-DG core antibody (Millipore, 3D7).

Morris water maze test. The Morris water maze apparatus consisted of a circular pool (120 cm diameter, 50 cm height) filled with opaque water maintained at 22 °C. A transparent escape platform (10 cm diameter) was submerged 1 cm below the surface in a fixed location. Mice were subjected to four trials per day for six consecutive training days, with a maximum trial duration of 60 s and an intertrial interval of approximately 15 min. If a mouse failed to locate the platform within 60 s, it was gently guided to the platform and allowed to remain there for 10 s. The starting

position was varied pseudorandomly among four quadrants for each trial. On day 7, a probe trial was performed in which the platform was removed, and the mouse was allowed to swim freely for 60 s. Escape latency, swimming path, and time spent in each quadrant were recorded and analyzed using an automated video tracking system (EthoVision XT, Noldus).

Serum creatine kinase (CK) activity assay. Fresh serum was collected from the orbital sinus of mice. According to the manufacturer's guidelines, the CK activity was determined using the Creatine Kinase Activity Assay Kit (Sigma, MAK116). CK activity was expressed as units/liter.

Untargeted Metabolomics in Mouse Muscle Tissue. Three biological replicates of muscle tissue samples of *Gmppb*$^{+/-}$, *Gmppb*$^{P32L/+}$, *Gmppb*$^{R287Q/R287Q}$ and WT were subjected to untargeted metabolomic profiling. Muscle tissue samples were rinsed with pre-chilled PBS, snap-frozen in liquid nitrogen. Frozen tissues (50 mg) were homogenized with steel balls at 60 Hz for 120 s under liquid nitrogen cooling. Metabolites were extracted with 1 mL of pre-chilled methanol:acetonitrile:water (2:2:1, v/v/v) containing 0.1 μg/mL L-2-chlorophenylalanine, vortexed, ice-water sonicated for 10 min, incubated at −20 °C for 1 h, and centrifuged at 13,000×g for 15 min at 4 °C. The extraction was repeated 1 time, supernatants combined, and vacuum-dried. Dried extracts were reconstituted in 100 μL acetonitrile:water (1:1, v/v), filtered through a 0.22 μm membrane, and transferred to LC-MS vials. Quality control (QC) samples were prepared by pooling equal volumes of all sample supernatants. Metabolite separation was performed on an ACQUITY UPLC HSS T3 column (2.1 mm × 100 mm, 1.8 μm) at 40 °C with a mobile phase of 0.1% formic acid in water (A) and 0.1% formic acid in acetonitrile (B), using a gradient elution (0–2 min, 2% B; 2–12 min, 2%–98% B; 12–15 min, 98% B; 15–15.1 min, 98%–2% B; 15.1–18 min, 2% B) at 0.3 mL/min, with a 2 μL injection volume. Mass spectrometric detection was conducted on a Q Exactive HF-X Orbitrap mass spectrometer in positive/negative ESI modes (spray voltage: 3.5 kV/2.8 kV; capillary temperature: 320 °C). Full-scan MS data (m/z 70–1050, 60,000 resolution) and data-dependent MS/MS spectra (15,000 resolution, 20–40 eV collision energy) were acquired for non-targeted metabolomics analysis. Metabolites with VIP > 1 (variable importance in the projection of the first principal component in OPLS-DA) and $p < 0.05$

(Student's t-test) were considered significantly changed. Pathway enrichment analysis was performed using KEGG and MetaboAnalyst databases.

Bulk RNA Sequencing of Cell and Muscle Tissue Samples. For cell samples, adherent cells were washed with pre-chilled PBS, dissociated with trypsin, centrifuged at 300×g for 5 min at 4 °C, and the pellet was lysed with RNAiso Plus (Takara) and stored at −80 °C. Muscle tissue samples were rinsed with pre-chilled PBS, snap-frozen in liquid nitrogen, ground into powder under liquid nitrogen, and lysed with RNAiso Plus. Total RNA was extracted using RNAiso Plus following the manufacturer's protocol. RNA concentration and purity were determined with a NanoDrop ND-2000 spectrophotometer (A260/A280: 1.8–2.1; A260/A230 ≥ 2.0), and integrity was verified using an Agilent 2100 Bioanalyzer (RIN ≥ 7.0). Qualified RNA was used for library construction. mRNA was enriched via oligo (dT) magnetic beads, fragmented into 200–300 bp fragments, and reverse-transcribed into double-stranded cDNA. After end repair, A-tailing, adapter ligation, and PCR amplification, libraries were purified with AMPure XP beads and validated using an Agilent 2100 Bioanalyzer and qPCR. Qualified libraries were sequenced on an Illumina NovaSeq 6000 platform with the PE150 mode. Raw reads were filtered to obtain clean reads for subsequent genome alignment, gene expression quantification (FPKM/TPM), and differential gene expression analysis.

Lectin-based glycoprotein enrichment and LC–MS/MS analysis. GA muscles were ground in liquid nitrogen and lysed with protease inhibitors. Equal amounts (2mg) of clarified protein lysates were incubated with ConA-agarose beads (Vector Laboratories, AL-1003-10) at 4°C overnight. After extensive washing, bound glycoproteins were eluted with 200 mM methyl-α-D-mannopyranoside. Protein samples were transferred to the filter (Millipore, MRCPRT010) and washed with UA buffer three times and 25mM NH_4HCO_3 buffer twice. Trypsin was added (1:50, wt/wt)) and incubated at 37℃ overnight, and the resulting peptides were collected as a filtrate. The peptides were analyzed by OrbitrapTM AstralTM mass spectrometer (Thermo Scientific) connected to an Vanquish Neo system liquid chromatography (Thermo Scientific) in the data independent acquisition (DIA) mode. Precursor ions were scanned at a mass range of 380-980m/z,

MS1 resolution was 240000 at 200 m/z, Normalized AGC Target: 500%, Maximum IT: 5ms. 299 windows were set for DIA mode in MS2 scanning, Isolation Window: 2m/z, HCD Collision Energy: 25ev, Normalized AGC Target: 500%, Maximum IT: 3ms. iRT (indexed retention time) calibration peptides were spiked into the sample. DIA data was analyzed with DIA-NN 1.8.1. Main software parameters were set as follows: enzyme is trypsin, max missed cleavages is 1, fixed modification is carbamidomethyl(C), dynamic modification is oxidation(M) and acetyl (Protein N-term). All reported data were based on 99% confidence for protein identification as determined by false discovery rate (FDR) ≤ 1%.

Electromyography and nerve conduction velocity test. Mice were anesthetized with 2% isoflurane, and body temperature was maintained at 37 °C using a heating pad. CMAPs were recorded using a needle electrode inserted into the gastrocnemius muscle, while the sciatic nerve was stimulated proximally at the sciatic notch and distally at the ankle using bipolar stimulating electrodes. Stimulation was delivered as supramaximal square-wave pulses (0.1 ms duration), and CMAP amplitude and latency were measured using an EMG recorder (Yuyan Instruments, Shanghai, cat# IX-RA-834). Motor nerve conduction velocity was calculated as the distance between the two stimulation sites divided by the latency difference.

In vivo muscle contraction test. Muscle contractile performance was assessed *in vivo* using a nerve-stimulated gastrocnemius contraction assay. Mice were anesthetized with 2% isoflurane, and body temperature was maintained at 37 °C using a thermostatic heating pad. The hindlimb was secured to the platform of an *in vivo* muscle testing system (Aurora Scientific, #1300A), with the foot fixed to a footplate connected to a force transducer. The sciatic nerve was exposed and stimulated via electrodes using 1 ms pulses of supramaximal intensity delivered by a stimulator (Aurora Scientific, #701C). Isometric contractions of the gastrocnemius muscle were recorded in response to stimulation frequencies ranging from 10 Hz to 150 Hz to generate a force–frequency curve. Each contraction was separated by at least 1 min to avoid fatigue.

Grip test. Forelimb muscle strength was measured with a grip strength meter. To assess grip strength, each mouse was held by the tail and its forelimbs firmly grabbed a metal grid. The

mouse was then pulled backward at an even speed until it released its grip. Each mouse was assessed ten times, and the average force in each trial was taken as the grip strength.

Rotarod test. The motor coordination of the mice was analyzed by a rotarod test. Three days before the test, subject mice were exercised for 5min, three times per day. The mice that fell off the rod were put back again to adapt to the test. On the fourth day, mice were subjected to three trials mice reached 40 rpm during 300s, with a 30-minute rest between each trial. The Latency to fall was recorded and 300s is the maximum retention time.

AAV production and injection. For muscle-targeted gene therapy, the MyoAAV 2A-CMV-GMPPB was generated by PackGene and systemically injected into 12-week-old Gmppb$^{P32L+/-}$ mice. This AAV construct carries the expression cassette of *Gmppb*, which is driven by the cytomegalovirus (CMV) promoter. It was reported that MyoAAV administration at low doses results in therapeutic efficacy in disease models and systemically administrated MyoAAV transduces primate muscles highly efficiently[78]. For i.v. injection, a total of 5×10^{11} genome copies (GC) particles of AAV (in a volume of 100μl) were injected into adult *Gmppb*$^{P32L+/-}$ mice (12-week-old) through the tail vein.

MyoAAV viruses were produced by triple-plasmid transfection in human embryonic kidney (HEK) 293 cells and three rounds of CsCl ultracentrifugation purification. The AAV titer was quantitated by real-time PCR using a Fast SYBR Green master mix kit (Applied Biosystems, Foster City, CA, USA) with a pair of primers that amplify a fragment in the CMV promoter. The primers were as follows: forward, 5′- TGGCACCAAAATCAACGGGAC -3′; reverse, 5′- CGTCCAGCTCGACCAGGAT -3′.

Intracellular Ca^{2+} measurements. C2C12 cells were incubated with fluo-4-AM at 37°C in a buffer containing 137 mM NaCl, 4 mM KCl, 1 mM $MgCl_2$,1 mM $CaCl_2$, 10 mM glucose and 10 mM HEPES-NaOH (pH 7.4) for 60 minutes. The tube was maintained in the assay buffer at room

temperature in a SpectraMax i3X Microplate reader. Measure fluorescence using instrument settings appropriate for excitation at 494 nm and emission at 516 nm. The effects of ATP were also measured as above but in the $CaCl_2$-free buffer with the addition of 0.05 mM EGTA. The detailed experiment procedures can be seen in the guidelines of Fluo-4 Direct™ Calcium Assay Kits (Invitrogen, #F10471).

Treatment with CHIR-99021 in vitro and in vivo. In order to verify the effect of canonical Wnt signaling on muscle differentiation, C2C12 myoblasts and Satellite cells were treated with 3 μM CHIR-99021 (Selleck, #S1263) during differentiation. Immuno-fluorescence analysis was performed after 4 days of differentiation. To activate canonical Wnt signaling in vivo, the TA muscles of WT and *Gmppb*$^{P32L/+}$ mice were injected with 10 μM CHIR-99021 (20μl) or saline at 2.5d post injury. The injured TA muscles were then collected for H&E analysis at 5 d post-injury. For continuous treatment, mice received 10 μM CHIR-99021 (20μl) each day at the TA muscles for 7 days before rotarod/grip tests.

Statistical analysis. All experiments included at least three biological replicates. Prism 9.0 (GraphPad) was used for analysis. The areas of fluorescent staining for muscle fibers and nuclei were determined using ImageJ software. Statistical analyses were based on Student's t-test or analysis of variance (ANOVA) with Bonferroni post hoc test or Tukey post-hoc test.

Data Availability

All RNA-seq data sets that were generated in this study have been deposited in the Gene Expression Omnibus, with accession number GSE268450 (https://www.ncbi.nlm.nih.gov/geo/query/acc.cgi?acc=GSE268450) for cell-derived RNA-seq data and GSE268448 (https://www.ncbi.nlm.nih.gov/geo/query/acc.cgi?acc=GSE268448) for RNA-seq data derived from mouse muscle tissues. Untargeted metabolomics data sets have been

deposited in MetaboLights with identifier number MTBLS10214(https://www.ebi.ac.uk/metabolights/reviewer72fc43b3-6b83-429f-b844-74194e1936f5). The mass spectrometry proteomics data have been deposited to the ProteomeXchange Consortium (https://proteomecentral.proteomexchange.org) via the iProX partner repository with the dataset identifier PXD073832 (https://proteomecentral.proteomexchange.org/cgi/GetDataset?ID=PXD073832).. The mutational spectrum data used to generate Fig. 1a and crystal structure of GMPPB used to generate Fig. 2b were generated in prior studies, which are appropriately cited in this article, whenever suitable. Data for all other figures are generated in this study. Source Data are provided as a Source Data file.

Reference

1. Martin, P.T.H.H.F. Glycobiology of neuromuscular disorders. *Glycobiology* **13**, 67R-75 (2003).
2. Francesco Muntoni, M.B., Silvia Torelli and Susan C. Brown. Defective glycosylation in congenital muscular dystrophies.pdf. *Current Opinion in Neurology* **17**, 205-9 (2004).
3. M Brockington *et al.* Mutations in the fukutin-related protein gene (FKRP) identify limb girdle muscular dystrophy 2I as a milder allelic variant of congenital muscular dystrophy MDC1C. *Human molecular genetics* **10**, 2851-9 (2001).
4. Dincer, P. *et al.* A novel form of recessive limb girdle muscular dystrophy with mental retardation and abnormal expression of alpha-dystroglycan. *Neuromuscul Disord* **13**, 771-8 (2003).
5. Godfrey, C. *et al.* Fukutin gene mutations in steroid-responsive limb girdle muscular dystrophy. *Ann Neurol* **60**, 603-610 (2006).
6. Wan, L. *et al.* Structure and assembly of the dystrophin glycoprotein complex. *Nature* **637**, 1252-1260 (2025).
7. Ibraghimov-Beskrovnaya, O. *et al.* Primary structure of dystrophin-associated glycoproteins linking dystrophin to the extracellular matrix. *Nature* **355**, 696-702 (1992).
8. Ervasti, J.M. & Campbell, K.P. A Role for the Dystrophin-Glycoprotein Complex as a Transmembrane Linker between Laminin and Actin.pdf. *The Journal of Cell Biology* **122**, 809-23 (1993).
9. Lapidos, K.A., Kakkar, R. & McNally, E.M. The dystrophin glycoprotein complex: signaling strength and integrity for the sarcolemma. *Circ Res* **94**, 1023-31 (2004).
10. Kanagawa, M. Dystroglycanopathy: From Elucidation of Molecular and Pathological

Mechanisms to Development of Treatment Methods. *Int J Mol Sci* **22**(2021).
11. Oestergaard, S.T. *et al.* Muscle involvement in limb-girdle muscular dystrophy with GMPPB deficiency (LGMD2T). *Neurol Genet* **2**, e112 (2016).
12. Carss, K.J. *et al.* Mutations in GDP-mannose pyrophosphorylase B cause congenital and limb-girdle muscular dystrophies associated with hypoglycosylation of alpha-dystroglycan. *Am J Hum Genet* **93**, 29-41 (2013).
13. Belaya, K. *et al.* Mutations in GMPPB cause congenital myasthenic syndrome and bridge myasthenic disorders with dystroglycanopathies. *Brain* **138**, 2493-504 (2015).
14. Donata Rimoldi, K.E.C.a.L.M.D.L. Reduced mannose incorporation into GDP-mannose and dolichol-linked intermediates of N-glycosylation in hamster liver during vitamin A deficiency. *Molecular and Cellular Biochemistry* **93**, 129-40 (1990).
15. Anna Zakrzewska *et al.* Overexpression of the Gene Encoding GTP:Mannose-1-Phosphate Guanyltransferase, mpg1, Increases Cellular GDP-Mannose Levels and Protein Mannosylation in Trichoderma reesei. *APPLIED AND ENVIRONMENTAL MICROBIOLOGY* **69**, 4383-9 (2003).
16. Jensen, B.S. *et al.* GMPPB-Associated Dystroglycanopathy: Emerging Common Variants with Phenotype Correlation. *Hum Mutat* **36**, 1159-63 (2015).
17. Astrea, G. *et al.* Broad phenotypic spectrum and genotype-phenotype correlations in GMPPB-related dystroglycanopathies: an Italian cross-sectional study. *Orphanet Journal of Rare Diseases* **13**, 170 (2018).
18. Astrea, G. *et al.* Broad phenotypic spectrum and genotype-phenotype correlations in GMPPB-related dystroglycanopathies: an Italian cross-sectional study. *Orphanet J Rare Dis* **13**, 170 (2018).
19. Chiara Panicucci *et al.* Mutations in GMPPB Presenting with Pseudometabolic Myopathy. *JIMD Reports*, 23-31 (2018).
20. Franzka, P. *et al.* GMPPA defects cause a neuromuscular disorder with alpha-dystroglycan hyperglycosylation. *J Clin Invest* **131**(2021).
21. Koehler, K. *et al.* Mutations in GMPPA cause a glycosylation disorder characterized by intellectual disability and autonomic dysfunction. *Am J Hum Genet* **93**, 727-34 (2013).
22. Franzka, P., Mittag, S., Chakraborty, A., Huber, O. & Hubner, C.A. Ubiquitination contributes to the regulation of GDP-mannose pyrophosphorylase B activity. *Front Mol Neurosci* **17**, 1375297 (2024).
23. Hornbeck, P.V. *et al.* PhosphoSitePlus, 2014: mutations, PTMs and recalibrations. *Nucleic Acids Res* **43**, D512-20 (2015).
24. Schurig, M.K. *et al.* Consequences of GMPPB deficiency for neuromuscular development and maintenance. *Front Mol Neurosci* **17**, 1356326 (2024).
25. Grefte, S., Kuijpers-Jagtman, A.M., Torensma, R. & Von den Hoff, J.W. Skeletal muscle development and regeneration. *Stem Cells Dev* **16**, 857-68 (2007).
26. Dayanidhi, S. & Lieber, R.L. Skeletal muscle satellite cells: mediators of muscle growth during development and implications for developmental disorders. *Muscle Nerve* **50**, 723-32 (2014).

27. Hernandez-Hernandez, J.M., Garcia-Gonzalez, E.G., Brun, C.E. & Rudnicki, M.A. The myogenic regulatory factors, determinants of muscle development, cell identity and regeneration. *Semin Cell Dev Biol* **72**, 10-18 (2017).
28. Thornell, L.E. *et al.* Satellite cell dysfunction contributes to the progressive muscle atrophy in myotonic dystrophy type 1. *Neuropathol Appl Neurobiol* **35**, 603-13 (2009).
29. Ribeiro, A.F., Jr. *et al.* Muscle satellite cells and impaired late stage regeneration in different murine models for muscular dystrophies. *Sci Rep* **9**, 11842 (2019).
30. Sacco, A. *et al.* Short telomeres and stem cell exhaustion model Duchenne muscular dystrophy in mdx/mTR mice. *Cell* **143**, 1059-71 (2010).
31. Chang, N.C., Chevalier, F.P. & Rudnicki, M.A. Satellite Cells in Muscular Dystrophy - Lost in Polarity. *Trends Mol Med* **22**, 479-496 (2016).
32. B Wang, J Li & Xiao, X. Adeno-associated virus vector carrying human minidystrophin genes effectively ameliorates muscular dystrophy in mdx mouse model. *Proc Natl Acad Sci U S A* **97**, 13714-9 (2000).
33. Duan, D. Systemic AAV Micro-dystrophin Gene Therapy for Duchenne Muscular Dystrophy. *Mol Ther* **26**, 2337-2356 (2018).
34. Cabrera-Serrano, M. *et al.* Expanding the phenotype of GMPPB mutations. *Brain* **138**, 836-44 (2015).
35. Sarkozy, A. *et al.* Mobility shift of beta-dystroglycan as a marker of GMPPB gene-related muscular dystrophy. *J Neurol Neurosurg Psychiatry* **89**, 762-768 (2018).
36. Luo, S. *et al.* Novel mutations in the C-terminal region of GMPPB causing limb-girdle muscular dystrophy overlapping with congenital myasthenic syndrome. *Neuromuscul Disord* **27**, 557-564 (2017).
37. Montagnese, F. *et al.* Two patients with GMPPB mutation: The overlapping phenotypes of limb-girdle myasthenic syndrome and limb-girdle muscular dystrophy dystroglycanopathy. *Muscle Nerve* **56**, 334-340 (2017).
38. Rodriguez Cruz, P.M. *et al.* Clinical features of the myasthenic syndrome arising from mutations in GMPPB. *J Neurol Neurosurg Psychiatry* **87**, 802-9 (2016).
39. Diana X Bharucha-Goebel , E.N., Sandra Donkervoort , Jahannaz Dastgir , Edythe Wiggs , Thomas L Winder, Steven A Moore , Susan T Iannaccone , Carsten G Bönnemann Intrafamilial variability in GMPPB-associated dystroglycanopathy: Broadening of the phenotype. *Neurology* (2015).
40. Liu, Z. *et al.* GMPPB-congenital disorders of glycosylation associate with decreased enzymatic activity of GMPPB. *Mol Biomed* **2**, 13 (2021).
41. Zheng, L. *et al.* Cryo-EM structures of human GMPPA–GMPPB complex reveal how cells maintain GDP-mannose homeostasis. *Nature Structural & Molecular Biology* **28**, 1-12 (2021).
42. Lvqin Zheng, Z.L., Yan Wang, Fan Yang *et al.* Cryo-EM structures of human GMPPA–GMPPB complex reveal how cells maintain GDP-mannose homeostasis.pdf. *Nature Structural & Molecular Biology* **28**, 1-12 (2021).
43. Schurig, M.K. *et al.* Consequences of GMPPB deficiency for neuromuscular development and maintenance. *Front Mol Neurosci* **17**, 1356326 (2024).

44. Taday, R., Gruneberg, M., DuChesne, I., Reunert, J. & Marquardt, T. Dietary mannose supplementation in phosphomannomutase 2 deficiency (PMM2-CDG). *Orphanet J Rare Dis* **15**, 258 (2020).
45. Schneider, A. *et al.* Successful prenatal mannose treatment for congenital disorder of glycosylation-Ia in mice. *Nature Medicine* **18**, 71-73 (2012).
46. De Palma, C. *et al.* Autophagy as a new therapeutic target in Duchenne muscular dystrophy. *Cell Death Dis* **3**, e418 (2012).
47. Fiacco, E. *et al.* Autophagy regulates satellite cell ability to regenerate normal and dystrophic muscles. *Cell Death Differ* **23**, 1839-1849 (2016).
48. Dube, J., Blaser, S., Guerguerian, A., Hazrati, L. & Yoon, G. P434 Severe GMPPB-related congenital muscular dystrophy with rapidly progressive encephalopathy leading to infantile death. *Neuromuscular Disorders* **33**, S161 (2023).
49. Ervasti JM, C.K. membrane organization of the dystrophin-glycoprotein complex. *Cell* **66**, 1121-31 (1991).
50. JM Ervasti, K.C. A role for the dystrophin-glycoprotein complex as a transmembrane linker between laminin and actin. *The journal of cell biology* **122**, 809–823 (1993).
51. Renzhi Han *et al.* Basal lamina strengthens cell membrane integrity via the laminin G domain-binding motif of alpha-dystroglycan. *Proc Natl Acad Sci U S A* **106**, 12573-9 (2009).
52. Wang, C. *et al.* The role of PDIA3 in myogenesis during muscle regeneration. *Exp Mol Med* **52**, 105-117 (2020).
53. Miller, J.B. Myogenic programs of mouse muscle cell lines: expression of myosin heavy chain isoforms, MyoD1, and myogenin. *The Journal of Cell Biology* **111**, 1149–1159 (1993).
54. Margaret Buckingham , P.W.J.R. Gene Regulatory Networks and Transcriptional Mechanisms that Control Myogenesis. *Developmental cell* **28**, 225-38 (2014).
55. Zhu, Q. *et al.* KDM4A regulates myogenesis by demethylating H3K9me3 of myogenic regulatory factors. *Cell Death Dis* **12**, 514 (2021).
56. Rahman, N.I.A. *et al.* PAX7, a Key for Myogenesis Modulation in Muscular Dystrophies through Multiple Signaling Pathways: A Systematic Review. *Int J Mol Sci* **24**(2023).
57. Moremen, K.W., Tiemeyer, M. & Nairn, A.V. Vertebrate protein glycosylation: diversity, synthesis and function. *Nat Rev Mol Cell Biol* **13**, 448-62 (2012).
58. Senoo, N. *et al.* Glycerophospholipid profile alterations are associated with murine muscle-wasting phenotype. *Muscle Nerve* **62**, 413-418 (2020).
59. Brewer, C.F. & Bhattacharyya, L. Specificity of concanavalin A binding to asparagine-linked glycopeptides. A nuclear magnetic relaxation dispersion study. *Journal of Biological Chemistry* **261**, 7306-7310 (1986).
60. Romano, P.R. *et al.* Development of recombinant Aleuria aurantia lectins with altered binding specificities to fucosylated glycans. *Biochem Biophys Res Commun* **414**, 84-9 (2011).
61. E Lilliu, S.K., X Koenig, M Frieden. Store-Operated Calcium Entry in Skeletal Muscle: What Makes It Different? *Cells* **10**, 2356 (2021).
62. Justyna Róg *et al.* Dystrophic mdx mouse myoblasts exhibit elevated ATP/UTP-evoked

metabotropic purinergic responses and alterations in calcium signalling. *Biochimica et biophysica acta. Molecular basis of disease.* **1865**, 1138-1151 (2019).
63. Onopiuk, M. *et al.* Store-operated calcium entry contributes to abnormal Ca(2)(+) signalling in dystrophic mdx mouse myoblasts. *Arch Biochem Biophys* **569**, 1-9 (2015).
64. Sambasivan, R. *et al.* Pax7-expressing satellite cells are indispensable for adult skeletal muscle regeneration. *Development* **138**, 3647-56 (2011).
65. Relaix, F. & Zammit, P.S. Satellite cells are essential for skeletal muscle regeneration: the cell on the edge returns centre stage. *Development* **139**, 2845-56 (2012).
66. Y., W., J., L. & Y., L. Skeletal Muscle Regeneration in Cardiotoxin-Induced Muscle Injury Models. *International journal of molecular sciences* **23**, 13380 (2022).
67. Lehka, L. & Redowicz, M.J. Mechanisms regulating myoblast fusion: A multilevel interplay. *Semin Cell Dev Biol* **104**, 81-92 (2020).
68. von Maltzahn, J., Chang, N.C., Bentzinger, C.F. & Rudnicki, M.A. Wnt signaling in myogenesis. *Trends Cell Biol* **22**, 602-9 (2012).
69. Girardi, F. & Grand, F.L. Wnt Signaling in Skeletal Muscle Development and Regeneration. *Prog Mol Biol Transl Sci.* **153**, 157-179 (2018).
70. Rudnicki, M.A. & Williams, B.O. Wnt signaling in bone and muscle. *Bone* **80**, 60-66 (2015).
71. Rudolf, A. *et al.* beta-Catenin Activation in Muscle Progenitor Cells Regulates Tissue Repair. *Cell Rep* **15**, 1277-90 (2016).
72. Kim, C.H., Neiswender, H., Baik, E.J., Xiong, W.C. & Mei, L. Beta-catenin interacts with MyoD and regulates its transcription activity. *Mol Cell Biol* **28**, 2941-51 (2008).
73. Cui, S. *et al.* beta-Catenin is essential for differentiation of primary myoblasts via cooperation with MyoD and alpha-catenin. *Development* **146**(2019).
74. Ying Tang , J.C., Johnny Huard, Bing Wang. AAV-directed muscular dystrophy gene therapy. *Expert Opin Biol Ther* **10**, 395-408 (2010).
75. Kei-ichiro Inamori , T.Y.-M., Yuji Hara, Mary E Anderson, Liping Yu, Kevin P Campbell. Dystroglycan Function Requires Xylosyl- and Glucuronyltransferase Activities of LARGE. *Science* **335**, 93-6 (2012).
76. Barresi, R. *et al.* LARGE can functionally bypass alpha-dystroglycan glycosylation defects in distinct congenital muscular dystrophies. *Nat Med* **10**, 696-703 (2004).
77. Asher, D.R. *et al.* Clinical development on the frontier: gene therapy for duchenne muscular dystrophy. *Expert Opin Biol Ther* **20**, 263-274 (2020).
78. Tabebordbar, M. *et al.* Directed evolution of a family of AAV capsid variants enabling potent muscle-directed gene delivery across species. *Cell* **184**, 4919-4938.e22 (2021).
79. Balmer, N.V. *et al.* Epigenetic changes and disturbed neural development in a human embryonic stem cell-based model relating to the fetal valproate syndrome. *Human Molecular Genetics* **21**, 4104-4114 (2012).
80. Stefan Nicolau *et al.* A homozygous mutation in GMPPB leads to centronuclear myopathy with combined pre- and postsynaptic defects of neuromuscular transmission. *Neuromuscul Disord* **29**, 614-617 (2019).
81. Chompoopong, P. & Milone, M. GDP-Mannose Pyrophosphorylase B (GMPPB)-Related

Disorders. *Genes (Basel)* **14**(2023).
82. Deng, Y.T. *et al.* Identifying causal genes for depression via integration of the proteome and transcriptome from brain and blood. *Mol Psychiatry* **27**, 2849-2857 (2022).
83. Wen, H., Zhang, R., Zhong, B., Liu, H. & Liu, C. Cross-Trait Genome-Wide Association Study Identifies Shared Genetic Risk Loci Between COPD and Five Autoimmune Diseases. *Int J Chron Obstruct Pulmon Dis* **20**, 3019-3034 (2025).
84. Dai, Z., Wu, Y., Huang, H. & Zheng, H. Integrating brain proteomes and genetics to identify novel risk genes in chronic widespread musculoskeletal pain. *Sci Rep* **15**, 21999 (2025).
85. Michele, D.E. *et al.* Post-translational disruption of dystroglycan–ligand interactions in congenital muscular dystrophies. *Nature* **418**, 417-421 (2002).
86. Kanagawa, M. *et al.* Impaired viability of muscle precursor cells in muscular dystrophy with glycosylation defects and amelioration of its severe phenotype by limited gene expression. *Human Molecular Genetics* **22**, 3003-3015 (2013).
87. Miyagoe-Suzuki, Y. *et al.* Reduced proliferative activity of primary POMGnT1-null myoblasts in vitro. *Mechanisms of Development* **126**, 107-116 (2009).
88. Kanagawa, M. *et al.* Residual laminin-binding activity and enhanced dystroglycan glycosylation by LARGE in novel model mice to dystroglycanopathy. *Human Molecular Genetics* **18**, 621-631 (2008).
89. Kanagawa, M. *et al.* Impaired viability of muscle precursor cells in muscular dystrophy with glycosylation defects and amelioration of its severe phenotype by limited gene expression. *Hum Mol Genet* **22**, 3003-15 (2013).
90. Ronald D Cohn *et al.* Disruption of Dag1 in Differentiated Skeletal Muscle Reveals a Role for Dystroglycan in Muscle Regeneration. *Cell* **110**, 639-48 (2002).
91. M.A.M. Luz, M.J. Marques & Neto, H.S. Impaired regeneration of dystrophin-deficient muscle fibers is caused by exhaustion of myogenic cells. *Brazilian Journal of Medical and Biological Research* **35**, 691-695 (2002).
92. Rashid, H.-O., Yadav, R.K., Kim, H.-R. & Chae, H.-J. ER stress: Autophagy induction, inhibition and selection. *Autophagy* **11**, 1956-1977 (2015).
93. Kim, J.-H. *et al.* Sex hormones establish a reserve pool of adult muscle stem cells. *Nature Cell Biology* **18**, 930-940 (2016).
94. Lü, Z. *et al.* Large-scale sequencing of flatfish genomes provides insights into the polyphyletic origin of their specialized body plan. *Nature Genetics* **53**, 742-751 (2021).
95. Fecarotta, S. *et al.* Steroid therapy in an alpha-dystroglycanopathy due to GMPPB gene mutations: A case report. *Neuromuscul Disord* **28**, 956-960 (2018).
96. Odom, G.L., Gregorevic, P., Allen, J.M., Finn, E. & Chamberlain, J.S. Microutrophin delivery through rAAV6 increases lifespan and improves muscle function in dystrophic dystrophin/utrophin-deficient mice. *Mol Ther* **16**, 1539-45 (2008).
97. Yu, M. *et al.* Adeno-associated viral-mediated LARGE gene therapy rescues the muscular dystrophic phenotype in mouse models of dystroglycanopathy. *Hum Gene Ther* **24**, 317-30 (2013).
98. Xu, L. *et al.* Adeno-associated virus 9 mediated FKRP gene therapy restores functional

glycosylation of alpha-dystroglycan and improves muscle functions. *Mol Ther* **21**, 1832-40 (2013).

99. Tokuoka, H. *et al.* CDP-ribitol prodrug treatment ameliorates ISPD-deficient muscular dystrophy mouse model. *Nat Commun* **13**, 1847 (2022).
100. Weenink, B., French, P.J., Sillevis Smitt, P.A.E., Debets, R. & Geurts, M. Immunotherapy in Glioblastoma: Current Shortcomings and Future Perspectives. *Cancers (Basel)* **12**(2020).
101. Okada, Y. *et al.* Complementation of placental defects and embryonic lethality by trophoblast-specific lentiviral gene transfer. *Nat Biotechnol* **25**, 233-7 (2007).
102. Schwab, M.E. & MacKenzie, T.C. Prenatal gene therapy. *Clinical Obstetrics and Gynecology* **64**, 876-885 (2021).
103. Behringer, R. *Manipulating the mouse embryo : a laboratory manual*, xxii, 814 pages (Cold Spring Harbor Laboratory Press, Cold Spring Harbor, New York, 2014).
104. Michele, D.E. *et al.* Post-translational disruption of dystroglycan-ligand interactions in congenital muscular dystrophies. *Nature* **418**, 417-22 (2002).
105. Xie, X., Tsai, S.Y. & Tsai, M.J. COUP-TFII regulates satellite cell function and muscular dystrophy. *J Clin Invest* **126**, 3929-3941 (2016).

Acknowledgement

This work was supported by the Startup funding of Fudan University (JIF101074 to Y.W.), the Fundamental Research Funds for the Central Universities (202261051, 202262014 to H.J.). Y.W. is supported by the Pujiang Talent Project (20PJ1400700). We thank Dr. Zhigang Zhang at Fudan University for his assistance in electron microscopy, the colleagues in Keymed Biosciences for their support and advice, Dr. Lunzhi Dai at Sichuan University for his generosity in equipment sharing.

I (Y.W) would like to dedicate this work to the memory of my beloved daughter, Chelsea Zechuan Shia (Oct, 2017-Jul, 2020), who carried compound mutations in *GMPPB*. Chelsea's courage and resilience throughout her life were a profound source of inspiration, prompting me to broaden my research focus beyond cancer studies to include rare diseases, areas that often receive less attention and funding. Though Chelsea did not directly participate in this study, her influence is deeply interwoven with its purpose and direction. Her presence in my life has instilled in me a greater awareness of the challenges faced by patients with rare genetic conditions and a renewed commitment to contributing to research that seeks to improve their lives. In memory of Chelsea, I dedicate this work to all those affected by rare diseases, hoping that our collective efforts in scientific research will one day alleviate their suffering and bring new hope and solutions to their conditions.

Author Contributions Statement

Z.F. and Y.W. conceived and designed the study. Z.F., T.W., T.Q., Y.C., J.Y., H.Y., B.Y., B.G., W.L., S.L. and Y.W. carried out experiments and analyses. C.Z. and Z.Z. performed bioinformatic analyses. Y.L. performed pathological and electron microscopic analyses. L.S., H.J., B.C., Z.Z., X.L. and Y.W. supervised the study. H.J., B.C., X.L. and Y.W. provided funding.

Competing Interests Statement

The authors declare no competing interests.

Figure Legends

Fig. 1 | *Gmppb* mutations result in embryonic lethality. a, Frequency plot of patients with *GMPPB* mutations. **b**, The locations of common point mutation amino acids on the GMPPB protein structure. **c**, Schematic diagram of generation of *Gmppb* mutant mice. Details are described in the Materials and Methods section. The *Gmppb* knock-out mice deleted 303 bp using CRISPR-Cas9 system. The *Gmppb* knock-in mice were generated by homologous recombination with oligo donor. The star in exon 1 denotes P32L missense mutation. The circle in exon 8 denotes R287Q missense mutation. **d**, Photograph images of the uterus of *Gmppb*$^{+/-}$ mice at gestational days 8.5 and 14.5, with red arrows indicating deceased embryos. **e**, Embryos of *Gmppb*$^{+/-}$ mice at E10.5 and E12.5 with different genotypes. Red arrows indicate areas of hemorrhage. **f**, Photograph images of the uterus of *Gmppb*$^{P32L/+}$ mice at gestational days 8.5 and 14.5, with red arrows indicating embryos undergoing developmental failure. **g**, Embryos of *Gmppb*$^{P32L/+}$ mice at E10.5 and E12.5 with different genotypes. Green arrows indicate areas of edema. Source data are provided as a Source Data file.

Fig. 2 | *Gmppb*$^{P32L/+}$ mice display dystrophic phenotype in skeletal muscles.

a, GDP-mannose contents of the GA muscle were determined by LC-MS. Data are presented as mean values ± SD (n=3 female mice per group, biological replicates; two-sided Student’ s t test). **b**, H&E staining of GA muscle of 32-week-old *Gmppb*$^{+/-}$, *Gmppb*$^{P32L/+}$ and *Gmppb*$^{R287Q/R287Q}$ mice, with white arrows indicating centrally nucleated muscle fibers. Scale bars: 100 μm (left) and 50 μm (right). **c**, Quantitative data represent GA muscle fiber diameter. Each data point represents one animal. Data are presented as mean values ± SD (n=3 female mice per group, biological replicates; One-way ANOVA with Bonferroni post hoc test for multiple comparisons). d, Increased centralized nuclei in GA muscle sections of 32-week-old *Gmppb*$^{P32L/+}$ mice. Data are presented as mean values ± SD (n=3 male mice per group, biological replicates; One-way ANOVA with Bonferroni post hoc test for multiple comparisons). Scale bars: 100 μm. **e,** H&E

staining of GA muscle at 16, 32, and 48 weeks of age. *Gmppb*$^{P32L/+}$ mice show increased centralized nuclei in GA muscle compared with control mice as aged (n = 3 male mice per group; One-way ANOVA with Bonferroni post hoc test). Data are presented as mean values ± SD. Scale bars: 100 μm. **f**, Accumulation of scattered autophagic vacuoles containing cytoplasmic debris and electron-dense material was observed in the muscle fibers of *Gmppb*$^{P32L/+}$ mice. Tissue sections were stained with uranyl acetate and lead citrate. Black arrows indicated autophagic vacuoles. ×9700 magnification. The muscle of 32-week-old *Gmppb*$^{P32L/+}$ mice contained a portion of distorted mitochondria (red arrows). ×24500 magnification. Scale bars: 1μm. *: $P < 0.05$, **: $P < 0.01$, ***: $P < 0.001$, ****: $P < 0.0001$, n.s. : not significant, $P > 0.05$. Source data are provided as a Source Data file.

Fig. 3 | *Gmppb*$^{P32L/+}$ mice display neurological manifestations. a, The cerebellum of *Gmppb*$^{P32L/+}$ and WT mice at 3-month and 12-month were subjected to H&E staining (upper, whole tissue (left) and enlarged views for Purkinje cells (right)) and immunofluorescent labeling of Purkinje cells with Calbindin-D28k (bottom). Cell staining positive for Calbindin was counted for 10 independent high-power fields, and the average was taken as a biological replicate. Data are presented as mean values ± SD (n=3 Male mice per group, biological replicates; two-sided Student's t test). **b**, H&E staining of the sciatic nerve cross sections of 12 month *Gmppb*$^{P32L/+}$ and WT mice. **c**, Transmission electron microscopy of the sciatic nerve cross sections of 32-week GmppbP32L/+ and WT mice, stained with uranyl acetate and lead citrate. Red arrows indicate axons with impaired myelination. The G-ratio of axons was calculated and plotted. Data are presented as mean values ± SD (n=3 female mice per group, biological replicates; two-sided Student's t test). Scale bars: 20μm (top) and 5μm (bottom). **d**, EM pictures of *Gmppb*$^{P32L/+}$ sciatic nerves, showing areas where Schwann cells were spatially disoriented. Scale bars: 5μm. **e**, Nerve conduction velocity for the sciatic nerve of mice with indicated genotypes, as measured by in vivo electromyography. Data are presented as mean values ± SD (n=5 male mice per group, biological replicates; One-way ANOVA with Bonferroni post hoc test for multiple comparisons).

f, The compound muscle action potential (CMAP) was plotted as mean±SD. n=5 female mice per group. **g**,16-week and 48-week *Gmppb*$^{P32L/+}$ and WT mice reduced the average time to fall in the rotarod test (*n*= 10 mice per group; male mice; One-way ANOVA with Bonferroni post hoc test). **h**, 16-week and 48-week *Gmppb*$^{P32L/+}$ mice held less weight with their forepaws. Data are presented as mean values ± SD (n=10 mice per group, female mice, biological replicates; One-way ANOVA with Bonferroni post hoc test for multiple comparisons). **i**, The maximal contraction force of *Gmppb*$^{P32L/+}$ and WT mice as measured by in vivo contraction test was plotted. Data are presented as mean values ± SD (n=5 male mice per group, biological replicates; two-sided Student’ s t test). **j,** 30-week-old *Gmppb*$^{P32L/+}$ mice had considerably higher serum CK levels. Data are presented as mean values ± SD (n=5 male mice per group, biological replicates; One-way ANOVA with Bonferroni post hoc test for multiple comparisons). *: $P < 0.05$, **: $P < 0.01$, ***: $P < 0.001$， ****: $P < 0.0001$, n.s.: not significant, $P > 0.05$. Source data are provided as a Source Data file.

Fig. 4 | Abnormal α-dystroglycan glycosylation was observed in *Gmppb*$^{P32L/+}$ mice. a, W Western blots of α-DG glycosylation levels and β-DG expression, with IIH6C4 and VIA4-1 antibodies specifically detecting α-DG glycosylation epitopes. β-tubulin served as loading control. Data are presented as mean values ± SD (n=3 independent experiments, biological replicates, female mice; One-way ANOVA with Bonferroni post hoc test for multiple comparisons). **b**, **c**, **d**, Quantitative data of Western blot experiments for VIA4-1, IIH6C4 and β-DG. Data are presented as mean values ± SD (n=3 mice per group, biological replicates, male mice; One-way ANOVA with Bonferroni post hoc test for multiple comparisons,). **e**, Western blot analyses of total dystroglycan of 30-week-old mice. Data are presented as mean values ± SD (n=3 mice per group, biological replicates; One-way ANOVA with Bonferroni post hoc test for multiple comparisons). **f**, Representative images of IIH6C4 and β-DG reactivity in immunofluorescence-stained cross sections of muscle. Scale bars: 50μm. Quantitative data of α-DG IIH6C4 normalized by β -DG were plotted. Data are presented as mean values ± SD (n=3 mice per group, biological replicates, female mice; two-sided Student’s t test). **g**, Representative

Laminin overlay assay with protein lysates of indicated genotypes, with β-DG as internal control. The relative intensities were plotted. Data are presented as mean values ± SD (n=3 mice per group, biological replicates, female mice; One-way ANOVA with Bonferroni post hoc test for multiple comparisons). **h**, Representative assay of solid-phase laminin-binding activity in WGA-enriched glycoproteins from skeletal muscle. n=3 female mice **i**, Immunofluorescent staining of Laminin in muscle tissues from indicated genotypes. The relative intensities were plotted. Data are presented as mean values ± SD (n=3 mice per group, biological replicates; One-way ANOVA with Tukey post hoc test for multiple comparisons). Scale bar = 100μm. **P*<0.05, ***P*<0.01, *** *P*<0.001, *****P*<0.0001, n.s.: *P* > 0.05. Source data are provided as a Source Data file.

Fig. 5 | Loss of *GMPPB* results in impaired muscle differentiation in vitro. a, Western blotting (upper) and RT-qPCR (bottom) demonstrated GMPPB knockout in C2C12 cells by CRISPR-Cas9 system. Data are presented as mean values ± SD (n=3 independent cell cultures, biological replicates; two-sided Student’ s t test). **b,** CCK8 assay showed that knockout of *GMPPB* had no influence on the ability of cell proliferation of C2C12 cells. (n=3 independent cell cultures). **c**, Concentration of GDP-mannose in *Gmppb*-KO and wild-type C2C12 cells by LC-MS. The peak area was quantified and represented as mean±SD on bar graphs (n=3 each group, Student’s t test). **d**, Temporal change in apoptosis rate was determined using the Annexin V/PI staining assay during the differentiation of Gmppb-KO and wild-type C2C12 cells. Data are presented as mean values ± SD (n=3 independent experiments, biological replicates; two-way ANOVA with Bonferroni post hoc test for time and genotype effects). D0, day0; D1, day1; D3, day3; D5, day5. **e**, Immunofluorescence staining for MyHC in *Gmppb*-KO and wild-type C2C12 cells cultured for 7d in differentiation medium. (n=3) Scale bars: 50μm. *GMPPB* knockout caused a significant decrease in myotube diameters (**f**) and fusion index (**g**) compared to wild-type C2C12 cells. **h, i, j, k,** Temporal expression of myogenic regulatory factors (MRFs) Pax7 (**h**), MyoD (**i**), Myf5 (**j**), and Myogenin (**k**) in *Gmppb*-KO C2C12 cells during cell differentiation compared with *Gmppb*-WT cells. **l, m, n, o**, Quantified relative signal intensity of Pax7 (**l**), MyoD (**m**), Myf5 (**n**), and

Myogenin (**o**) during differentiation. Vinculin or β-tubulin as loading control. Data are presented as mean values ± SD (n=3 independent cell cultures, biological replicates; two-way ANOVA with Bonferroni post hoc test for time and genotype effects). ns: $P > 0.05$, **P<0.01, ****P<0.0001. Source data are provided as a Source Data file.

Fig. 6 | *GMPPB* knockout or mutant result in alterations of gene expression profile and autophagic/mitochondrial defects. a, Plot for Gene Ontology (GO) function enrichment analysis of differentially expressed genes (DEGs) from Gmppb-KO and wild-type C2C12 cells. Statistical test: Fisher's exact test with false discovery rate (FDR) correction for multiple comparisons. **b**, Circle plot for GO enrichment analysis from RNA sequencing of skeletal muscles of *Gmppb*$^{+/-}$, *Gmppb*$^{P32L/+}$and *Gmppb*$^{R287Q/R287Q}$ mice. **c**, GSEA enrichment profiles of mannose type O-Glycan biosynthesis and N-glycan biosynthesis. Statistical test: Kolmogorov-Smirnov test with FDR correction for multiple comparisons. **d**, GSEA enrichment profile of neuromuscular junction-associated pathways. Statistical test: Kolmogorov-Smirnov test with FDR correction for multiple comparisons. **e**, GSEA enrichment of unfolded protein response and reactive oxygen species pathway. Statistical test: Kolmogorov-Smirnov test with FDR correction for multiple comparisons. **f**, Western blots of p62 (upper), LC3 (middle) and Vinculin (bottom, loading control) in protein lysates of muscle from indicated genotypes. The relative LC3-II:LC3 I ratio was plotted. Data are presented as mean values ± SD (n=3 male mice per group, biological replicates; One-way ANOVA with Bonferroni post hoc test for multiple comparisons). **g**, Immunofluorescent images of C2C12 cells stained with MitoTracker. Scale bars: 50μm. (n=3 independent cell cultures, biological replicates). **h**, Identified scatter plot of ConA-enriched glycoprotein subjected to LC-MS identification and quantification. P values were either indicated or represented as ****: $P<0.0001$, n.s.: $P > 0.05$. Source data are provided as a Source Data file.

Fig. 7 | Satellite cells of *Gmppb*$^{P32L/+}$ mice displayed a diminished ability to differentiate. a, Satellite cells were isolated through flow cytometry analysis of CD31, CD45, Sca1, and VCAM1

expression in skeletal muscle-derived single cell suspension. Image(s) provided by Servier Medical Art (https://smart.servier.com), licensed under CC BY 4.0 (https://creativecommons.org/licenses/by/4.0/).**b**, Immunofluorescence staining for MyHC in FACS-purified satellite cells from WT and *Gmppb*$^{P32L/+}$ mice cultured for 4 d in proliferation medium followed by 4 d in differentiation medium. n = 3 cell cultures in each group. Scale bars: 100μm. **c**, Immunofluorescence staining for MyoG in FACS-purified satellite cells from WT and *Gmppb*$^{P32L/+}$ mice cultured for 4 d in proliferation medium followed by 3 d in differentiation medium. n = 3 cell cultures in each group. Scale bars: 100μm. **d**, Fusion index was calculated as the average number of nuclei in MyHC-positive cells divided by the total number of nuclei. Data are presented as mean values ± SD (n=3 independent cell cultures per group, biological replicates; two-sided Student’ s t test). ***P<0.001. **e**, Immunofluorescence intensities of MyoG positive cells were quantified by ImageJ in the satellites groups as indicated above. Error bars represent the mean ± SD. ***P < 0.001; Student’s t-test. **f**, Western blot analysis of satellite cells from WT and GmppbP32L/+ mice muscle at day 1 and 5 of differentiation. β-tubulin was used as a loading control. **g, h**， The histogram indicated MyHC and MyoG, protein levels normalized to β-tubulin signals. (n=3 independent experiments; Two-way ANOVA with Bonferroni post hoc test). Error bars: mean±SD. n.s.: not significant, ***$P < 0.001$, ****$P < 0.0001$. Source data are provided as a Source Data file. The vial image in Fig. 7a and the dish image in Fig. 7b are adopted from Servier Medical Art (https://smart.servier.com), licensed under CC BY 4.0 (https://creativecommons.org/licenses/by/4.0/).

Fig. 8 | *Gmppb*$^{P32L/+}$ mice display impaired regeneration post CTX-induced muscle injury. **a**, Schematic diagram of cardiotoxin (CTX)-induced injury on wild type and *Gmppb*$^{P32L/+}$ mice skeletal muscle tissues. 30-week-old WT and *Gmppb*$^{P32L/+}$ mice were injected intramuscularly with CTX, and the skeletal muscles were analyzed 3, 5, and 14 days (d) after injury. The mouse image is adopted from Servier Medical Art (https://smart.servier.com), licensed under CC BY

4.0 (https://creativecommons.org/licenses/by/4.0/). **b**, H&E staining of injured and contralateral TA muscles (CTL) from WT and *Gmppb*$^{P32L/+}$ mice at 3, 5, and 14 day post-injury. (n=3 mice per group). Scale bars: 100μm. **c**, The number of myofibers containing two or more centrally located nuclei per field and **d**, the average cross-sectional area (CSA) of regenerating myofibers post-injury. n=3 in each group. **e**, Distribution of myofiber CSAs at day 5 post-injury. Data are presented as mean values ± SD (n=3 female mice per group, biological replicates). **f**, Serum CK levels of *Gmppb*$^{P32L/+}$ and WT mice at day 0, 3, 5 and 14 post-injury. Data are presented as mean values ± SD (n=3 female mice per group, biological replicates; two-way ANOVA with Bonferroni post hoc test for time and genotype effects). **g**, Immunofluorescence analysis of eMyHC+ fibers in TA muscles of WT and *Gmppb*$^{P32L/+}$ mice at 5 days post injury. Scale bar: 50μm. Percentage of eMyHC^{+} fibers per laminin^{+} myofiber in 5d-injured TA muscle of WT and *Gmppb*$^{P32L/+}$ mice. n=3 in each group for eMyHC and laminin staining. Error bars represent the mean±SD. *$P < 0.05$, **$P < 0.01$, ***$P < 0.001$， ****$P < 0.0001$, n.s.: $P > 0.05$; Student's t-test. Source data are provided as a Source Data file.

Fig. 9 | Impairment of myogenic development is restored by activating Wnt signaling. a, Heatmap of the changes in selected gene expression levels in *GMPPB*-KO and WT C2C12 cells by RNA-seq. **b,** KEGG enrichment of glycoproteomic analysis in the Wnt signaling pathway. Threshold was set at $Log_{10}(0.05) > 1.3$. Statistical test: Fisher's exact test with FDR correction for multiple comparisons. **c**, Expression analysis of Wnt signaling pathway genes and myogenic genes in Gmppb-KO and wild-type C2C12 cells at 5d in differentiation medium using qRT-PCR. Data are presented as mean values ± SD (n=3 independent cell cultures, biological replicates; two-sided Student's t test). **d**, Western blot analysis of active β-catenin abundance (upper) in the nuclear fraction extracted from Gmppb-KO and Gmppb-WT C2C12 cells in proliferation medium and after 5 and 7d in differentiation medium. Laminin B1 (bottom) serves as internal control. Data are presented as mean values ± SD (n=3 independent cell cultures, biological

replicates; two-way ANOVA with Bonferroni post hoc test for time and genotype effects). **e**, Immunofluorescence staining for MyHC in C2C12 cells treated with CHIR-99021 or DMSO after 5 d in differentiation medium. A fusion index was calculated as the number of fibers containing a minimum of two nuclei divided by total nuclei. Data are presented as mean values ± SD (n=3 independent cell cultures per group, biological replicates; two-way ANOVA with Bonferroni post hoc test for treatment and genotype effects). Scale bars: 50 μm. **f**, Immunofluorescence staining for MyHC in FACS-purified satellite cells from WT and *Gmppb*$^{P32L+/-}$ mice treated with treated with CHIR-99021 or DMSO and then cultured for 4 d in differentiation medium. n=3 independent cell cultures per group. Scale bars: 50μm. fusion index are shown on the right. **g**, Intramuscular injection of CHIR-99021 or saline at 2.5 d post injury and H&E staining of injured TA muscles of WT and *Gmppb*$^{P32L/+}$ mice at 5 d post-injury. Average cross-sectional area (CSA) of regenerating myofibers is plotted. Data are presented as mean values ± SD (n=3 male mice per group, biological replicates; two-way ANOVA with Bonferroni post hoc test for treatment and genotype effects). Scale bars: 100 μm. Source data are provided as a Source Data file.

Fig. 10 | The myopathy phenotype is ameliorated by AAV-GMPPB treatment.

a, Representative IIH6C4 immunofluorescence (upper) and H&E staining (bottom) images after AAV-mediated gene transfer. Scale bars: 100μm. **b**, Quantification of IIH6C4 relative intensity from immunofluorescence in (**a**). Error bars represent mean±SD. n=3 female mice per group. **c**, Quantification of proportion of centrally-nucleated myofibers is represented as the mean±SD. n=3 female mice per group. **d**, α-DG glycosylation was measured with IIH6C4 and VIA4 antibody and β-DG expression using Western blot. β-actin served as loading control. **e**, Western blots of nuclear β-catenin (upper) and histone H3 (bottom, loading control) in *Gmppb*$^{P32L/+}$ GA muscles receiving CHIR or AAV treatment. n=3 female mice per group. **f**, Quantified relative intensities of β-catenin were plotted. Data are presented as mean values ± SD (n=3 mice per group). **g** and **h**, Temporal changes in rotarod test (P=0.0049 at 20 weeks, P=0.0003 at 28 weeks)

and grip test (P=0.0107 at 20 weeks, P=0.0054 at 28 weeks). Data are presented as mean values ± SD (n=3 female mice per group, biological replicates; two-way ANOVA with Bonferroni post hoc test for time and treatment effects). **i,** Serum CK activity of *Gmppb*$^{P32L/+}$ mice receiving AAV treatment at 28-week. Data are presented as mean values ± SD (n=7 female mice per group, biological replicates; One-way ANOVA with Bonferroni post hoc test for multiple comparisons). **j**, Representative photomicrographs of 5d-injured TA muscle sections of WT mice and the *Gmppb*$^{P32L+/-}$ mice with or without AAV therapy after immunostaining for eMyHC (red) and laminin (green) protein. Nuclei were counterstained with DAPI (blue). Scale bars: 100μm. **k**, Percentage of eMyHC+ fibers per laminin+ myofiber in 5d-injured TA muscle of WT mice and GmppbP32L/+ mice with or without AAV therapy. Data are presented as mean values ± SD (n=3 mice per group, biological replicates; One-way ANOVA with Bonferroni post hoc test for multiple comparisons). Error bars represent the means ±SD. Source data are provided as a Source Data file.

Editorial Summary

Here, in mouse models of GMPPB dystroglycanopathy, the authors show that impaired glycosylation disrupts muscle integrity and triggers broader cellular stress. They identify actionable pathways that improve muscle function, suggesting therapeutic strategies.

Peer review information: *Nature Communications* thanks Patricia Franzka, and the other, anonymous, reviewer(s) for their contribution to the peer review of this work. A peer review file is available.

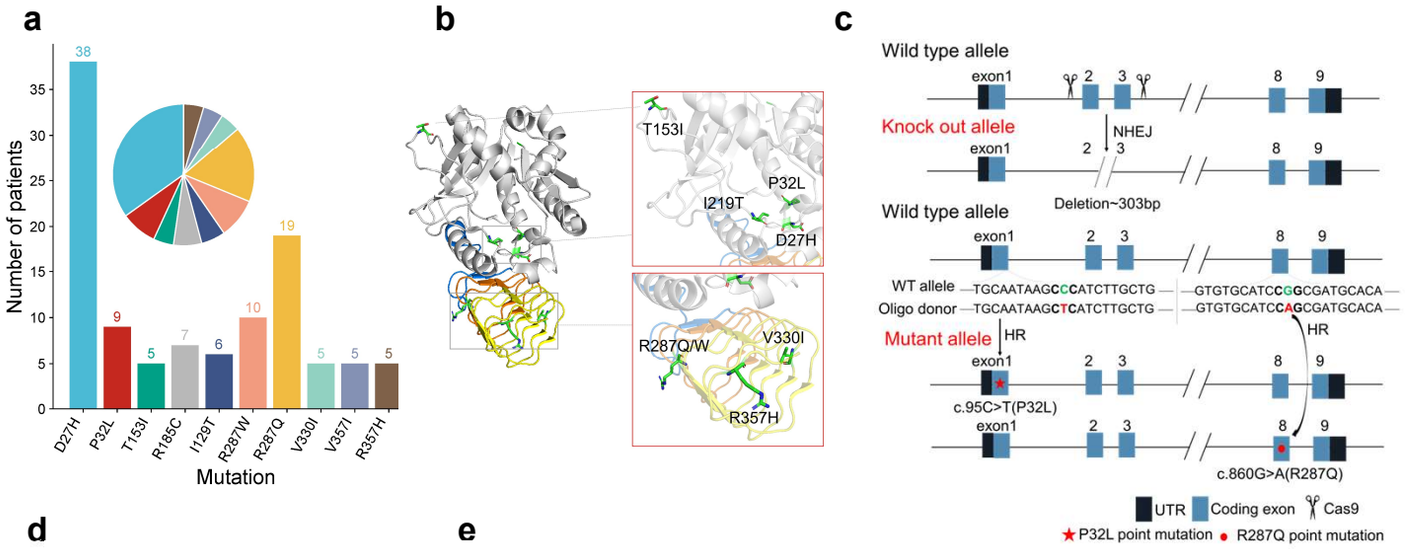
a
Number of patients
Mutation
D27H
P32L
T153I
R185C
I129T
R287W
R287Q
V330I
V357I
R357H
38
9
5
7
6
10
19
5
5
5
b
T153I
P32L
I219T
D27H
R287Q/W
V330I
R357H
c
Wild type allele
exon1
Knock out allele
NHEJ
Deletion~303bp
WT allele
Oligo donor
Mutant allele
HR
c.95C>T(P32L)
c.860G>A(R287Q)
UTR
Coding exon
Cas9
P32L point mutation
R287Q point mutation

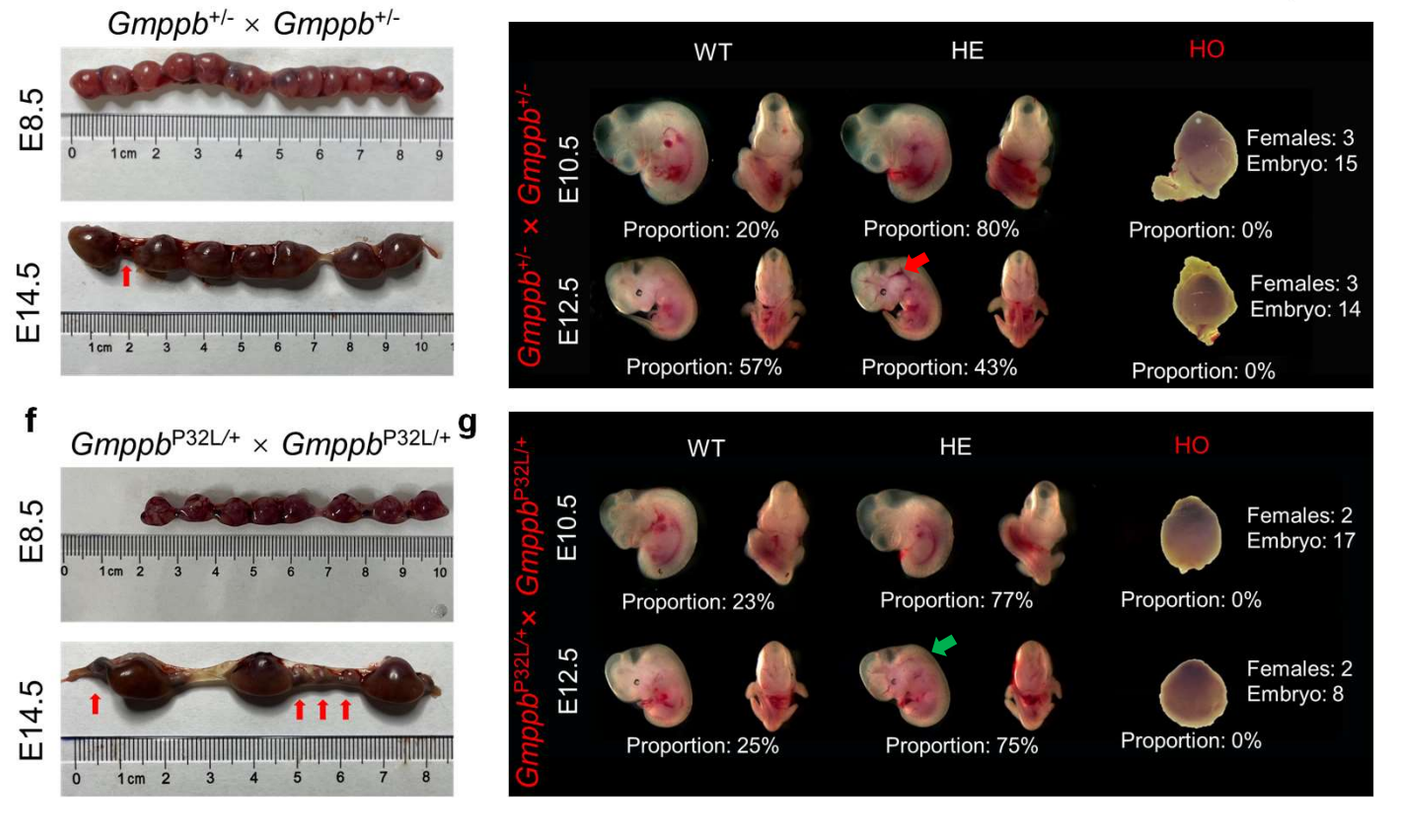
d
Gmppb+/- × Gmppb+/-
E8.5
E14.5
e
WT
HE
HO
Gmppb+/- × Gmppb+/-
E10.5
E12.5
Proportion: 20%
Proportion: 80%
Proportion: 0%
Females: 3
Embryo: 15
Proportion: 57%
Proportion: 43%
Proportion: 0%
Females: 3
Embryo: 14
f
GmppbP32L/+ × GmppbP32L/+
E8.5
E14.5
g
WT
HE
HO
GmppbP32L/+ × GmppbP32L/+
E10.5
E12.5
Proportion: 23%
Proportion: 77%
Proportion: 0%
Females: 2
Embryo: 17
Proportion: 25%
Proportion: 75%
Proportion: 0%
Females: 2
Embryo: 8

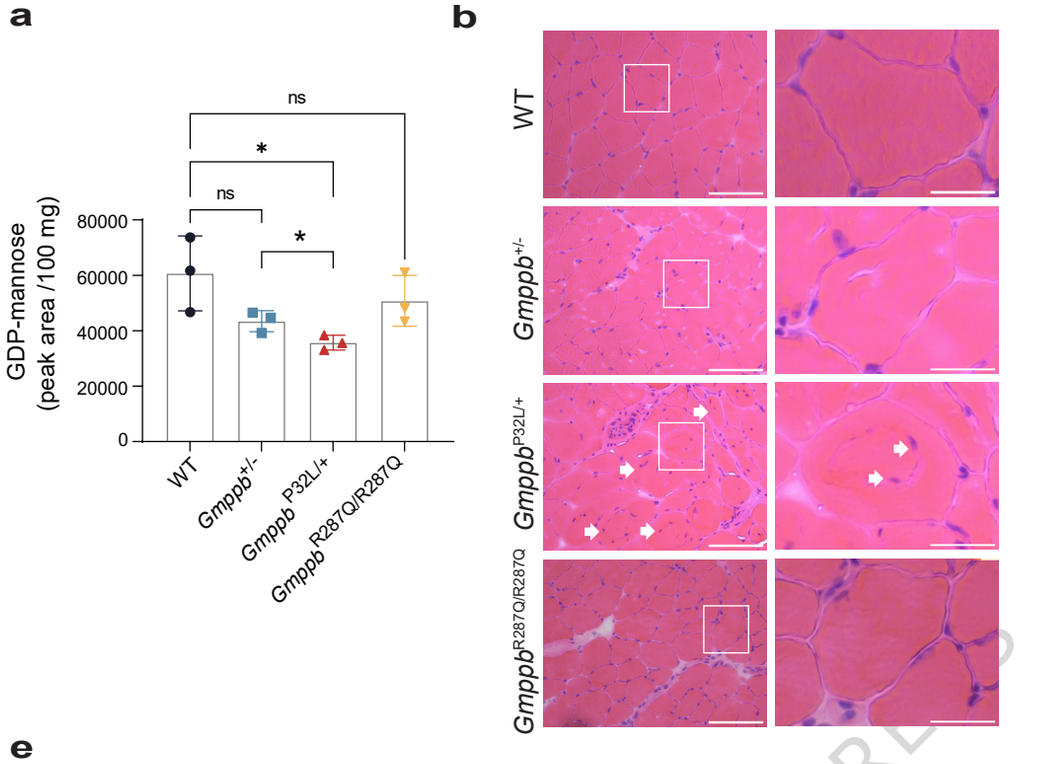
a
GDP-mannose
(peak area /100 mg)
80000
60000
40000
20000
0
ns
*
ns
*
WT
Gmppb+/-
Gmppb P32L/+
Gmppb R287Q/R287Q
b
WT
Gmppb+/-
GmppbP32L/+
GmppbR287Q/R287Q
c
Myofiber diameter(um)
65
60
55
50
45
40
ns
**
ns
WT
Gmppb+/-
GmppbP32L/+
GmppbR287Q/R287Q
d
Centrally nucleated
myofibers (%)
40
30
20
10
0
ns
****
ns
WT
Gmppb+/-
GmppbP32L/+
GmppbR287Q/R287Q

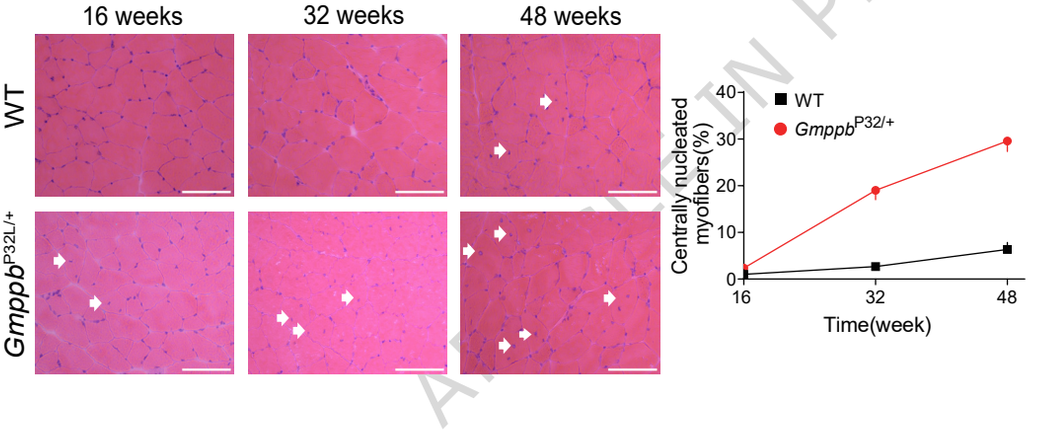
e
16 weeks
32 weeks
48 weeks
WT
GmppbP32L/+
Centrally nucleated
myofibers(%)
40
30
20
10
0
WT
GmppbP32/+
16
32
48
Time(week)

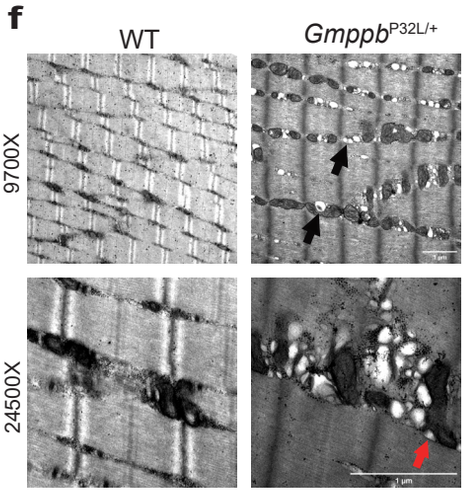
f
WT
GmppbP32L/+
9700X
24500X

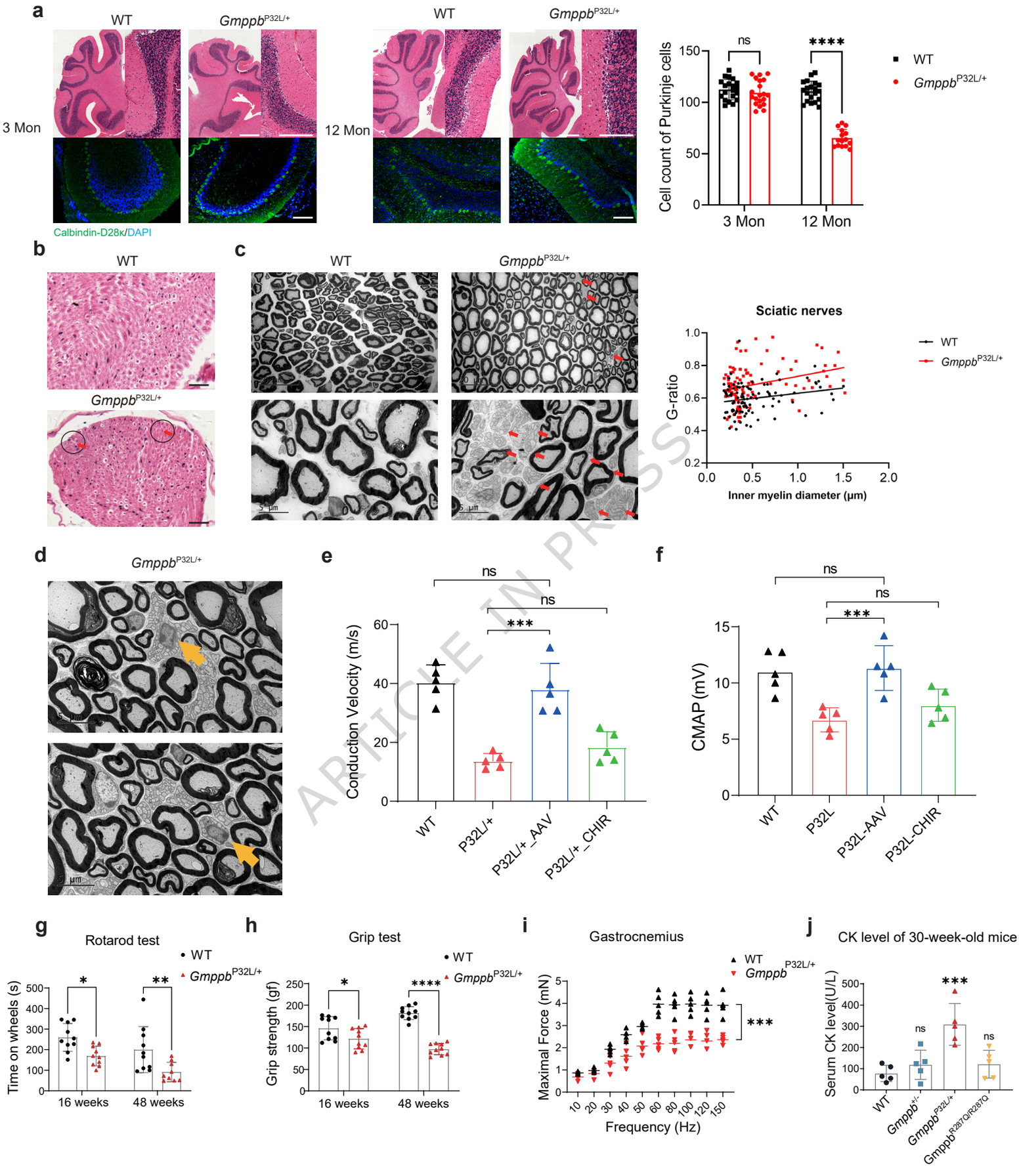

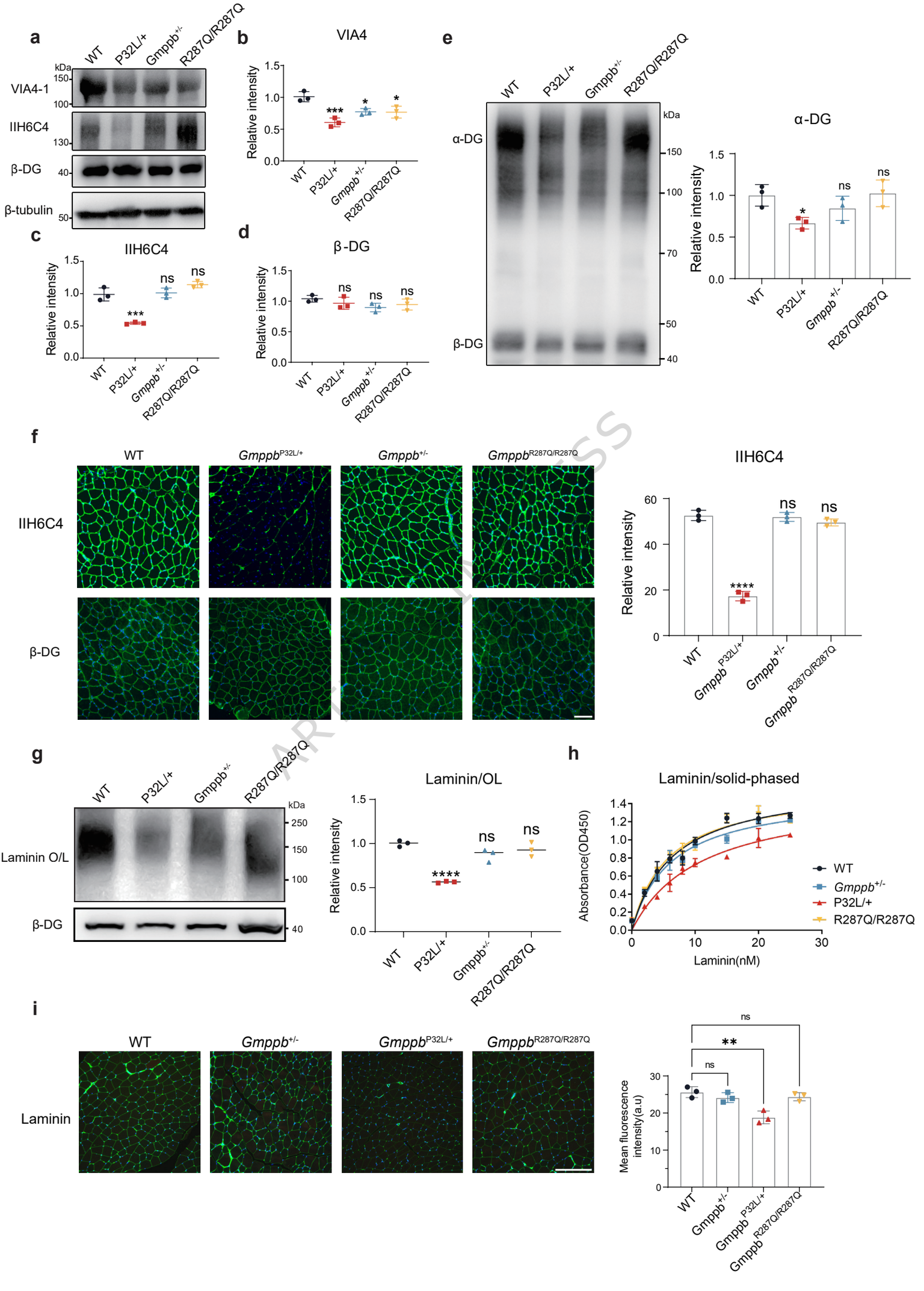
a
WT
P32L/+
Gmppb+/-
R287Q/R287Q
kDa
VIA4-1
150
100
IIH6C4
130
β-DG
40
β-tubulin
50
b
VIA4
Relative intensity
1.5
1.0
0.5
0.0
***
*
*
c
IIH6C4
ns
ns
d
β-DG
e
α-DG
β-DG
150
100
70
50
40
f
WT
Gmppb P32L/+
Gmppb+/-
Gmppb R287Q/R287Q
IIH6C4
β-DG
60
40
20
0
****
g
Laminin O/L
β-DG
250
150
100
40
Laminin/OL
h
Laminin/solid-phased
Absorbance(OD450)
1.4
1.2
1.0
0.8
0.6
0.4
0.2
0.0
0
10
20
30
Laminin(nM)
WT
Gmppb+/-
P32L/+
R287Q/R287Q
i
Laminin
Mean fluorescence intensity(a.u)
**

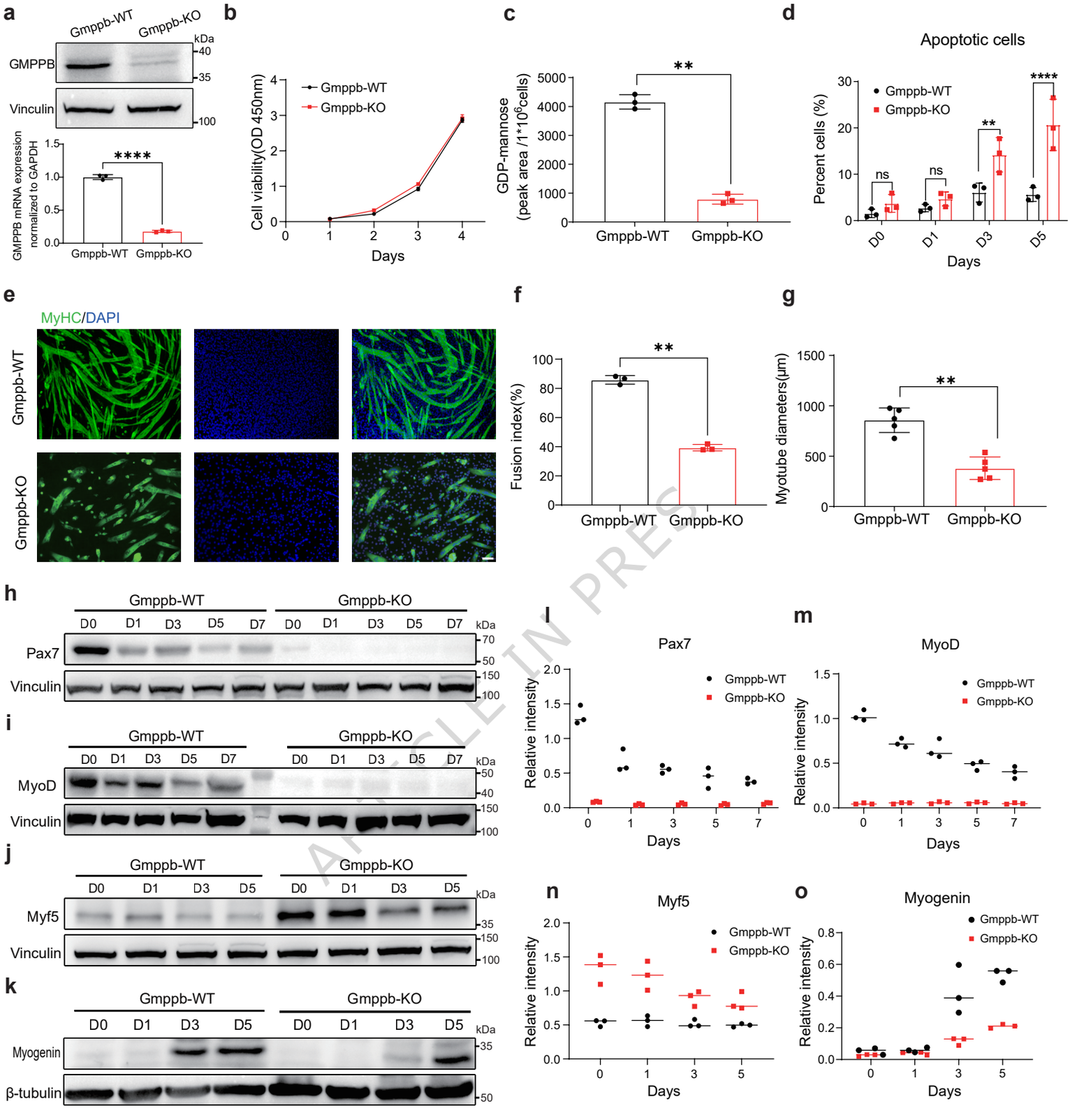

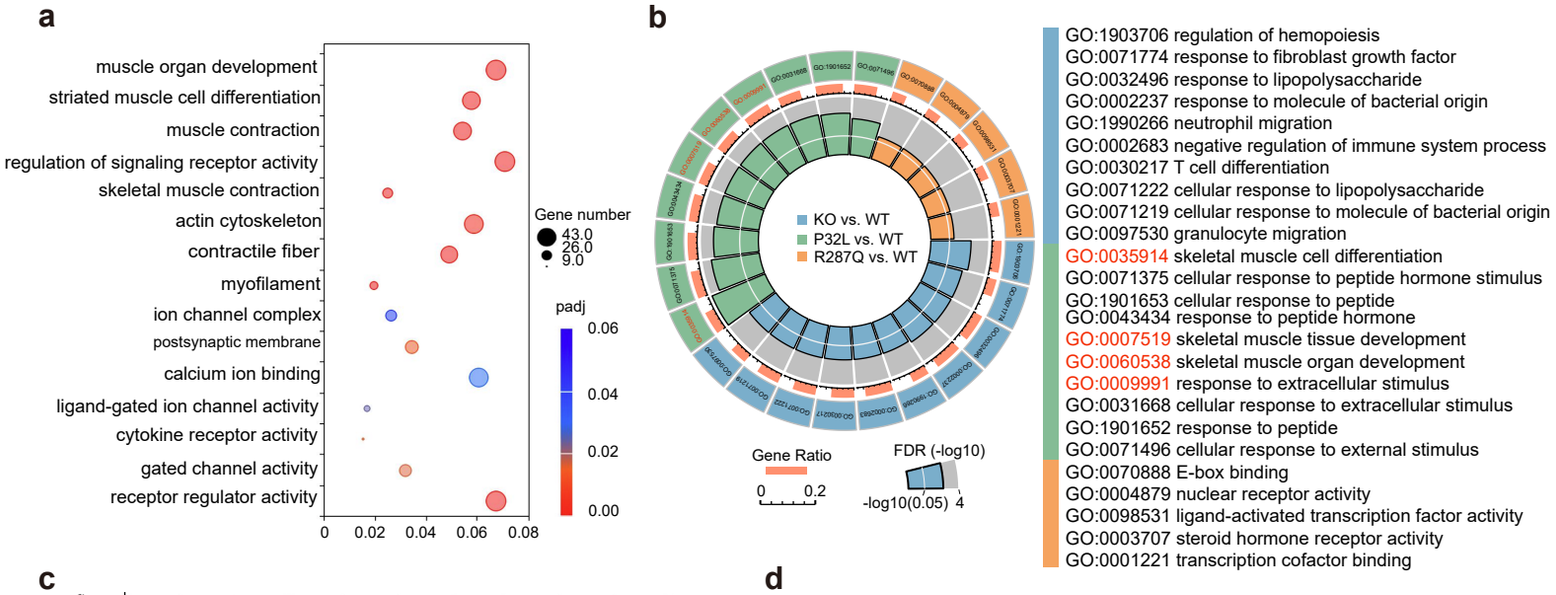
a
muscle organ development
striated muscle cell differentiation
muscle contraction
regulation of signaling receptor activity
skeletal muscle contraction
actin cytoskeleton
contractile fiber
myofilament
ion channel complex
postsynaptic membrane
calcium ion binding
ligand-gated ion channel activity
cytokine receptor activity
gated channel activity
receptor regulator activity
0 0.02 0.04 0.06 0.08
Gene number
43.0
26.0
9.0
padj
0.06
0.04
0.02
0.00
b
KO vs. WT
P32L vs. WT
R287Q vs. WT
Gene Ratio
0 0.2
FDR (-log10)
-log10(0.05) 4
GO:1903706 regulation of hemopoiesis
GO:0071774 response to fibroblast growth factor
GO:0032496 response to lipopolysaccharide
GO:0002237 response to molecule of bacterial origin
GO:1990266 neutrophil migration
GO:0002683 negative regulation of immune system process
GO:0030217 T cell differentiation
GO:0071222 cellular response to lipopolysaccharide
GO:0071219 cellular response to molecule of bacterial origin
GO:0097530 granulocyte migration
GO:0035914 skeletal muscle cell differentiation
GO:0071375 cellular response to peptide hormone stimulus
GO:1901653 cellular response to peptide
GO:0043434 response to peptide hormone
GO:0007519 skeletal muscle tissue development
GO:0060538 skeletal muscle organ development
GO:0009991 response to extracellular stimulus
GO:0031668 cellular response to extracellular stimulus
GO:1901652 response to peptide
GO:0071496 cellular response to external stimulus
GO:0070888 E-box binding
GO:0004879 nuclear receptor activity
GO:0098531 ligand-activated transcription factor activity
GO:0003707 steroid hormone receptor activity
GO:0001221 transcription cofactor binding

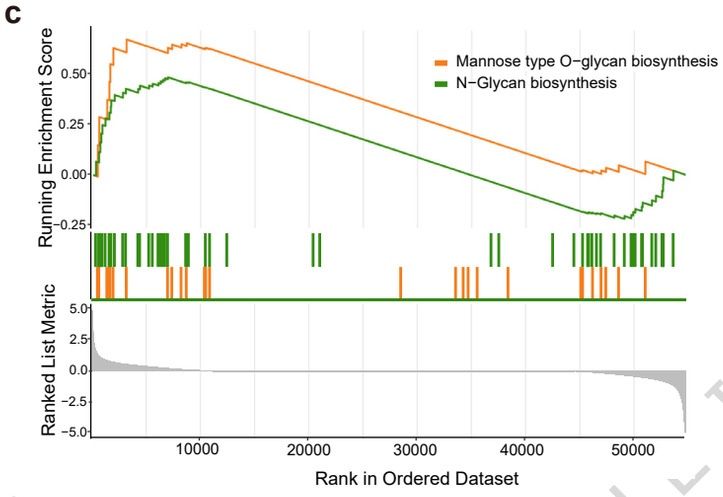
c
Mannose type O−glycan biosynthesis
N−Glycan biosynthesis
Running Enrichment Score
Ranked List Metric
Rank in Ordered Dataset

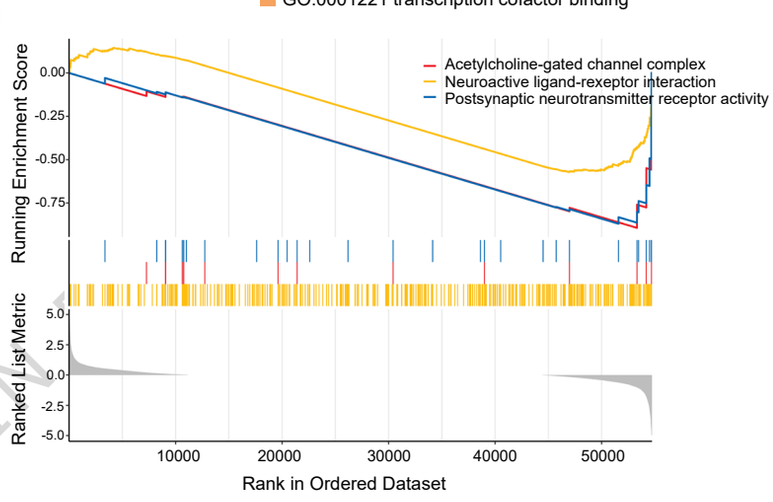
d
Acetylcholine-gated channel complex
Neuroactive ligand-rexeptor interaction
Postsynaptic neurotransmitter receptor activity
Running Enrichment Score
Ranked List Metric
Rank in Ordered Dataset

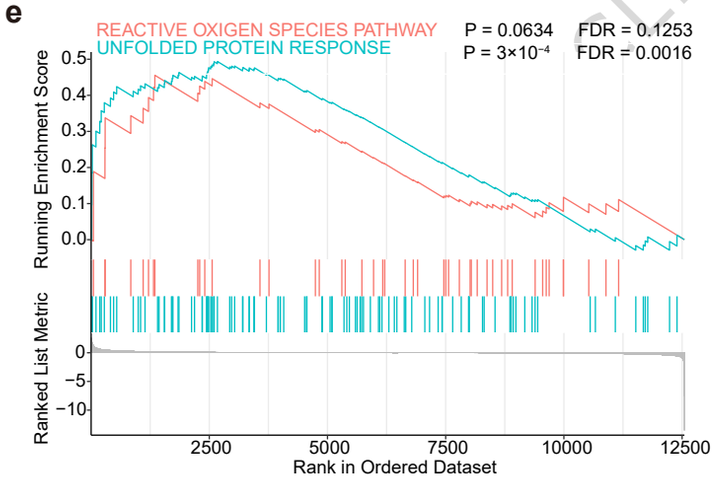
e
REACTIVE OXIGEN SPECIES PATHWAY
P = 0.0634 FDR = 0.1253
UNFOLDED PROTEIN RESPONSE
P = 3×10⁻⁴ FDR = 0.0016
Running Enrichment Score
Ranked List Metric
Rank in Ordered Dataset

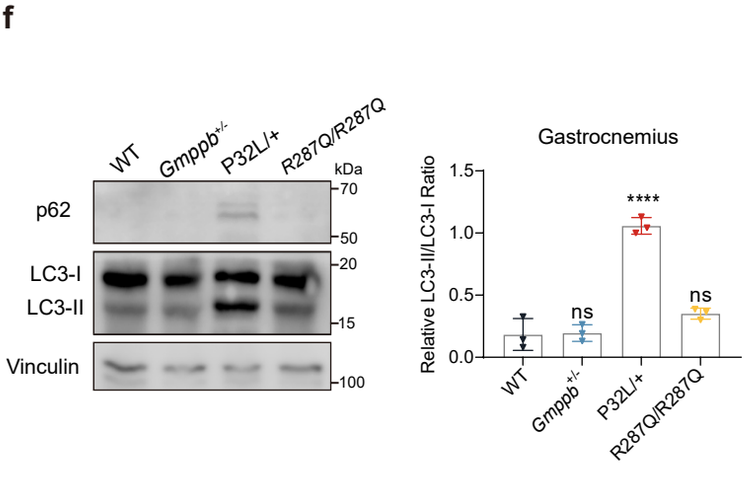
f
WT
Gmppb+/-
P32L/+
R287Q/R287Q
kDa
p62
LC3-I
LC3-II
Vinculin
70
50
20
15
100
Gastrocnemius
Relative LC3-II/LC3-I Ratio
****
ns
ns

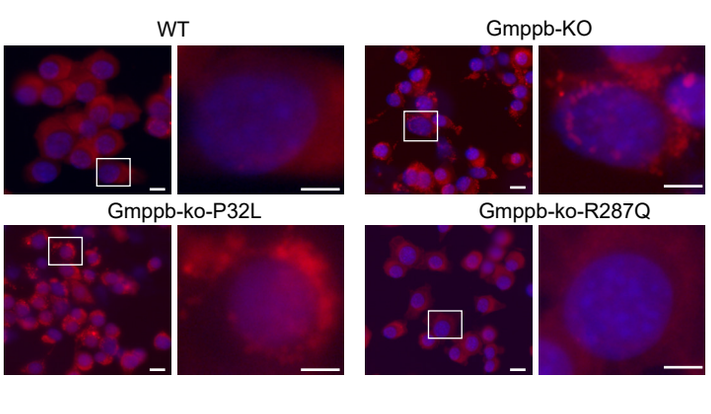
g
WT
Gmppb-KO
Gmppb-ko-P32L
Gmppb-ko-R287Q

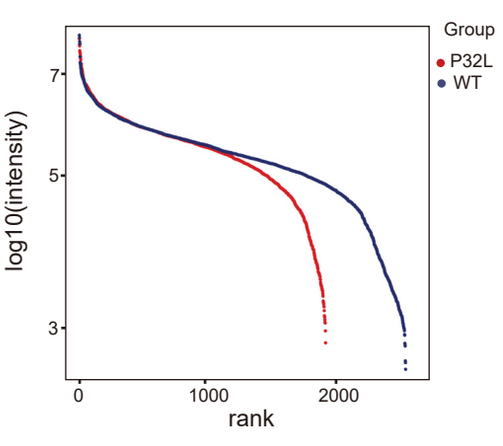
h
log10(intensity)
rank
Group
P32L
WT

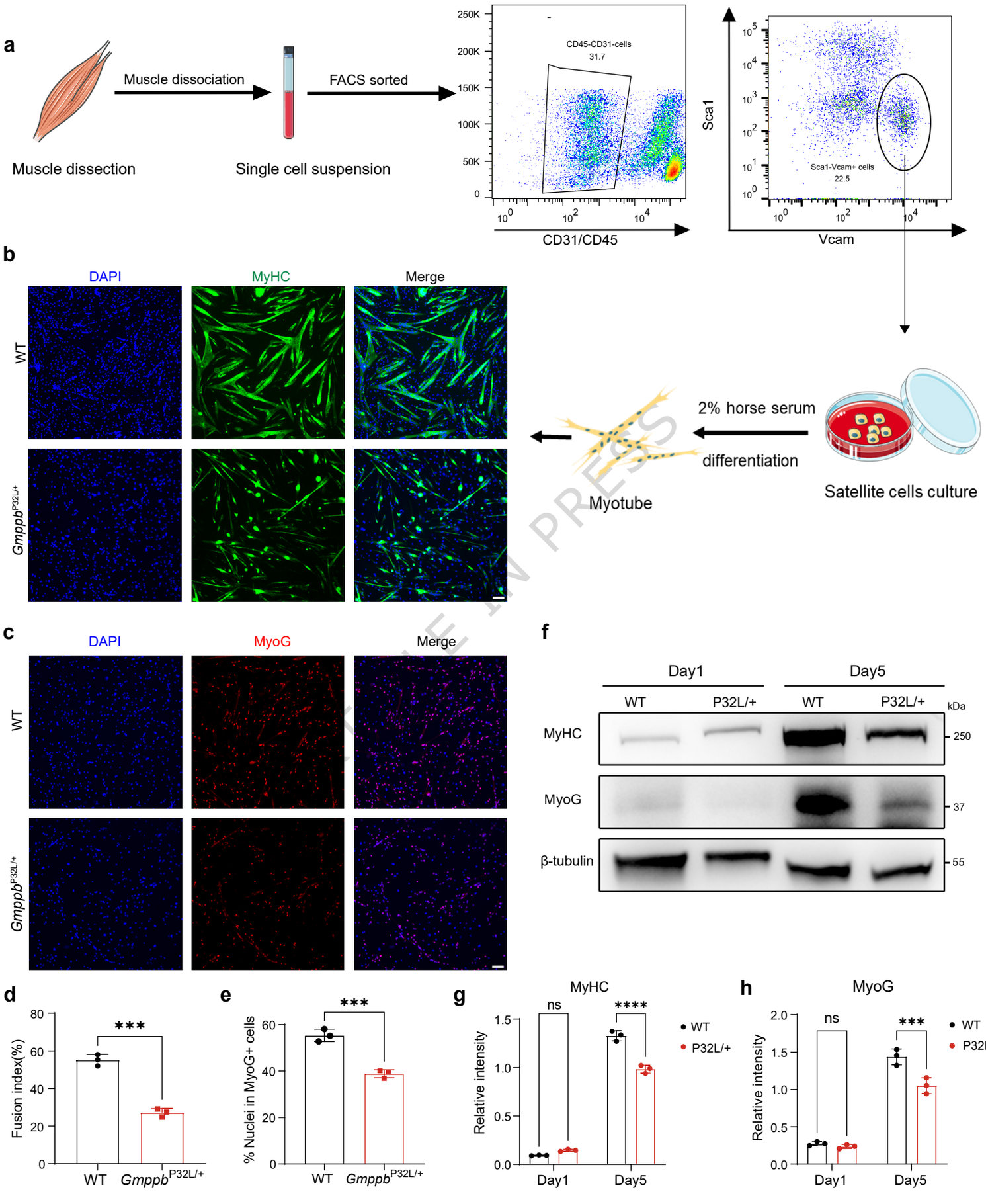
a
Muscle dissociation
FACS sorted
Muscle dissection
Single cell suspension
CD45-CD31-cells
31.7
CD31/CD45
Sca1
Sca1-Vcam+ cells
22.5
Vcam
b
DAPI
MyHC
Merge
WT
Gmppb P32L/+
2% horse serum
differentiation
Myotube
Satellite cells culture
c
DAPI
MyoG
Merge
WT
Gmppb P32L/+
f
Day1
Day5
WT
P32L/+
WT
P32L/+
kDa
MyHC
250
MyoG
37
β-tubulin
55
d
Fusion index(%)
***
WT
Gmppb P32L/+
e
% Nuclei in MyoG+ cells
***
WT
Gmppb P32L/+
g
MyHC
Relative intensity
ns
****
WT
P32L/+
Day1
Day5
h
MyoG
Relative intensity
ns
***
WT
P32L/+
Day1
Day5

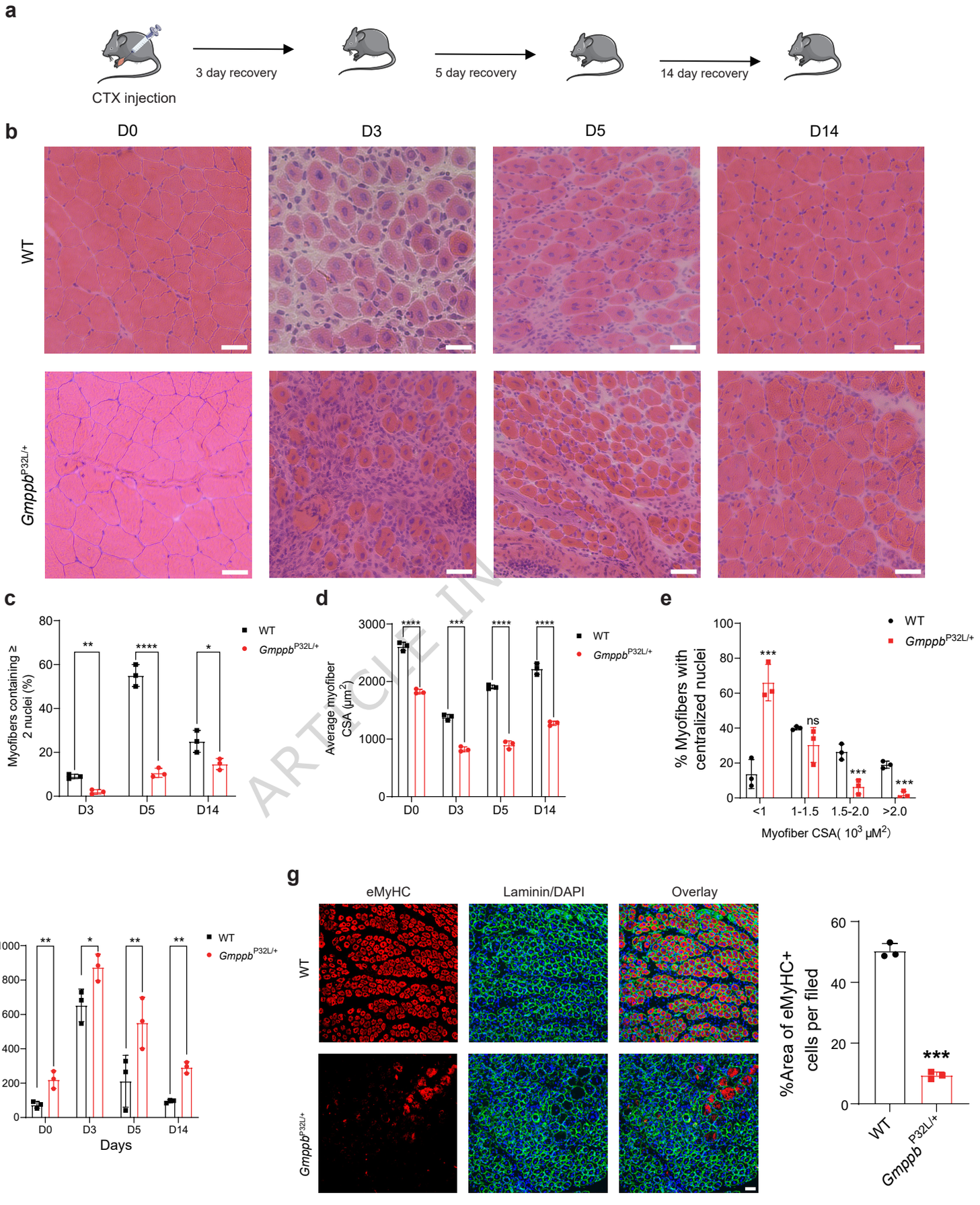
a
CTX injection
3 day recovery
5 day recovery
14 day recovery
b
D0
D3
D5
D14
WT
Gmppb P32L/+
c
Myofibers containing ≥ 2 nuclei (%)
WT
Gmppb P32L/+
D3
D5
D14
d
Average myofiber CSA (μm2)
WT
Gmppb P32L/+
D0
D3
D5
D14
e
% Myofibers with centralized nuclei
WT
Gmppb P32L/+
ns
<1
1-1.5
1.5-2.0
>2.0
Myofiber CSA(10^3 μM^2)
f
Serum CK level(U/L)
WT
Gmppb P32L/+
D0
D3
D5
D14
Days
g
eMyHC
Laminin/DAPI
Overlay
WT
Gmppb P32L/+
%Area of eMyHC+ cells per filed
WT
Gmppb P32L/+

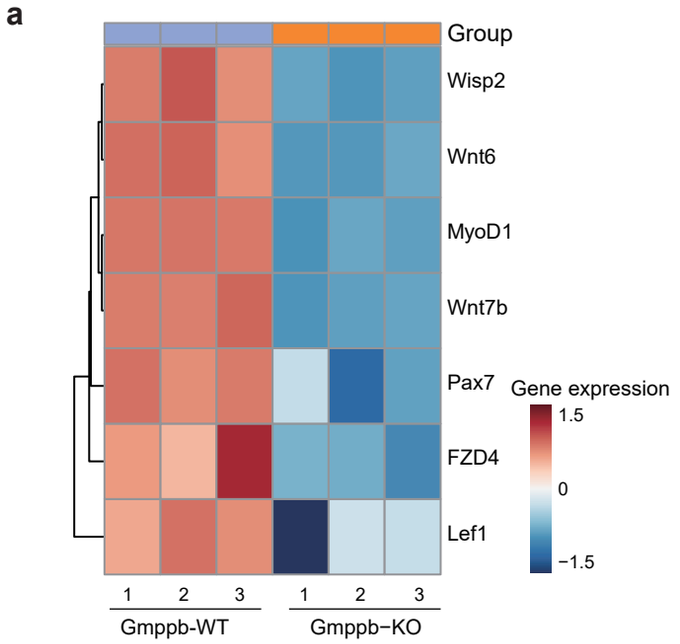
a
Group
Wisp2
Wnt6
MyoD1
Wnt7b
Pax7
FZD4
Lef1
Gene expression
1.5
0
−1.5
1 2 3 1 2 3
Gmppb-WT
Gmppb−KO

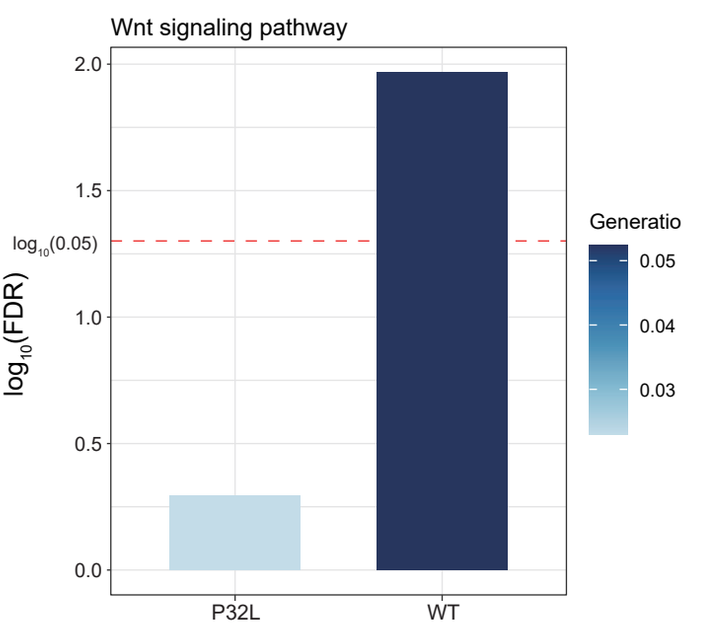
b
Wnt signaling pathway
log10(FDR)
log10(0.05)
2.0
1.5
1.0
0.5
0.0
P32L
WT
Generatio
0.05
0.04
0.03

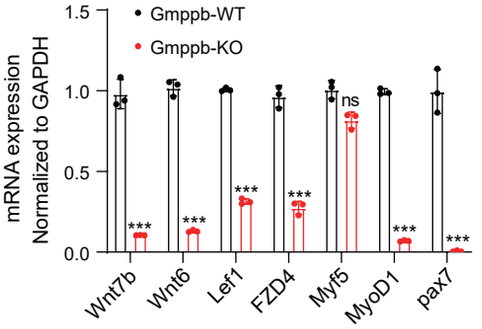
c
Gmppb-WT
Gmppb-KO
mRNA expression
Normalized to GAPDH
1.5
1.0
0.5
0.0
ns
***
Wnt7b
Wnt6
Lef1
FZD4
Myf5
MyoD1
pax7

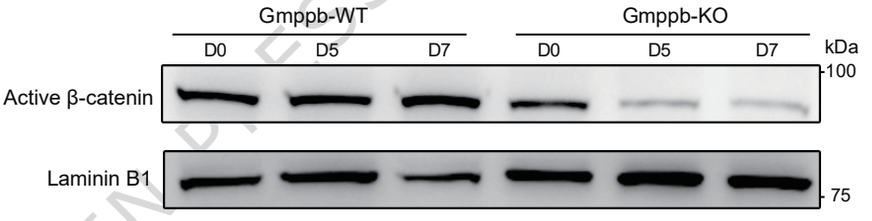
d
Gmppb-WT
Gmppb-KO
D0
D5
D7
D0
D5
D7
kDa
Active β-catenin
100
Laminin B1
75

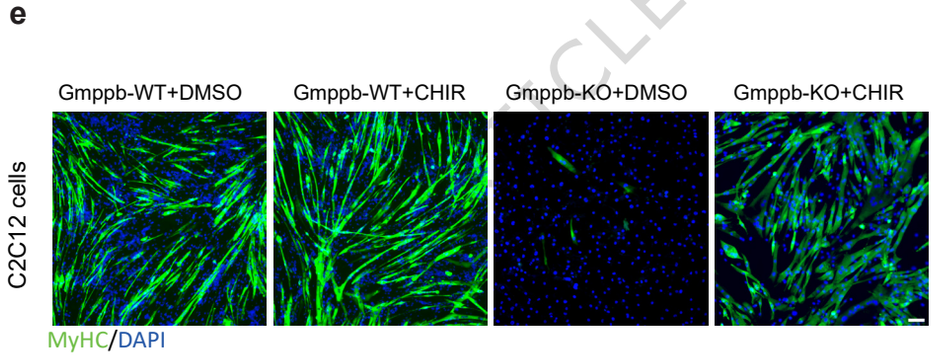
e
Gmppb-WT+DMSO
Gmppb-WT+CHIR
Gmppb-KO+DMSO
Gmppb-KO+CHIR
C2C12 cells
MyHC/DAPI

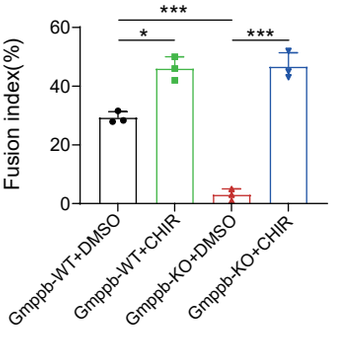
Fusion index(%)
60
40
20
0
***
*
***
Gmppb-WT+DMSO
Gmppb-WT+CHIR
Gmppb-KO+DMSO
Gmppb-KO+CHIR

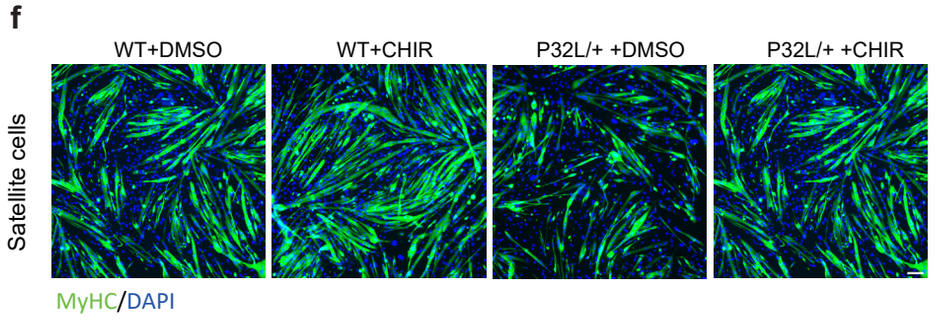
f
WT+DMSO
WT+CHIR
P32L/+ +DMSO
P32L/+ +CHIR
Satellite cells
MyHC/DAPI

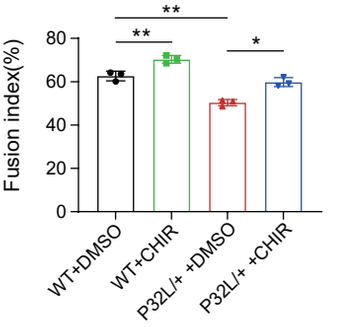
Fusion index(%)
80
60
40
20
0
**
**
*
WT+DMSO
WT+CHIR
P32L/+ +DMSO
P32L/+ +CHIR

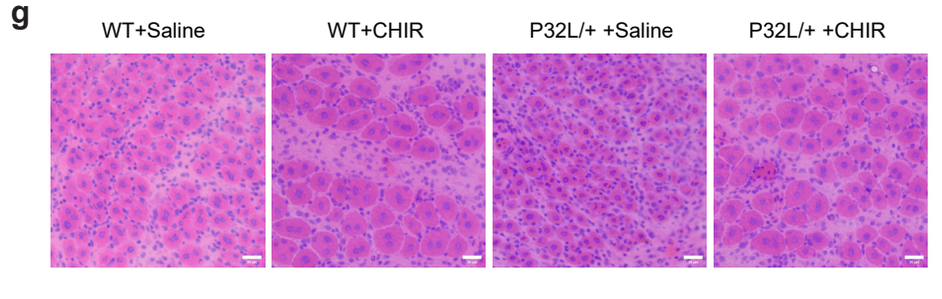
g
WT+Saline
WT+CHIR
P32L/+ +Saline
P32L/+ +CHIR

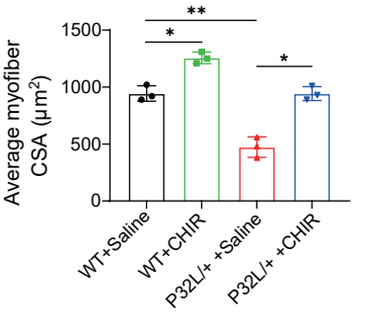
Average myofiber CSA (μm2)
1500
1000
500
0
**
*
*
WT+Saline
WT+CHIR
P32L/+ +Saline
P32L/+ +CHIR

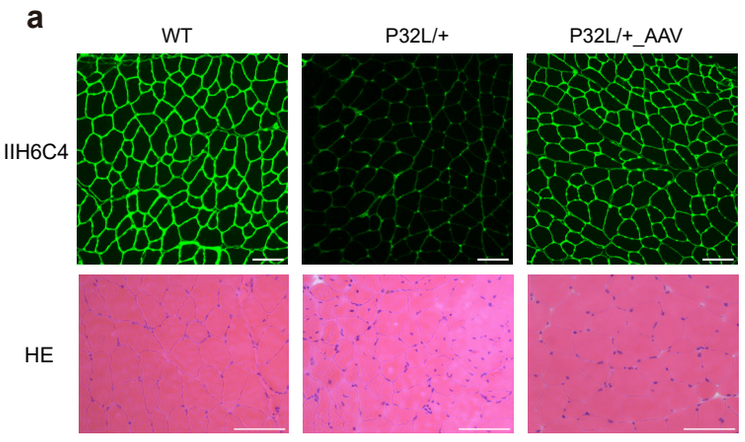
a
WT
P32L/+
P32L/+_AAV
IIH6C4
HE

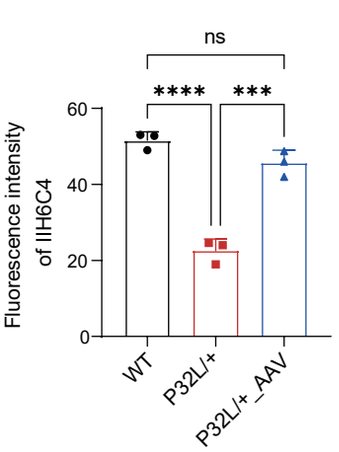
b
ns
****
***
Fluorescence intensity of IIH6C4
60
40
20
0
WT
P32L/+
P32L/+ _AAV

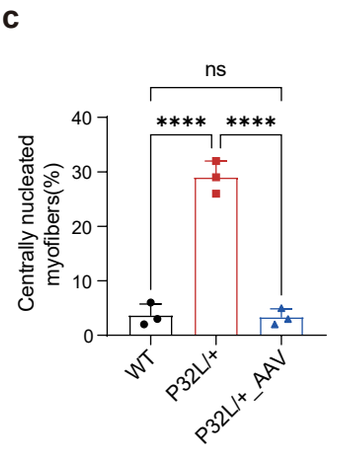
c
ns
****
****
Centrally nucleated myofibers(%)
40
30
20
10
0
WT
P32L/+
P32L/+ _AAV

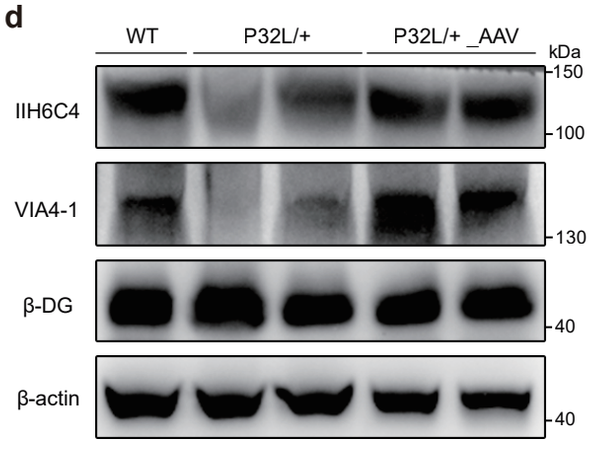
d
WT
P32L/+
P32L/+ _AAV
kDa
IIH6C4
150
100
VIA4-1
130
β-DG
40
β-actin
40

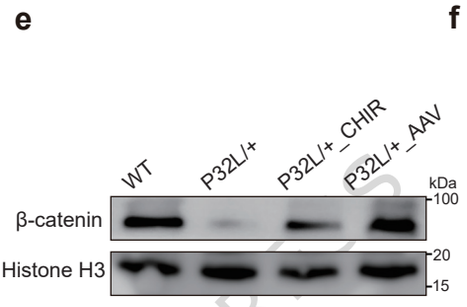
e
WT
P32L/+
P32L/+ _CHIR
P32L/+ _AAV
kDa
β-catenin
100
Histone H3
20
15

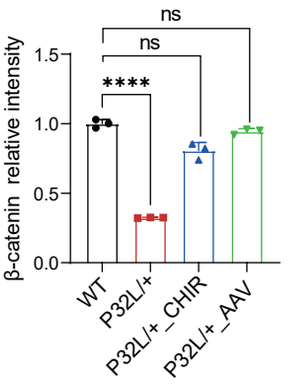
f
ns
ns
****
β-catenin relative intensity
1.5
1.0
0.5
0.0
WT
P32L/+
P32L/+ _CHIR
P32L/+ _AAV

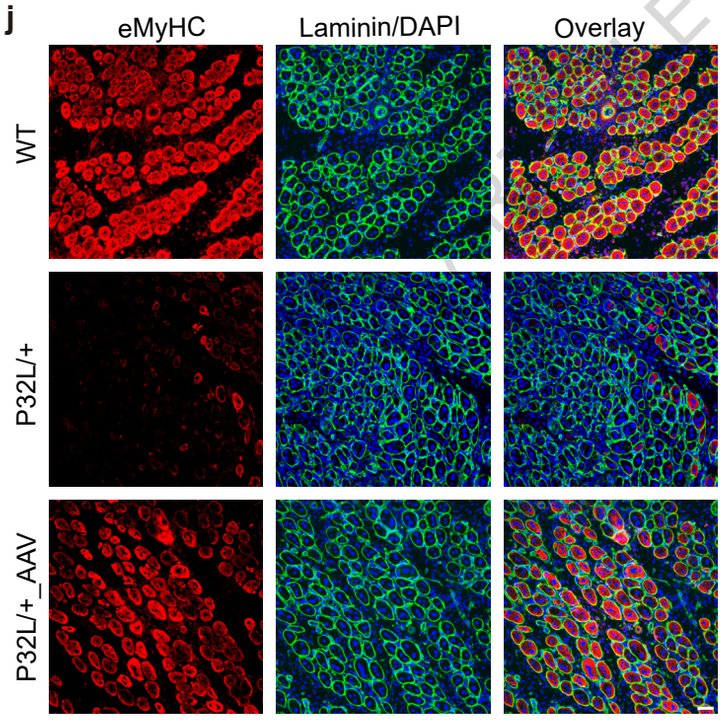
j
eMyHC
Laminin/DAPI
Overlay
WT
P32L/+
P32L/+_AAV

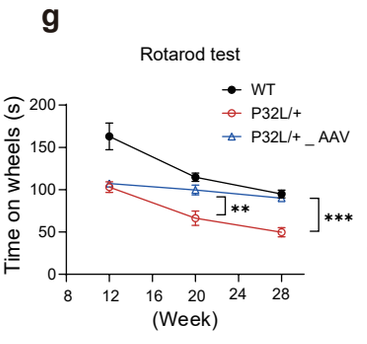
g
Rotarod test
WT
P32L/+
P32L/+ _ AAV
Time on wheels (s)
200
150
100
50
0
**
***
8
12
16
20
24
28
(Week)

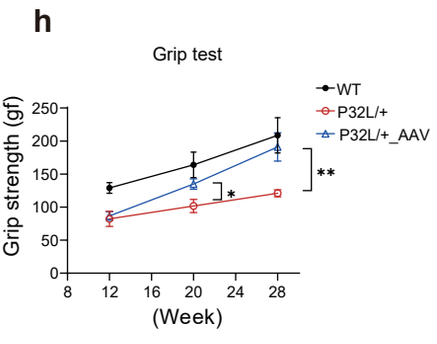
h
Grip test
WT
P32L/+
P32L/+_AAV
Grip strength (gf)
250
200
150
100
50
0
*
**
8
12
16
20
24
28
(Week)

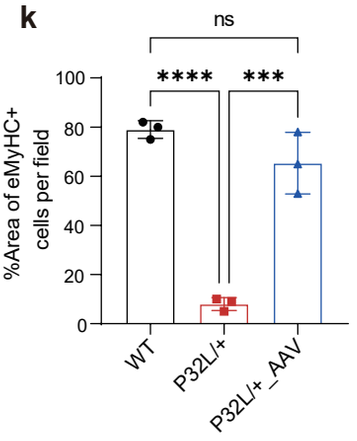
k
ns
****
***
%Area of eMyHC+ cells per field
100
80
60
40
20
0
WT
P32L/+
P32L/+ _AAV

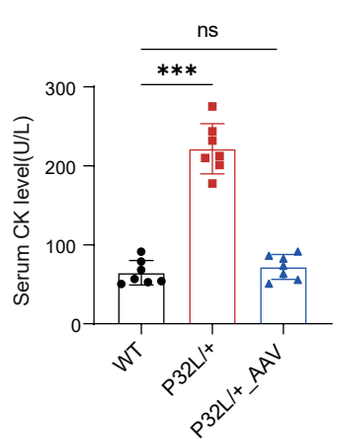
i
ns
***
Serum CK level(U/L)
300
200
100
0
WT
P32L/+
P32L/+ _AAV